Acoustic Biomolecules for Diagnostic Ultrasound Imaging

Thesis by

Bill Ling

In Partial Fulfillment of the Requirements for
the Degree of Doctor of Philosophy in
Chemical Engineering

CALIFORNIA INSTITUTE OF TECHNOLOGY
Pasadena, California

2023
(Defended May 26, 2023)

Bill Ling
ORCID: 0000-0002-1276-7204

ACKNOWLEDGEMENTS

First and foremost, I am eternally grateful for the opportunities and mentorship provided by my PhD advisor, Mikhail Shapiro. You welcomed a student who knew little about imaging or biology and allowed me the freedom to explore my interests. You have cultivated an immensely multidisciplinary lab, with every single group meeting providing an exciting chance to learn something new. You were always generous with your time, offering regular feedback and suggestions, and I am continually amazed by your prompt responses, even to my 2 AM emails. It has truly been inspiring to work with you as you built the lab, earned tenure, were appointed to HHMI, among other accomplishments. Thank you.

I would also like to thank my undergraduate research advisor, Tom Lectka, and graduate student mentor, Cody Ross Pitts, for introducing me to academic lab work. My research career began with you teaching me how to set up a lab notebook.

I am grateful to my committee members, Mark Davis, Rustem Ismagilov, and Warren Chan, for their guidance throughout this project.

Over the past few years, I have had the honor to work with many brilliant collaborators and colleagues in the Shapiro lab. Thank you, Anupama Lakshmanan, David Maresca, and Audrey Lee-Gosselin, for teaching me the skills that allowed me to work independently. Thank you, Di Wu, Mohamed Abedi, Dan Piraner, Arash Farhadi, Pradeep Ramesh, and George Lu, for being amazing and giving great advice to a young student. Thank you, Rob Hurt, for McDonald's. Thank you, Zhiyang Jin, Yuxing Yao, Ruby Zhang, Justin Lee, Danny Sawyer, Teresa Tran, Mei Yi You, and Tom Duan, for the San Gabriel adventures; I'm getting hungry just thinking about them. Thank you, Jeong Hoon Ko, Gunho

Kim, and Ben Stordy, for being great friends and fantastic co-authors. It's been a pleasure working closely with you. Thank you, Ernesto Criado-Hidalgo, Shirin Shivaei, Abdullah Farooq, Avinoam Bar-Zion, Joe Wekselblatt, Nivin Nystrom, and Cameron Smith, for the great conversations and lots of laughs. Thank you, Bilge Gungoren, for being an outstanding undergrad. Thank you, Dina Malounda, for being the world's greatest GV factory. To all current and former Shapiro Lab members, thank you for your friendship and for creating a fun, creative environment in which to learn and discover.

I am also grateful for all the friendships outside of the lab. Thank you, Constantine Sideris, Jin Mo Koo, Sergio Guevara, and Luis Garcia, for the adventures around LA. Special thanks to the Caltech gym for providing opportunities to meet George Mountoufaris, Stefan Wan, Luke Frankiw, Szilard Szoke, Joe Ruan, and Hristos Courellis.

To Alessandra Felloni, thank you for your love and support. You have somehow put up with my annoying tendencies and have kept me motivated from across the country.

To my parents, Deyi Ling and Yongxia Huang, everything that Kenny and I have achieved has been due to your hard work and sacrifice. All of our accomplishments are yours.

Finally, I would like to thank Grandpa Tigro Buddy and Chairman Meow for their unwavering moral support.

ABSTRACT

Nanotechnology has enabled significant breakthroughs in the early detection and treatment of disease, but many of these advances rely on expensive and less-accessible imaging modalities. Ultrasound, on the other hand, is a noninvasive imaging modality that stands out for its universal availability, cost-effectiveness, and safety. However, harnessing the benefits of nanomaterials for ultrasound has been challenging due to the size and stability constraints of typical ultrasound contrast agents. Recently, an innovative solution has emerged in the form of gas vesicles (GVs), a class of air-filled protein nanostructures found in certain aquatic microbes. These promising next-generation ultrasound contrast agents offer a crucial bridge between nanotechnology and ultrasonography.

In this thesis, we investigate the *in vivo* behavior of GVs, explore their potential applications as nanodiagnostic agents, and consider key factors for their future clinical deployment. In Chapter 2, we examine the interactions of GVs with blood components, focusing on imaging performance and immunogenicity. In Chapter 3, we show that intravenously injected GVs are cleared by liver-resident macrophages and subsequently undergo lysosomal degradation. We leverage this finding to develop an ultrasound-based method for visualizing cellular degradative processes and demonstrate its potential as a liver disease diagnostic. In Chapter 4, we introduce bicone GVs, the smallest known ultrasound contrast agent. We show that these sub-80 nm particles can penetrate tumors, deliver potent

ultrasound-induced mechanical effects, and are readily engineered for molecular targeting, extended circulation time, and payload conjugation.

Together, these findings highlight the tremendous potential of GVs as injectable nanomaterials for ultrasound imaging, laying the foundation for future studies to further refine the design and application of these agents.

PUBLISHED CONTENT AND CONTRIBUTIONS

Ling, B.*, Ko, J.H.*, Stordy, B., Zhang, Y., Didden T.F., Malounda, D., Swift, M.B., Chan, W.C.W.C., Shapiro, M.G. Pharmacokinetics and pharmacodynamics of acoustic biomolecules: the role of blood components. *In preparation*

B.L. conceived the study with J.H.K., conducted experiments, analyzed the data, and prepared the manuscript.

Ling, B., Gungoren, B., Yao, Y., Dutka, P., Lee, J., Swift, M.B., Shapiro, M.G. Truly tiny acoustic biomolecules for ultrasound diagnostics and therapy. *In preparation*.

B.L. conceived the study, conducted experiments, analyzed the data, and prepared the manuscript.

Sawyer, D.P., Bar-Zion, A., Farhadi, A., Shivaei, S., **Ling, B.**, Lee-Gosselin, A., Shapiro, M.G. Ultrasensitive ultrasound imaging of gene expression with signal unmixing. *Nat. Methods* **18**, 945-952 (2021). DOI: https://doi.org/10.1038/s41592-021-01229-w

B.L. participated in designing and conducting in vivo experiments with D.P.S.

Rabut, C., Wu, D., **Ling, B.**, Jin, Z., Malounda, D., Shapiro, M.G. Ultrafast amplitude modulation for molecular and hemodynamic ultrasound imaging. *Appl. Phys. Lett.* **118**, 244102 (2021). DOI: https://doi.org/10.1063/5.0050807

B.L. assisted with in vivo experiments.

Yao, Y., Jin, Z., **Ling, B.**, Malounda, D., Shapiro, M.G. Self-assembly of protein superstructures by physical interactions under cytoplasm-like conditions. *Biophys. J.* **120**, 2701-2709 (2021). DOI: https://doi.org/10.1016/j.bpj.2021.05.007

B.L. participated in data collection.

Rabut, C., Yoo, S., Hurt, R.C., Jin, Z., Guo, H., **Ling, B.**, Shapiro, M.G. Ultrasound technologies for imaging and modulating neural activity. *Neuron* **108**, 93-110 (2020). DOI: https://doi.org/10.1016/j.neuron.2020.09.003

B.L. participated in the writing of the manuscript.

Ling, B., Lee, J., Maresca, D., Lee-Gosselin, A., Malounda, D., Swift, M.B., Shapiro, M.G. Biomolecular ultrasound imaging of phagolysosomal function. *ACS Nano* **14**, 12210-12221 (2020). DOI: https://doi.org/10.1021/acsnano.0c05912

B.L. conceived the study, conducted experiments, analyzed the data, and wrote the manuscript.

Maresca, D., Payen, T., Lee-Gosselin, A., **Ling, B.**, Malounda, D., Demene, C., Tanter, M., Shapiro, M.G. Acoustic biomolecules enhance hemodynamic functional ultrasound imaging of neural activity. *NeuroImage* **209**, 116467 (2019). DOI: https://doi.org/10.1016/j.neuroimage.2019.116467

B.L. conducted in vivo experiments with A.L. and D.M.

Farhadi, A., Ho, G., Kunth, M., **Ling, B.**, Lakshmanan, A., Lu, G.J., Bourdeau, R., Schroder, L., Shapiro, M.G. Recombinantly expressed gas vesicles as nanoscale contrast agents for ultrasound and hyperpolarized MRI. *AIChE J.* **64**, 2927-2933 (2018). DOI: https://doi.org/10.1002/aic.16138

B.L. participated in data collection.

TABLE OF CONTENTS

LIST OF ILLUSTRATIONS

Number *Page*

LIST OF TABLES

Number *Page*

Chapter 1

BIOMOLECULAR ULTRASOUND DIAGNOSTICS AND THERAPEUTICS

1.1 Introduction

Early detection of disease is a key element in improving health outcomes, as demonstrated by the significant reduction in mortality following the adoption of effective screening methods such as Pap smears for cervical cancer and mammography for breast cancer[1–3]. Building on this progress, the field of nanotechnology has given rise to a range of innovative diagnostic tools capable of imaging specific molecules and biological processes[4,5]. These nanoprobes offer a potential alternative to invasive procedures, such as endoscopy and biopsy, which carry significant complication risks and depend heavily on operator expertise[6,7].

For instance, nonalcoholic fatty liver disease (NAFLD) affects over 25% of the global population and can lead to a range of serious health outcomes, including hepatitis, cirrhosis, fibrosis, and hepatocellular carcinoma[8,9]. Its diagnosis predominantly relies on biopsy, a procedure impractical for regular testing given the large patient population. Recently developed nanoparticles responsive to biomarkers of NAFLD and fibrosis have shown promise for minimally invasive screening and monitoring of this disease[10,11].

Similarly, nanoprobes have been designed to sense unique signatures of cancerous tissue, offering new avenues for cancer detection[12–14].

Despite the transformative potential of nanoparticle diagnostics, their practical implementation has been hindered by factors such as high cost, limited accessibility, and safety concerns[5,15]. Many of these probes are designed for imaging modalities such as computed tomography (CT), position emission tomography (PET), single photon emission computed tomography (SPECT), and magnetic resonance imaging (MRI)[15–17]. While these modalities provide high-resolution, whole-body imaging capabilities, their associated instruments are expensive, require specialized infrastructure, and their accessibility is often restricted, particularly in resource-limited settings. Furthermore, some of these imaging techniques expose patients to ionizing radiation, an undesirable factor for routine screening.

Biomedical ultrasound stands out as a promising solution to bridge the gap between the innovations of nanotechnology and their pragmatic clinical application. This modality meets three key criteria for broad adoption of a diagnostic method: safety, accessibility, and the provision of specific, actionable information[18,19]. Ultrasound is one of the most widely available medical imaging modalities, with ongoing developments such as smartphone- or tablet-operated systems and wireless transducers broadening its reach to bedside diagnostics and even remote, low-resource settings[20]. Not only does it produce high-resolution images in real-time using nonionizing radiation, but it is also being further enhanced by emerging artificial intelligence tools aiding operation and interpretation[21].

In this chapter, we provide an overview of biomedical ultrasound and the integral role of contrast agents in diagnostic imaging. We introduce gas vesicles (GVs), a promising

next-generation contrast agent, and explore their potential to pioneer a new approach for nano-enabled ultrasound imaging and therapy.

1.2 Biomedical ultrasound

Biomedical ultrasound is an indispensable tool in modern medicine, employing sound waves with frequencies beyond the human auditory threshold to interact with the body[19,22,23]. It has allowed clinicians diagnose and treat a variety of conditions with unparalleled safety and precision. Here, we will describe the fundamental principles underlying diagnostic and therapeutic ultrasound and highlight significant innovations in these areas.

1.2.1 Diagnostic ultrasound

Diagnostic ultrasound produces real-time, high-resolution images that provide valuable insight into organ anatomy and physiology[18,24]. The imaging process utilizes a pulse-echo principle, where a transducer emits acoustic waves—typically above 1 MHz—towards the target tissue. The transducer then detects the returning echoes, calculating depth from the time taken for the echoes to return. These echoes emerge as the transmitted wave encounters changes in acoustic impedance, a property defined by local density and compressibility. Boundaries between tissues with contrasting impedances generate strong reflections, resulting in well-delineated organs, while smaller structures, such as cells and extracellular matrix, produce weak, omnidirectional scattering.

Enhancing the diagnostic utility of ultrasound examinations are various imaging modes, designed to selectively capture different aspects of the acoustic signals[22,24]. This array

includes B-mode imaging, several nonlinear imaging modes, and Doppler imaging.

B-mode imaging, the most common, translates the amplitude of backscattered echoes into a real-time, two-dimensional image of tissue anatomy. Nonlinear imaging modes, such as pulse inversion and amplitude modulation, amplify higher frequency components, reducing imaging artifacts and selectively visualizing contrast agents[25,26]. Doppler imaging uses the frequency shift imparted on returning echoes by moving blood cells to visualize vascular structures and assess blood flow dynamics. The development of 2D transducers has extended these techniques to encompass volumetric imaging[27,28].

Among recent innovations, the use of plane waves has facilitated clinically relevant techniques such as shear wave elastography and functional imaging[22]. Unlike traditional pulse sequences that scan line-by-line, plane waves illuminate the entire region of interest with a single transmit event, enabling frame rates of several kilohertz. Ultrafast imaging of this kind can track the propagation of shear waves generated by a high-intensity focused acoustic pulse, thereby creating a map of local tissue elasticity[29]—useful for monitoring diseases such as liver fibrosis and certain cancers[30].

Functional ultrasound imaging (fUSI) combines ultrafast imaging with the Doppler paradigm to visualize regional blood flow enhancements following bursts of neural activity[31,32]. These developments, in conjunction with the compact nature of ultrasound systems, facilitate imaging in awake and freely moving subjects, including rodents[33,34] and human infants[35], and enable single-trial studies, which are challenging with modalities such as functional magnetic resonance imaging (fMRI). This is facilitating development of

sophisticated applications, including motor decoding algorithms for brain-machine interfaces[36,37] and intra-operative guidance during brain surgery[38].

1.2.2 Therapeutic Ultrasound

Therapeutic ultrasound uses focused acoustic waves to induce localized thermal and mechanical effects within the body, providing a noninvasive option for various medical interventions[39]. These include tissue ablation, heating, and neuromodulation. Precise ablation of brain regions, tumors, and other tissue can be achieved by inducing tissue necrosis through heating to high temperatures[40,41]. Another technique, histotripsy, uses short, high-pressure pulses to mechanically disrupt tissue, minimizing side effects from thermal conduction[42]. Interestingly, both mechanisms can stimulate systemic immune responses, potentially enhancing the outcomes of cancer immunotherapy[43,44].

Furthermore, focused ultrasound can trigger biological effects by stimulating genetic and neural circuits. For example, engineered cells carrying temperature-sensitive gene circuits[45] can be heated to a specific temperature to initiate programming such as cytotoxicity or cytokine secretion[46–48]. Ultrasound pulses can also trigger neuronal firing by activating mechanosensitive channels on the cell surface[19,49]. This approach is currently under investigation for treatment of diabetes[50,51] and autoimmune disease[52,53].

1.3 Microbubble Contrast Agents

Ultrasound imaging primarily delivers anatomical and limited physiological data. To enrich this information, contrast agents are needed to illuminate structures of interest. Gas

microbubbles have been particularly effective as ultrasound imaging agents, as their low density and high compressibility relative to tissue results in strong acoustic scattering and size oscillations, which in turn generate nonlinear contrast[23,54,55]. Clinical formulations typically comprise a low-solubility fluorinated gas stabilized by a shell of lipids or protein, with diameters above 1 μm.

Initially developed for evaluating cardiac function[56,57], microbubbles are now used to visualize blood flow across various organs. Recent innovations include algorithms to track the movement of individual microbubbles, yielding maps of vasculature and flow velocity with sub-wavelength resolution[58]. This technique enabled detection of deep cerebral aneurysms in human patients[59] and could be helpful for monitoring other diseases where microvascular flows are significantly altered, such as cancer and stroke. Additionally, this approach has been extended to functional and volumetric imaging[27,60], providing superior resolution and easier implementation than comparable CT or MRI methods.

Customization of microbubbles for specific applications such as molecular imaging and drug delivery is an active area of research. For instance, Bracco's BR55 agent, which incorporates targeting peptides in its shell, is currently in clinical trials for detecting angiogenesis markers in various cancers[61–63]. Similar configurations are being explored to target other markers associated with cancer and inflammation[62,64]. Additionally, microbubbles can serve as vehicles for delivering surface-adsorbed plasmid DNA[54,65] by oscillating near cell membranes to induce formation of transient pores[66]. A similar

mechanism has been used to temporarily open the blood-brain barrier (BBB), allowing passage of therapeutics including small molecules, antibodies, and viruses[67,68].

Despite their many applications, microbubbles face significant limitations for clinical use. Surface tension promotes bubble dissolution by inducing a pressure gradient between the internal gas and surrounding medium. This pressure gradient is inversely proportional to diameter, restricting microbubbles to dimensions above 1 μm[23,55]. Consequently, they are sterically confined to the vasculature, unable to reach targets within the tissue. Furthermore, their efficient filtration from the bloodstream results in circulation half-lives of only several minutes, often necessitating multiple infusions during an imaging session[54,69]. While potential alternatives such as nanobubbles[70,71] and nanodroplets[72,73] have shown some success, they can be challenging to prepare, and their capabilities remain under investigation. Consequently, there is a need for smaller, more stable ultrasound contrast agents.

1.4 Biomolecular Ultrasound

Gas vesicles (GVs) are biogenic, air-filled protein nanostructures that have emerged as a promising next-generation ultrasound contrast agent[74]. These naturally occurring structures are produced by certain aquatic microbes to regulate buoyancy for optimal positioning during photosynthesis[75,76]. GVs form through a nucleation complex that assembles repeating units of GvpA and other structural proteins into a hollow shell[77,78]. As the GV elongates, GvpC is added as an external scaffold to provide structural rigidity. The resultant 3-nm thick protein shell has a highly hydrophobic inside surface that prevents the condensation of liquid water but allows for the free exchange of gas, creating a stable pocket of air with a hydrodynamic

diameter of approximately 250 nm. In 2014, it was first demonstrated that this air-liquid interface strongly scatters acoustic waves, enabling GVs to produce robust ultrasound contrast[74].

Since the inception of the biomolecular ultrasound field, there have been considerable advances in the understanding and application of GV-based contrast agents[18]. Specialized pulse sequences have been designed to sensitively and specifically detect GVs, leveraging unique acoustic signatures produced by the buckling[79–81] and collapse of the GV shell[82]. Concurrently, strides have been made in GV engineering, primarily focused on manipulating the underlying genetic sequence[83–85] or biochemically functionalizing the shell proteins[74,86–88]. GVs have also been repurposed as reporter genes to monitor gene expression in engineered bacteria and mammalian cells[89–92].

GVs offer numerous advantages over traditional contrast agents. They are easily isolated from their native hosts and have a long shelf-life[74,93]. For Doppler-based applications, GVs provide superior velocity-matching compared to microbubbles[94], and their inherent stability potentially allows for much longer imaging windows. A particularly unique aspect of GVs is the capacity to alter their acoustic response. Their genetically-defined collapse thresholds have been utilized for multiplexed imaging by sequentially erasing weaker populations[83]. Additionally, sensing moieties can be inserted into the GvpC proteins, allowing them to unbind in response to enzyme activity, switching on nonlinear contrast[84].

Besides ultrasound imaging, GVs have shown promising results as agents for cellular patterning[95], therapeutic ultrasound[96,97], optical imaging[98,99], and MRI[100,101].

1.5 Opportunities in Nanodiagnostics

GVs have the potential to significantly expand the capabilities of ultrasound by drawing on the breakthroughs of nanomedicine. As nanoscale agents, they can interact with biologically relevant structures through mechanisms that are unavailable to small molecules or bulk materials[15,16]. For instance, nanoparticles can accumulate in cancerous tissue through the enhanced permeability and retention (EPR) effect, a phenomenon believed to arise from a combination of active trafficking by endothelial cells[102,103] and passive leakage through gaps in the vasculature[104]. The surface of GVs can be engineered to leverage these interactions, thereby creating a wide array of molecular imaging probes. Furthermore, their biosensing capabilities can be engineered for activity-based diagnostics[4] of diseases such as cancer[13] and atherosclerosis[105], where the tissue microenvironment and enzyme activities are often altered.

In order to harness this potential, it is essential to understand GV interactions with the body. Upon administration, a particle's behavior is significantly impacted by the cells and fluids it encounters. For instance, intravenously injected nanoparticles are instantaneously coated with serum proteins, forming a protein corona that alters the particles' physicochemical properties and recognition by the body[106–108]. The protein corona mediates many subsequent interactions within the body, and its composition is predictive of factors such as biodistribution, toxicity, and cellular uptake[109–112]. Potential negative effects on

nanoprobe performance include masking of targeting ligands, engaging immune cells, and triggering aggregation.

Likewise, understanding the metabolism and elimination of a particle is crucial for developing guidelines for dosing and safety. GVs and most other nanoparticles are eventually sequestered by the liver due to factors such as large volume, slow blood flow, and an abundance of macrophages[113–115]. This may inadvertently lead to toxicity through unwanted immune responses and long-term accumulation[113].

This thesis will provide a comprehensive investigation of the journey of GVs within the body—beginning from their immediate interaction with blood following intravenous injection, navigating through their biodistribution, and culminating in their eventual metabolic clearance by the liver. Our objective is to deepen our understanding of GV behavior *in vivo*, which will inform the development of more efficacious GV-based imaging agents. Alongside this, our insights will spur the creation of novel technologies, uniquely enabled by these interactions. Finally, we will engineer ultra-small GVs and explore how they can introduce ultrasound imaging to the realm of nanomedicine.

References

1. Clarke, E. A. & Anderson, T. W. Does screening by 'Pap' smears help prevent cervical cancer?: A case-control study. *The Lancet* **314**, 1–4 (1979).
2. Mählck, C. G., Jonsson, H. & Lenner, P. Pap smear screening and changes in cervical cancer mortality in Sweden. *Int. J. Gynecol. Obstet.* **44**, 267–272 (1994).
3. Schopper, D. & de Wolf, C. How effective are breast cancer screening programmes by mammography? Review of the current evidence. *Eur. J. Cancer* **45**, 1916–1923 (2009).
4. Soleimany, A. P. & Bhatia, S. N. Activity-based diagnostics: An emerging paradigm for disease detection and monitoring. *Trends Mol. Med.* **26**, 450–468 (2020).
5. Weissleder, R. Molecular imaging in cancer. *Science* **312**, 1168–1171 (2006).
6. Zhao, H. *et al.* Updated analysis of complication rates associated with invasive diagnostic procedures after lung cancer screening. *JAMA Netw. Open* **3**, e2029874 (2020).
7. Midia, M., Odedra, D., Shuster, A., Midia, R. & Muir, J. Predictors of bleeding complications following percutaneous image-guided liver biopsy: A scoping review. *Diagn. Interv. Radiol.* **25**, 71–80 (2019).
8. Brunt, E. M. *et al.* Nonalcoholic fatty liver disease. *Nat. Rev. Dis. Primer* **1**, 1–22 (2015).
9. Cotter, T. G. & Rinella, M. Nonalcoholic fatty liver disease 2020: The state of the disease. *Gastroenterology* **158**, 1851–1864 (2020).
10. Kwong, G. A. *et al.* Mass-encoded synthetic biomarkers for multiplexed urinary monitoring of disease. *Nat. Biotechnol.* **31**, 63–70 (2013).
11. Cazanave, S. C. *et al.* Peptide-based urinary monitoring of fibrotic nonalcoholic steatohepatitis by mass-barcoded activity-based sensors. *Sci. Transl. Med.* **13**, eabe8939 (2021).
12. Hao, L. *et al.* Microenvironment-triggered multimodal precision diagnostics. *Nat. Mater.* **20**, 1440–1448 (2021).
13. Kwon, E. J., Dudani, J. S. & Bhatia, S. N. Ultrasensitive tumour-penetrating nanosensors of protease activity. *Nat. Biomed. Eng.* **1**, 1–10 (2017).
14. Loynachan, C. N. *et al.* Renal clearable catalytic gold nanoclusters for in vivo disease monitoring. *Nat. Nanotechnol.* **14**, 883–890 (2019).
15. Chen, G., Roy, I., Yang, C. & Prasad, P. N. Nanochemistry and nanomedicine for nanoparticle-based diagnostics and therapy. *Chem. Rev.* **116**, 2826–2885 (2016).
16. Lim, E.-K. *et al.* Nanomaterials for theranostics: Recent advances and future challenges. *Chem. Rev.* **115**, 327–394 (2015).
17. Mitchell, M. J. *et al.* Engineering precision nanoparticles for drug delivery. *Nat. Rev. Drug Discov.* **20**, 101–124 (2021).
18. Maresca, D. *et al.* Biomolecular ultrasound and sonogenetics. *Annu. Rev. Chem. Biomol. Eng.* **9**, 229–252 (2018).
19. Rabut, C. *et al.* Ultrasound technologies for imaging and modulating neural activity. *Neuron* **108**, 93–110 (2020).
20. Mayes, J., White, A., Byrne, M. & Mogg, J. How smartphone technology is changing healthcare in developing countries. *Columbia Univ. J. Glob. Health* **6**, 36–38 (2016).

21. Muse, E. D. & Topol, E. J. Guiding ultrasound image capture with artificial intelligence. *The Lancet* **396**, 749 (2020).
22. Tanter, M. & Fink, M. Ultrafast imaging in biomedical ultrasound. *IEEE Trans. Ultrason. Ferroelectr. Freq. Control* **61**, 102–119 (2014).
23. Frinking, P., Segers, T., Luan, Y. & Tranquart, F. Three decades of ultrasound contrast agents: A review of the past, present and future improvements. *Ultrasound Med. Biol.* **46**, 892–908 (2020).
24. Cobbold, R. S. C. *Foundations of Biomedical Ultrasound*. (Oxford University Press, 2007).
25. Anvari, A., Forsberg, F. & Samir, A. E. A primer on the physical principles of tissue harmonic imaging. *RadioGraphics* **35**, 1955–1964 (2015).
26. Burns, P. N., Simpson, D. H. & Averkiou, M. A. Nonlinear imaging. *Ultrasound Med. Biol.* **26**, S19–S22 (2000).
27. Chavignon, A. *et al.* 3D transcranial ultrasound localization microscopy in the rat brain with a multiplexed matrix probe. *IEEE Trans. Biomed. Eng.* **69**, 2132–2142 (2022).
28. Rabut, C. *et al.* 4D functional ultrasound imaging of whole-brain activity in rodents. *Nat. Methods* **16**, 994–997 (2019).
29. Bercoff, J., Tanter, M. & Fink, M. Supersonic shear imaging: A new technique for soft tissue elasticity mapping. *IEEE Trans. Ultrason. Ferroelectr. Freq. Control* **51**, 396–409 (2004).
30. Deffieux, T. *et al.* Investigating liver stiffness and viscosity for fibrosis, steatosis and activity staging using shear wave elastography. *J. Hepatol.* **62**, 317–324 (2015).
31. Macé, E. *et al.* Functional ultrasound imaging of the brain. *Nat. Methods* **8**, 662–664 (2011).
32. Mace, E. *et al.* Functional ultrasound imaging of the brain: Theory and basic principles. *IEEE Trans. Ultrason. Ferroelectr. Freq. Control* **60**, 492–506 (2013).
33. Tiran, E. *et al.* Transcranial functional ultrasound imaging in freely moving awake mice and anesthetized young rats without contrast agent. *Ultrasound Med. Biol.* **43**, 1679–1689 (2017).
34. Urban, A. *et al.* Real-time imaging of brain activity in freely moving rats using functional ultrasound. *Nat. Methods* **12**, 873–878 (2015).
35. Demene, C. *et al.* Functional ultrasound imaging of brain activity in human newborns. *Sci. Transl. Med.* **9**, eaah6756 (2017).
36. Norman, S. L. *et al.* Single-trial decoding of movement intentions using functional ultrasound neuroimaging. *Neuron* **109**, 1554-1566.e4 (2021).
37. Griggs, W. S. *et al.* Decoding motor plans using a closed-loop ultrasonic brain-machine interface. *bioRxiv* doi: 10.1101/2022.11.10.515371 (2022).
38. Soloukey, S. *et al.* Functional ultrasound (fUS) during awake brain surgery: The clinical potential of intra-operative functional and vascular brain mapping. *Front. Neurosci.* **13**, (2020).
39. Izadifar, Z., Izadifar, Z., Chapman, D. & Babyn, P. An introduction to high intensity focused ultrasound: Systematic review on principles, devices, and clinical applications. *J. Clin. Med.* **9**, 460 (2020).

40. Illing, R. O. *et al.* The safety and feasibility of extracorporeal high-intensity focused ultrasound (HIFU) for the treatment of liver and kidney tumours in a Western population. *Br. J. Cancer* **93**, 890–895 (2005).
41. Meng, Y., Hynynen, K. & Lipsman, N. Applications of focused ultrasound in the brain: from thermoablation to drug delivery. *Nat. Rev. Neurol.* **17**, 7–22 (2021).
42. Xu, Z., Hall, T. L., Vlaisavljevich, E. & Lee, F. T. Histotripsy: The first noninvasive, non-ionizing, non-thermal ablation technique based on ultrasound. *Int. J. Hyperth. Off. J. Eur. Soc. Hyperthermic Oncol. North Am. Hyperth. Group* **38**, 561–575 (2021).
43. Eranki, A. *et al.* High intensity focused ultrasound (HIFU) triggers immune sensitization of refractory murine neuroblastoma to checkpoint inhibitor therapy. *Clin. Cancer Res. Off. J. Am. Assoc. Cancer Res.* **26**, 1152–1161 (2020).
44. Fite, B. Z. *et al.* Immune modulation resulting from MR-guided high intensity focused ultrasound in a model of murine breast cancer. *Sci. Rep.* **11**, 927 (2021).
45. Piraner, D. I., Abedi, M. H., Moser, B. A., Lee-Gosselin, A. & Shapiro, M. G. Tunable thermal bioswitches for in vivo control of microbial therapeutics. *Nat. Chem. Biol.* **13**, 75–80 (2017).
46. Abedi, M. H., Lee, J., Piraner, D. I. & Shapiro, M. G. Thermal control of engineered T-cells. *ACS Synth. Biol.* **9**, 1941–1950 (2020).
47. Abedi, M. H. *et al.* Ultrasound-controllable engineered bacteria for cancer immunotherapy. *Nat. Commun.* **13**, 1585 (2022).
48. Wu, Y. *et al.* Control of the activity of CAR-T cells within tumours via focused ultrasound. *Nat. Biomed. Eng.* **5**, 1336–1347 (2021).
49. Yoo, S., Mittelstein, D. R., Hurt, R. C., Lacroix, J. & Shapiro, M. G. Focused ultrasound excites cortical neurons via mechanosensitive calcium accumulation and ion channel amplification. *Nat. Commun.* **13**, 493 (2022).
50. Cotero, V. *et al.* Stimulation of the hepatoportal nerve plexus with focused ultrasound restores glucose homoeostasis in diabetic mice, rats and swine. *Nat. Biomed. Eng.* 1–23 (2022) doi:10.1038/s41551-022-00870-w.
51. Cotero, V. *et al.* Noninvasive sub-organ ultrasound stimulation for targeted neuromodulation. *Nat. Commun.* **10**, 952 (2019).
52. Zachs, D. P. *et al.* Noninvasive ultrasound stimulation of the spleen to treat inflammatory arthritis. *Nat. Commun.* **10**, 951 (2019).
53. Zanos, S. *et al.* Focused ultrasound neuromodulation of the spleen activates an anti-inflammatory response in humans. *Brain Stimulat.* **16**, 703–711 (2023).
54. Ferrara, K., Pollard, R. & Borden, M. Ultrasound microbubble contrast agents: Fundamentals and application to gene and drug delivery. *Annu. Rev. Biomed. Eng.* **9**, 415–447 (2007).
55. Stride, E. *et al.* Microbubble agents: New directions. *Ultrasound Med. Biol.* **46**, 1326–1343 (2020).
56. Gramiak, R. & Shah, P. M. Echocardiography of the aortic root. *Invest. Radiol.* **3**, 356 (1968).
57. Gramiak, R., Shah, P. M. & Kramer, D. H. Ultrasound cardiography: Contrast studies in anatomy and function. *Radiology* **92**, 939–948 (1969).

58. Errico, C. *et al.* Ultrafast ultrasound localization microscopy for deep super-resolution vascular imaging. *Nature* **527**, 499–502 (2015).
59. Demené, C. *et al.* Transcranial ultrafast ultrasound localization microscopy of brain vasculature in patients. *Nat. Biomed. Eng.* **5**, 219–228 (2021).
60. Renaudin, N. *et al.* Functional ultrasound localization microscopy reveals brain-wide neurovascular activity on a microscopic scale. *Nat. Methods* **19**, 1004–1012 (2022).
61. Willmann, J. K. *et al.* Ultrasound molecular imaging with BR55 in patients with breast and ovarian lesions: First-in-human results. *J. Clin. Oncol.* **35**, 2133–2140 (2017).
62. Abou-Elkacem, L., Bachawal, S. V. & Willmann, J. K. Ultrasound molecular imaging: Moving toward clinical translation. *Eur. J. Radiol.* **84**, 1685–1693 (2015).
63. Willmann, J. K. *et al.* Dual-targeted contrast agent for US assessment of tumor angiogenesis in vivo. *Radiology* **248**, 936–944 (2008).
64. Moccetti, F. *et al.* Ultrasound molecular imaging of atherosclerosis using small-peptide targeting ligands against endothelial markers of inflammation and oxidative stress. *Ultrasound Med. Biol.* **44**, 1155–1163 (2018).
65. Bez, M. *et al.* Nonviral ultrasound-mediated gene delivery in small and large animal models. *Nat. Protoc.* **14**, 1015–1026 (2019).
66. Helfield, B., Chen, X., Watkins, S. C. & Villanueva, F. S. Biophysical insight into mechanisms of sonoporation. *Proc. Natl. Acad. Sci.* **113**, 9983–9988 (2016).
67. Szablowski, J. O., Lee-Gosselin, A., Lue, B., Malounda, D. & Shapiro, M. G. Acoustically targeted chemogenetics for the non-invasive control of neural circuits. *Nat. Biomed. Eng.* **2**, 475–484 (2018).
68. Choi, J. J., Pernot, M., Small, S. A. & Konofagou, E. E. Noninvasive, transcranial and localized opening of the blood-brain barrier using focused ultrasound in mice. *Ultrasound Med. Biol.* **33**, 95–104 (2007).
69. Errico, C. *et al.* Transcranial functional ultrasound imaging of the brain using microbubble-enhanced ultrasensitive Doppler. *NeuroImage* **124**, 752–761 (2016).
70. Krupka, T. M. *et al.* Formulation and characterization of echogenic lipid−Pluronic nanobubbles. *Mol. Pharm.* **7**, 49–59 (2010).
71. Perera, R. H. *et al.* Ultrasound imaging beyond the vasculature with new generation contrast agents. *Wiley Interdiscip. Rev. Nanomed. Nanobiotechnol.* **7**, 593–608 (2015).
72. Sheeran, P. S. & Dayton, P. A. Phase-change contrast agents for imaging and therapy. *Curr. Pharm. Des.* **18**, 2152–2165 (2012).
73. Sheeran, P. S., Luois, S., Dayton, P. A. & Matsunaga, T. O. Formulation and acoustic studies of a new phase-shift agent for diagnostic and therapeutic ultrasound. *Langmuir* **27**, 10412–10420 (2011).
74. Shapiro, M. G. *et al.* Biogenic gas nanostructures as ultrasonic molecular reporters. *Nat. Nanotechnol.* **9**, 311–316 (2014).
75. Walsby, A. E. Gas vesicles. *Microbiol. Rev.* **58**, 94–144 (1994).
76. Pfeifer, F. Distribution, formation and regulation of gas vesicles. *Nat. Rev. Microbiol.* **10**, 705–715 (2012).
77. Huber, S. T., Terwiel, D., Evers, W. H., Maresca, D. & Jakobi, A. J. Cryo-EM structure of gas vesicles for buoyancy-controlled motility. *Cell* **186**, 975-986.e13 (2023).

78. Dutka, P. *et al.* Structure of Anabaena flos-aquae gas vesicles revealed by cryo-ET. *Structure* **31**, 518-528.e6 (2023).
79. Maresca, D., Sawyer, D. P., Renaud, G., Lee-Gosselin, A. & Shapiro, M. G. Nonlinear X-wave ultrasound imaging of acoustic biomolecules. *Phys. Rev. X* **8**, 041002 (2018).
80. Maresca, D. *et al.* Nonlinear ultrasound imaging of nanoscale acoustic biomolecules. *Appl. Phys. Lett.* **110**, 073704 (2017).
81. Rabut, C. *et al.* Ultrafast amplitude modulation for molecular and hemodynamic ultrasound imaging. *Appl. Phys. Lett.* **118**, 244102 (2021).
82. Sawyer, D. P. *et al.* Ultrasensitive ultrasound imaging of gene expression with signal unmixing. *Nat. Methods* **18**, 945–952 (2021).
83. Lakshmanan, A. *et al.* Molecular engineering of acoustic protein nanostructures. *ACS Nano* **10**, 7314–7322 (2016).
84. Lakshmanan, A. *et al.* Acoustic biosensors for ultrasound imaging of enzyme activity. *Nat. Chem. Biol.* **16**, 988–996 (2020).
85. Kim, J.-M. *et al.* Bioengineering of Halobacterium sp. NRC-1 gas vesicle nanoparticles with GvpC fusion protein produced in E. coli. *Appl. Microbiol. Biotechnol.* **106**, 2043–2052 (2022).
86. Hao, Y., Li, Z., Luo, J., Li, L. & Yan, F. Ultrasound molecular imaging of epithelial mesenchymal transition for evaluating tumor metastatic potential via targeted biosynthetic gas vesicles. *Small* **19**, 2207940 (2023).
87. Wang, G. *et al.* Surface-modified GVs as nanosized contrast agents for molecular ultrasound imaging of tumor. *Biomaterials* **236**, 119803 (2020).
88. Kim, W.-S. *et al.* Magneto-acoustic protein nanostructures for non-invasive imaging of tissue mechanics in vivo. *bioRxiv* doi: 2022.05.26.493158 (2022).
89. Bourdeau, R. W. *et al.* Acoustic reporter genes for noninvasive imaging of microorganisms in mammalian hosts. *Nature* **553**, 86–90 (2018).
90. Farhadi, A. *et al.* Recombinantly expressed gas vesicles as nanoscale contrast agents for ultrasound and hyperpolarized MRI. *AIChE J.* **64**, 2927–2933 (2018).
91. Farhadi, A., Ho, G. H., Sawyer, D. P., Bourdeau, R. W. & Shapiro, M. G. Ultrasound imaging of gene expression in mammalian cells. *Science* **365**, 1469–1475 (2019).
92. Hurt, R. C. *et al.* Genomically mined acoustic reporter genes for real-time in vivo monitoring of tumors and tumor-homing bacteria. *Nat. Biotechnol.* 1–13 (2023) doi:10.1038/s41587-022-01581-y.
93. Lakshmanan, A. *et al.* Preparation of biogenic gas vesicle nanostructures for use as contrast agents for ultrasound and MRI. *Nat. Protoc.* **12**, 2050–2080 (2017).
94. Maresca, D. *et al.* Acoustic biomolecules enhance hemodynamic functional ultrasound imaging of neural activity. *NeuroImage* **209**, 116467 (2020).
95. Wu, D. *et al.* Biomolecular actuators for genetically selective acoustic manipulation of cells. *Sci. Adv.* **9**, eadd9186 (2023).
96. Song, L. *et al.* Biogenic nanobubbles for effective oxygen delivery and enhanced photodynamic therapy of cancer. *Acta Biomater.* **108**, 313–325 (2020).
97. Bar-Zion, A. *et al.* Acoustically triggered mechanotherapy using genetically encoded gas vesicles. *Nat. Nanotechnol.* **16**, 1403–1412 (2021).

98. Farhadi, A. *et al.* Genetically encoded phase contrast agents for digital holographic microscopy. *Nano Lett.* **20**, 8127–8134 (2020).
99. Lu, G. J. *et al.* Genetically encodable contrast agents for optical coherence tomography. *ACS Nano* **14**, 7823–7831 (2020).
100. Shapiro, M. G. *et al.* Genetically encoded reporters for hyperpolarized xenon magnetic resonance imaging. *Nat. Chem.* **6**, 629–634 (2014).
101. Lu, G. J. *et al.* Acoustically modulated magnetic resonance imaging of gas-filled protein nanostructures. *Nat. Mater.* **17**, 456–463 (2018).
102. Kingston, B. R. *et al.* Specific endothelial cells govern nanoparticle entry into solid tumors. *ACS Nano* **15**, 14080–14094 (2021).
103. Sindhwani, S. *et al.* The entry of nanoparticles into solid tumours. *Nat. Mater.* **19**, 566–575 (2020).
104. Zhu, M. *et al.* Machine-learning-assisted single-vessel analysis of nanoparticle permeability in tumour vasculatures. *Nat. Nanotechnol.* 1–10 (2023).
105. Öörni, K. *et al.* Acidification of the intimal fluid: The perfect storm for atherogenesis. *J. Lipid Res.* **56**, 203–214 (2015).
106. Monopoli, M. P., Åberg, C., Salvati, A. & Dawson, K. A. Biomolecular coronas provide the biological identity of nanosized materials. *Nat. Nanotechnol.* **7**, 779–786 (2012).
107. Rampado, R., Crotti, S., Caliceti, P., Pucciarelli, S. & Agostini, M. Recent advances in understanding the protein corona of nanoparticles and in the formulation of "stealthy" nanomaterials. *Front. Bioeng. Biotechnol.* **8**, (2020).
108. Corbo, C. *et al.* The impact of nanoparticle protein corona on cytotoxicity, immunotoxicity and target drug delivery. *Nanomed.* **11**, 81–100 (2016).
109. Lazarovits, J. *et al.* Supervised learning and mass spectrometry predicts the in vivo fate of nanomaterials. *ACS Nano* **13**, 8023–8034 (2019).
110. Lazarovits, J., Chen, Y. Y., Sykes, E. A. & Chan, W. C. W. Nanoparticle–blood interactions: the implications on solid tumour targeting. *Chem. Commun.* **51**, 2756–2767 (2015).
111. Walkey, C. D. *et al.* Protein corona fingerprinting predicts the cellular interaction of gold and silver nanoparticles. *ACS Nano* **8**, 2439–2455 (2014).
112. Ngo, W. *et al.* Identifying cell receptors for the nanoparticle protein corona using genome screens. *Nat. Chem. Biol.* **18**, 1023–1031 (2022).
113. Poon, W. *et al.* Elimination pathways of nanoparticles. *ACS Nano* **13**, 5785–5798 (2019).
114. Ngo, W. *et al.* Why nanoparticles prefer liver macrophage cell uptake in vivo. *Adv. Drug Deliv. Rev.* **185**, 114238 (2022).
115. Le Floc'h, J. *et al.* In vivo biodistribution of radiolabeled acoustic protein nanostructures. *Mol. Imaging Biol.* **20**, 230–239 (2018).

Chapter 2

PHARMACOKINETICS AND PHARMACODYNAMICS OF ACOUSTIC BIOMOLECULES: THE ROLE OF BLOOD COMPONENTS

Ling, B.*; Ko, J. H.*; Stordy, B.; Zhang, Y.; Didden, T. F.; Malounda, D.; Swift, M. B.; Chan, W. C. W. C.; Shapiro, M. G. Pharmacokinetics and pharmacodynamics of acoustic biomolecules: the role of blood components. *In preparation.*

2.1 Abstract

Gas vesicles (GVs) are genetically encoded, air-filled protein nanostructures of broad interest for biomedical and clinical applications, acting as imaging agents for ultrasound, magnetic resonance, and optical techniques. However, the development of GVs as systemically injectable agents has been challenging due to an incomplete understanding of their interactions with blood components, which can significantly impact imaging performance. In this study, we investigate the dynamics of GVs in the bloodstream using a combination of ultrasound and optical imaging, surface functionalization, flow cytometry, and mass

spectrometry, focusing on the role of erythrocytes and serum proteins in shaping acoustic response, circulation time, and immunogenicity.

2.2 Introduction

Nanomaterials are becoming increasingly important for various biomedical applications, such as drug delivery, medical imaging, and diagnostics[1]. In these contexts, nanoparticle behavior is significantly impacted by cells and proteins encountered within the bloodstream. Serum proteins rapidly adsorb to nanoparticle surfaces, forming a protein corona that alters their physicochemical properties and recognition by the body[2–4]. The corona's composition predicts factors such as pharmacokinetics, biodistribution, toxicity, and cellular uptake[5–7]. Modification strategies often involve covering the particle surface with polymers such as polyethylene glycol (PEG) and other ligands[8]. Additionally, some nanomaterials bind to erythrocytes (RBCs), affecting imaging contrast[9], biodistribution[10], and circulation time[11].

Gas vesicles (GVs) are an emerging nanomaterial with great potential as agents for imaging and therapy[12]. These air-filled protein nanostructures are naturally produced by certain aquatic microbes for buoyancy regulation[13]. GVs comprise a 2-nm thick protein shell that excludes liquid water but permits the dynamic exchange of gas, forming a thermodynamically stable pocket of air with nanoscale dimensions[13]. Acoustic waves are strongly scattered at this air-water interface, enabling GVs to produce robust ultrasound contrast when injected into the body[14–16] or expressed in engineered cells[17,18]. Furthermore, they are resilient to repeated insonation[14], easily tailored to target molecular markers[19–21] or respond to biological functions[22,23], and have growing applications in therapeutic

ultrasound[24], optical imaging[25,26], and magnetic resonance imaging[27,28]. However, to effectively incorporate these capabilities into an injectable agent, a deeper understanding of GV behavior *in vivo* is needed.

In this study, we investigate GV interactions with RBCs and serum proteins, develop surface functionalization techniques to modulate these interactions, and evaluate the downstream effects on acoustic response, circulation time, and immunogenicity. Additionally, we characterize the GV protein corona and identify molecular pathways governing their behavior. This comprehensive analysis offers valuable insights for the ongoing development and optimization of injectable nanoparticle and GV-based agents.

2.3 Results

2.3.1 Gas vesicles adsorb to red blood cells

We began by studying the behavior of GVs after intravenous (IV) administration. We visualized circulating GVs with ultrafast power Doppler ultrasound imaging, leveraging their ability to enhance blood flow contrast[15]. Targeting a single coronal plane in the mouse brain, we acquired images at a 15 MHz center frequency and 0.25 Hz frame rate (**Fig. 2-1a**). After a 5 min baseline, we IV injected 100 μL of GVs purified from *Anabaena flos-aquae*[29] (OD 50, equivalent to 28 nM) and monitored the ensuing changes in hemodynamic signal. In healthy BALB/c mice, contrast reached an initial peak within 1 min, followed by a larger peak 3.5 min later, then returned to baseline over approximately 30 min as GVs were cleared by the liver[23] (**Fig. 2-1b**). Intensities at the first peak were consistent across trials but varied significantly at the second peak (**Fig. 2-1c**). This behavior also occurred in

immunocompromised NSG mice, suggesting an antibody-independent mechanism (**Fig. 2-S1**).

We next investigated the cause of this dual peak phenomenon. We hypothesized that the first peak was due to dispersion of free-floating GVs throughout the bloodstream, as this process is expected to occur within 15 seconds of injection[30], while the second peak arose from an increase in acoustic backscatter due to adsorption to RBCs, as seen with nanobubbles[9]. Consistent with our hypothesis, the scattering cross-section[31] of RBC-GV complexes—modeled as uniform spheres with volume-weighted physical properties—increased with the number of adsorbed GVs and was greater than that of dispersed particles (**Fig. 2-S2**). We quantified binding by exposing purified mouse RBCs to GVs modified to produce nonlinear ultrasound contrast[21]. The GVs were at concentrations approximating *in vivo* conditions after dispersion, while RBCs were maintained at 10% of *in vivo* levels to facilitate uniform mixing. After 1 h, we loaded the samples into an imaging phantom and detected GVs specifically with an amplitude modulation (AM) pulse sequence[32] (**Fig. 2-1d**). Signal intensities for RBC and GV controls were 0.04 AU and 8.24 AU, respectively, and increased to 10.62 AU after mixing. After centrifugation to remove unbound GVs, 23% (2.41 AU) of this signal was retained (**Fig. 2-1e**). We validated these results by incubating RBCs with GVs labeled with a fluorescent dye. After 1 h, we washed the cells thoroughly to remove loosely bound GVs and analyzed them by flow cytometry (**Fig. 2-1d, 2-S3**). Mean fluorescence of the population doubled from 0.53 to 1.17, with 0.5% of RBCs showing significant binding, further confirming our hypothesis (**Fig. 2-1f**). Taken together, our data suggest that increased acoustic backscatter from GV adsorption to RBCs contributes to the

delayed wave of hemodynamic contrast. This mechanism may operate in concert with others such as serum-induced aggregation, which we examine below.

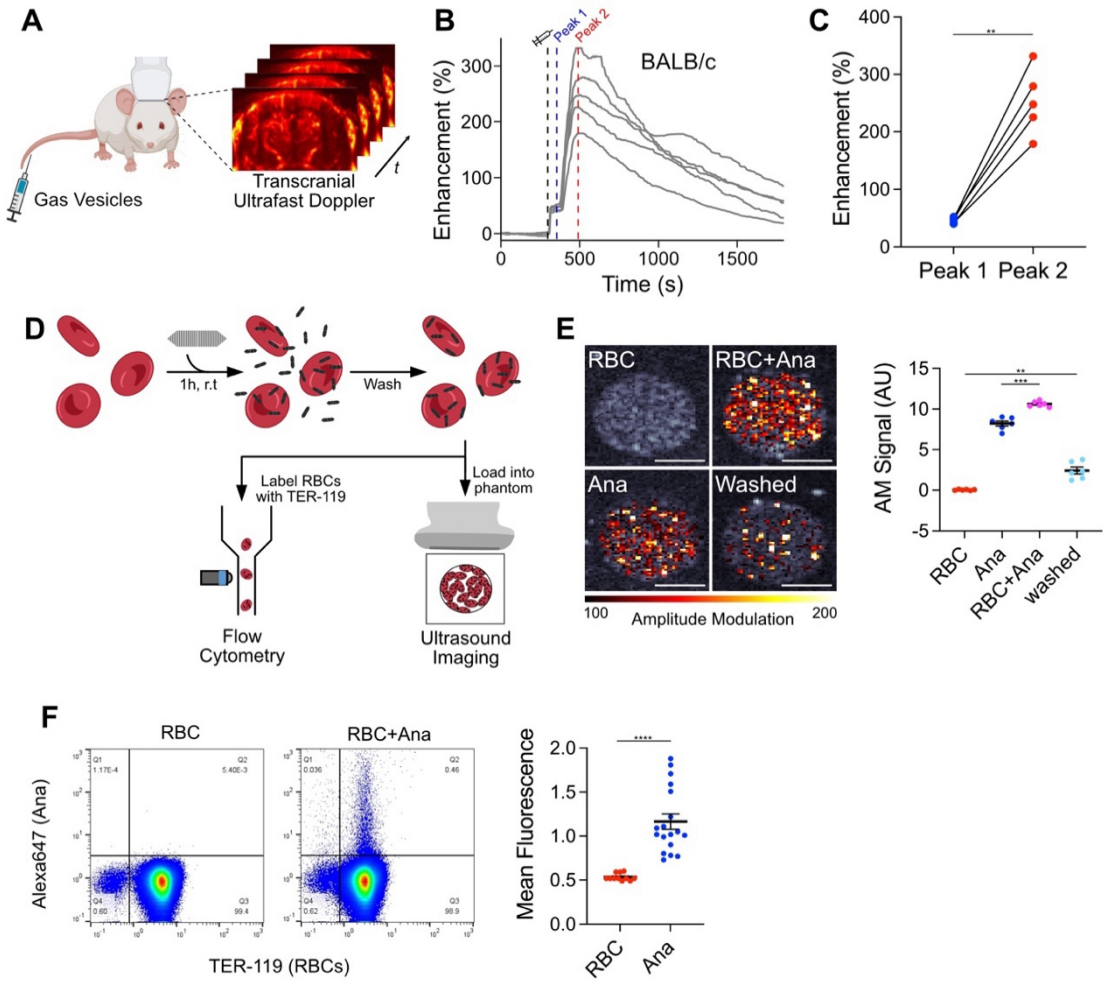

Figure 2-1. GV adsorption to RBCs results in a second wave of hemodynamic contrast. **A)** Diagram of *in vivo* imaging setup. Intravascular dynamics of IV injected GVs were visualized by transcranial ultrafast power Doppler imaging of the brain. **B)** Time courses of Doppler signal enhancement in immunocompetent mice following injection of 100 µL OD 50 GVs. N = 5. Dashed gray line, time of injection (300 s); dashed blue line, peak 1 (350 s); dashed red line, peak 2 (480 s). **C)** Signal enhancement at the indicated peaks in time courses from panel B. Points from the same trial are connected. N = 5. Paired t-test, (**, $p<0.01$). **D)** Diagram of RBC binding assay. Ultrasound imaging: RBCs were incubated with GVs modified to produce non-linear signal, washed by centrifugation, and loaded into an agarose phantom for nonlinear AM imaging. Flow cytometry:

RBCs were incubated with fluorescently-labeled GVs, washed by centrifugation, stained with anti-TER-119, and analyzed by flow cytometry. **E)** Acoustic detection of adsorbed GVs. Left: Representative ultrasound images of RBCs mixed with GVs. AM signal is overlaid on a conventional B-mode image. Scale bars, 1 mm. Right: Mean AM signal intensity within each well. N = 6. Error bars, ±SEM. Welch's t-test, (**, $p<0.01$; ***, $p<0.001$). **F)** Flow cytometric detection of GVs adsorbed to RBCs. Left: Representative dot plots of washed RBCs, gated for single cells. Right: Mean fluorescence of TER-119+ cell population. RBC, N = 11; RBC+Ana, N = 18. Error bars, ±SEM. Welch's t-test, (****, $p<0.0001$).

2.3.2 PEG-coated GVs do not interact with RBCs

To minimize RBC adsorption, we engineered GVs coated with methoxypolyethylene glycol (mPEG), a widely-used polymer for nanoparticle passivation[8]. We functionalized the GV surface with alkyne groups (**Fig. 2-S4**) and attached 10 kDa mPEG-azides through a copper-catalyzed azide-alkyne cycloaddition (CuAAC) (**Fig. 2-2a**). We will refer to unmodified GVs as Ana, and to functionalized GVs as Ana-PEG. Consistent with the addition of a PEG layer, dynamic light scattering showed an increase in hydrodynamic diameter from 240 nm to 370 nm (**Fig. 2-2b**), while zeta potential neutralized from −56 mV to −5 mV (**Fig. 2-2c**). We next performed pressurized absorbance spectroscopy, which measures optical density under increasing hydrostatic pressure to determine the threshold at which GVs collapse, providing a rapid measure of structural integrity[14,29]. Ana and Ana-PEG collapsed at 600 kPa and 450 kPa, respectively, suggesting that attachment of mPEG mildly destabilized the GV shell, but that most of its strength was intact (**Fig. 2-2d**). Incubation with mPEG or CuAAC reagents separately had no effect (**Fig. 2-S5**), while direct functionalization with NHS-PEG

severely compromised shell stability and failed to shield surface charge (**Fig. 2-S6**). B-mode ultrasound contrast from both GV types was equivalent (**Fig. 2-2e**).

Next, we evaluated the effectiveness of this coating at reducing RBC adsorption. As before, we mixed purified mouse RBCs with fluorescently-labeled Ana-PEG for 1 h, removed loosely bound GVs by centrifugation, and analyzed the cells by flow cytometry (**Fig. 2-1d**). Less than 0.1% of cells exhibited significant binding, with mean fluorescence of the population increasing only from 0.53 to 0.63, compared to 1.17 for Ana (**Fig. 2-2f**). Likewise, only 5% of AM signal intensity was retained after washing away unbound Ana-PEG, compared to 23% with Ana (**Fig. 2-2g**).

Having confirmed the reduced adsorption of Ana-PEG to RBCs, we assessed their *in vivo* behavior. Following IV injection of 100 µL OD 50 Ana-PEG into healthy BALB/c mice, hemodynamic contrast reached a maximum within 1 min before returning to baseline monotonically (**Fig. 2-2h**). The timing and magnitude of enhancement at this peak was consistent with the first peak observed after Ana injection (**Fig. 2-1b**), supporting our hypothesis that this initial peak resulted from vascular distribution. Unlike in the Ana time course, a second peak of contrast enhancement was not observed. Fitting these time courses

to an exponential decay model, we found that PEGylation increased half-life from 560 s to 840 s (**Fig. 2-2i, 2-S7**).

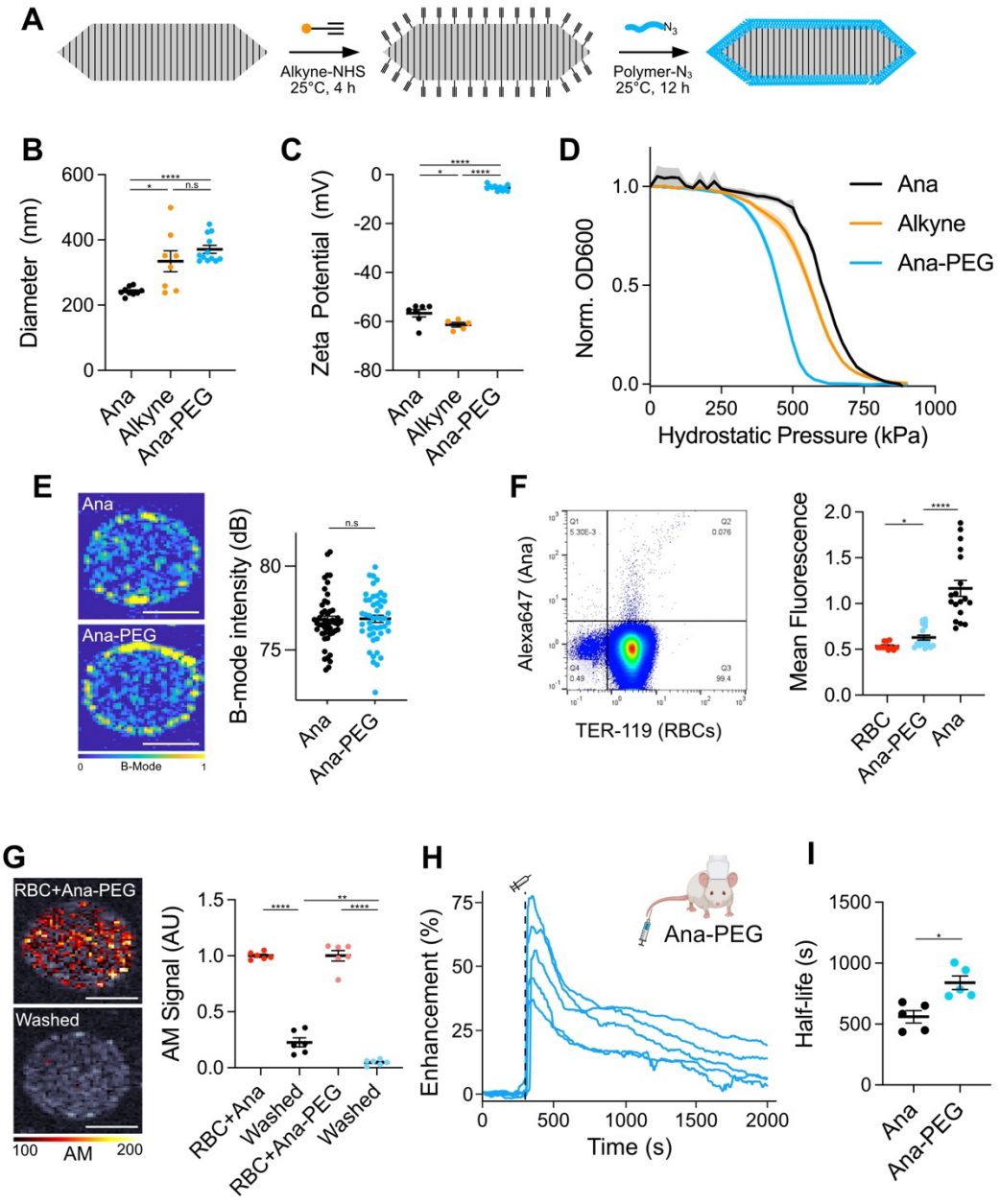

Figure 2-2. Surface passivation reduces RBC binding and extends circulation time. **A)** Reaction

scheme for GV functionalization. Alkynes were conjugated to lysines on the GV surface, and polymers were attached through a CuAAC reaction. **B)** DLS measurements of hydrodynamic diameter. N = 8–12. Error bars, ±SEM. Welch's t-test, (*, $p<0.05$; ****, $p<0.0001$; n.s, $p\geq0.05$). **C)** Zeta potential measurements of engineered GVs. N = 5–11. Error bars, ±SEM. Welch's t-test, (*, $p<0.05$; ****, $p<0.0001$). **D)** Normalized optical density at 600 nm as a function of hydrostatic pressure. N = 4. Thick lines, mean; shaded areas, ±SEM. **E)** Left: Representative B-mode images of Ana and Ana-PEG embedded in an agarose phantom. Right: Mean B-mode signal intensities within each well. N = 48. Error bars, ±SEM. Welch's t-test, (n.s, $p\geq0.05$). **F)** Flow cytometric detection of fluorescently-labeled Ana-PEG adsorbed to RBCs. Left: Representative dot plot of washed RBCs, gated for single cells. RBCs are stained with anti-TER-119. Right: Mean fluorescence of TER-119+ cell population. N = 18. Ana and RBC-only control from Fig. 2-1f are shown as a reference. Error bars, ±SEM. Welch's t-test, (*, $p<0.05$; ****, $p<0.0001$). **G)** Acoustic detection of Ana-PEG modified to produce nonlinear contrast. Left: Representative ultrasound images of RBCs mixed with Ana-PEG. AM signal is overlaid on a conventional B-mode image. Right: AM signal intensities, normalized to their respective washed samples. N = 6. Normalized data from Fig. 3-1e are shown as for comparison. Error bars, ±SEM. Welch's t-test, (**, $p<0.01$; ****, $p<0.0001$). **H)** Time courses of ultrafast power Doppler signal enhancement following injection of Ana-PEG into immunocompetent mice. N = 5. Dashed line, time of injection (300 s). **I)** Half-life of GV-induced signal enhancement calculated by fitting time courses in Fig. 2-1b (Ana) and Fig. 2-2h (Ana-PEG) to an exponential decay function. Error bars, ±SEM. Welch's t-test, (*, $p<0.05$).

2.3.3 Serum protein-mediated aggregation

GV aggregation is an alternative mechanism to increase acoustic backscatter[14] which cannot be excluded by the results presented thus far. Due to their highly charged surface (**Fig. 2-2c**), GV aggregation is unlikely to occur spontaneously[33] and would most likely be facilitated by a component within serum. To test this idea, we incubated Ana and Ana-PEG in 80% serum from naïve BALB/c, NSG, and outbred non-Swiss mice for 1 h at 37°C and measured flotation, a reliable indicator of clustering[14], by comparing optical density at the surface to the subnatant (**Fig. 2-3a**). We included NSG mice due to their lack of antibodies, while the genetic heterogeneity of outbred mice increases the likelihood of forming natural antibodies[34] against GVs. The optical density ratio was 1.1 for all samples prior to incubation and increased to 1.2 in BALB/c and NSG serum, though without statistical significance (**Fig.**

2-3b). In outbred serum, Ana formed a distinct buoyant layer with a ratio of 1.9, and Ana-PEG had a ratio of 1.3. Transmission electron microscopy (TEM) images before incubation showed only discrete particles, while outbred serum caused Ana to assemble into multi-GV bundles (**Fig. 2-3c**). Ana-PEG formed occasional small clusters but remained mostly dispersed. To compare acoustic response, we embedded GVs treated with either PBS or outbred serum into an imaging phantom and acquired ultrasound images using a conventional B-mode sequence (**Fig. 2-3d**). The signal intensity from Ana increased by 6.13 dB in outbred serum relative to PBS, while contrast from Ana-PEG remained relatively unchanged. Signal from Ana increased by 2.26 dB in BALB/c serum, consistent with a lower degree of aggregation relative to outbred serum (**Fig. 2-S8**).

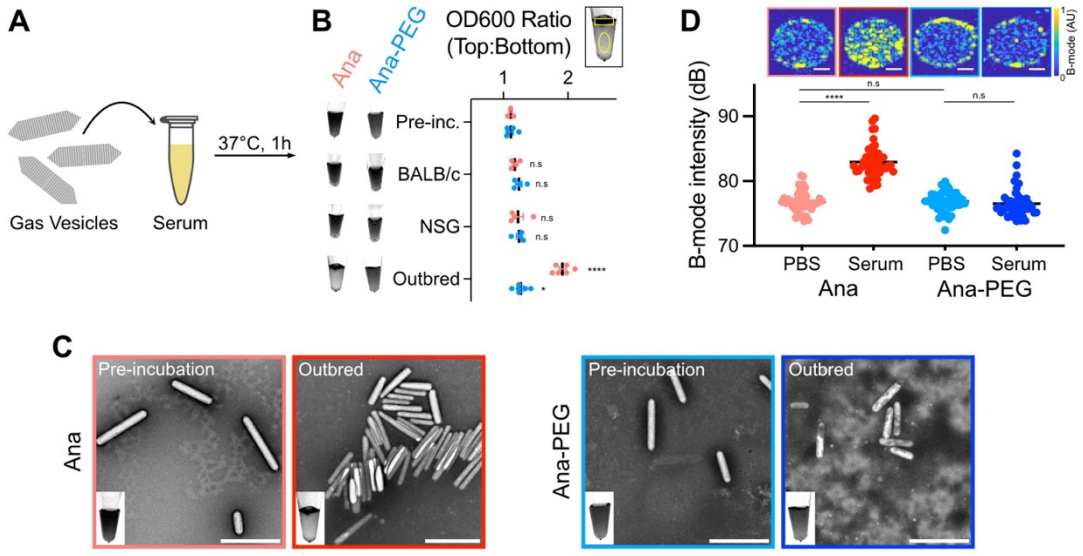

Figure 2-3. Serum exposure can cause GVs to aggregate. **A)** Diagram of serum incubation assay. GVs (OD 2) were incubated in 80% mouse serum for 1 h at 37°C. **B)** Optical detection of GV

flotation. Left: Representative trans-illumination images of serum-incubated GVs. Right: Ratio of optical densities in manually drawn ROIs at the surface and in the subnatant of each sample. Representative ROIs are shown above the plot. Error bars, ±SEM. Welch's t-test, compared to pre-incubation samples (*, $p<0.05$; ****, $p<0.0001$; n.s, $p\geq0.05$). **C)** Representative TEM images of GVs before and after exposure to serum from outbred mice. Inset shows trans-illumination image of corresponding sample. Scale bars, 500 μm. **D)** Ultrasound imaging of GVs following incubation in PBS or outbred mouse serum. Top: Representative B-mode images. Scale bars, 1 mm. Bottom: Mean signal intensity within each well. N = 48. Error bars, ±SEM. Welch's t-test, (****, $p<0.0001$; n.s, $p\geq0.05$).

2.3.4 Immunogenicity and effect of antibodies in vivo

We next investigated the impact of antibodies on GV dynamics *in vivo* by administering multiple GV injections. We injected BALB/c mice with an initial dose of 100μL OD 50 GVs and did so again 1 or 4 weeks later (**Fig. 2-4a**). Ana injections resulted in peak enhancements of approximately 280% at all three timepoints (**Fig. 2-4b–c**), with apparent circulation half-life decreasing from 560 s to 290 s and 410 s at weeks 1 and 4, respectively (**Fig. 2-4d**). Repeated Ana injections were well-tolerated, with no anomalies observed by veterinary assessment.

Ana-PEG produced peak enhancements of approximately 50% at all three timepoints (**Fig. 2-4e, 2-S9**). Unexpectedly, acute hypotension occurred several minutes after the second injection of Ana-PEG, resulting in a sharp reduction in hemodynamic contrast (**Fig. 2-4e**). Only 20% of mice recovered from hypotension at week 1 and 60% at week 4 (**Fig. 2-4f**). Based on similar responses to other PEGylated materials[35,36], we hypothesized that this reaction is triggered by anti-PEG antibodies. To test this hypothesis, we exposed GVs to serum prepared from mice 10 days post-immunization (**Fig. 2-4g**). In the presence of Ana-PEG antiserum, Ana-PEG aggregated and formed a buoyant layer within 30 min while Ana

remained in suspension, suggesting minimal cross-reactivity between anti-PEG antibodies and the Ana GV surface. Conversely, when exposed to Ana antiserum, Ana-PEG remained in suspension while Ana aggregated, further supporting the distinction in antibody selectivity for the different GV surfaces. Substituting mPEG with a 16 kDa zwitterionic polymer, which is being explored as a less immunogenic PEG alternative[37,38], did not alleviate anaphylaxis (**Fig. 2-S10**).

Taken together, our data suggest that the primary contributor to GV-enhanced hemodynamic contrast is RBC adsorption, while serum components mediate clearance and elicit immunogenic responses. This conclusion is supported by the comparable hemodynamic contrast dynamics observed in both immunocompetent BALB/c mice and antibody-deficient NSG mice after GV administration (**Fig. 2-S1**). Furthermore, peak enhancement was unaffected by the presence of serum components that cause significant GV

aggregation (**Fig. 2-4c, g**). Instead, these mice experienced accelerated GV clearance and, in the case of Ana-PEG, infusion reactions (**Fig. 2-4b, e**).

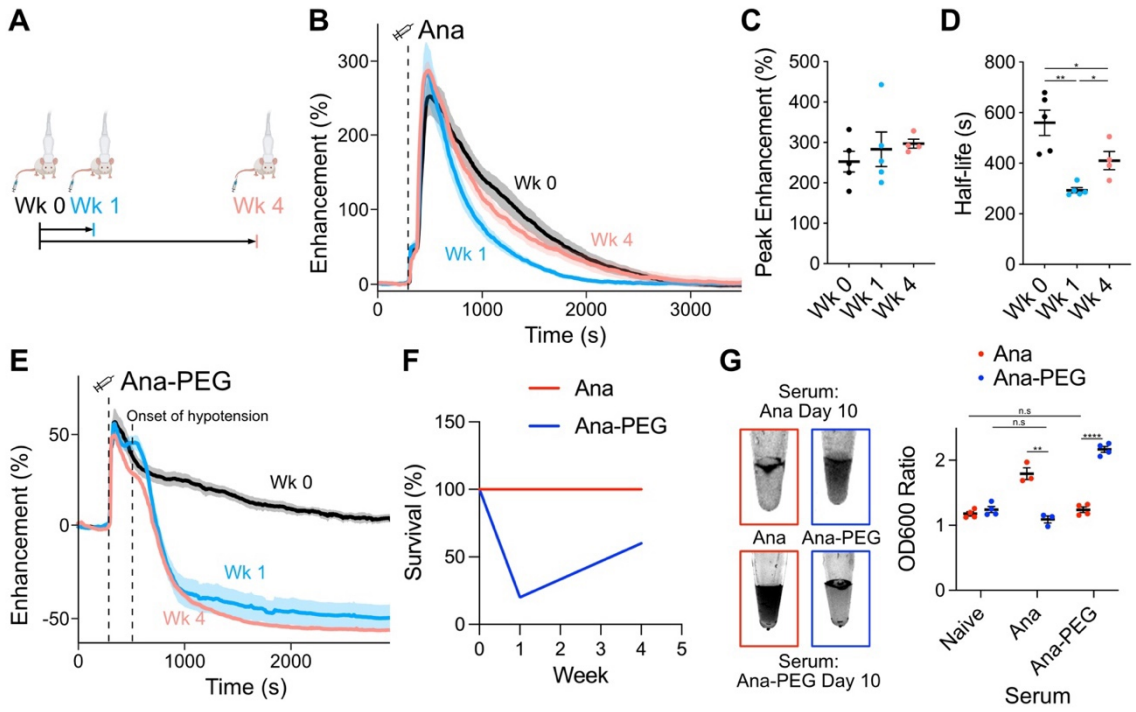

Figure 2-4. Immunogenicity of GVs. **A)** Timeline of GV injections. Immunocompetent mice were injected with two doses of 100 µL OD 50 Ana or Ana-PEG, separated by either 1 or 4 weeks. Ultrafast Doppler imaging was performed at each injection. **B)** Time courses of hemodynamic signal enhancement following administration of Ana. Thick lines, mean; shaded area, ±SEM; dashed line, time of injection (300 s). N = 4-5. **C)** Peak enhancement of time courses in panel B. Error bars, ±SEM. **D)** Circulation half-life calculated by fitting time courses in panel B to an exponential decay function. Error bars, ±SEM. Welch's t-test, (*, $p<0.05$; **, $p<0.01$). **E)** Time courses of hemodynamic signal enhancement following administration of Ana-PEG. Severe hypotension (dashed red line) occurs within 5 min of injection, resulting in a sharp drop in hemodynamic signal. Thick lines, mean; shaded area, ±SEM; dashed line, time of injection (300 s). N = 4-5. **F)** Survival rate following GV administration. All mice dosed with Ana recovered after both injections (N = 5 at each time point). Several mice dosed with Ana-PEG did not recover after the second injection (N = 5 at each time point). **G)** GV aggregation in the presence of anti-GV antibodies. Left: Representative trans-illumination images of GVs incubated in serum prepared from mice 10 days post-immunization. Right: Ratio of optical density at the surface relative to the

subnatant. Values from incubation in naïve BALB/c serum (Fig. 2-3b) are included for comparison. N = 3-4. Error bars, ±SEM. Welch's t-test, (**, $p<0.01$; ****, $p<0.0001$; n.s, $p\geq0.05$).

2.3.5 Protein corona of GVs is dominated by immune response proteins

To identify the serum components influencing GV behavior, we characterized the protein coronas associated with Ana and Ana-PEG. We incubated both GV types in serum from outbred mice for 1 h at 37 °C, as it offers a more diverse representation of serum components and enhances generalizability for translational applications[39]. After removing unbound proteins by centrifugation, we digested bound proteins with trypsin and quantified peptides by liquid chromatography tandem mass spectrometry (LC-MS/MS) (**Fig. 2-5a**). Levels of detected proteins showed moderate correlation between GV types (R = 0.77) but less so with serum (Ana R = 0.58, Ana-PEG R = 0.45) (**Fig. 2-S11**), indicating that Ana and Ana-PEG enrich for similar proteins through a process that cannot be explained by serum concentration alone. We detected comparable amounts of the GV structural protein gvpC across all samples, indicating similar GV loading, as well as minor quantities of gvpV, gvpN, and other cyanobacterial proteins (**Fig. 2-S12**).

Immune response proteins—part of an immunoglobulin complex or involved in complement activation—were highly abundant in the Ana corona, constituting 43.0% of detected proteins, compared to 14.0% of the Ana-PEG corona and 22.2% of serum (**Fig. 2-5b**). Of the proteins enriched by Ana over Ana-PEG, 24 of 27 were associated with immune response, including immunoglobulin A, immunoglobulin G, immunoglobulin kappa, mannose-binding protein C, and complement C1r (**Fig. 2-5c–d**). Similarly, 13 of the top 25

proteins enriched on Ana relative to serum were in this group (**Fig. 2-S13**). In contrast, only one immune response protein was among the 32 proteins more abundant on Ana-PEG than Ana. Consistent with its role as a natural antibody[40], immunoglobulin M (IgM) was the most prevalent member of this group, accounting for 15% of the Ana corona (1st overall) and 4% of the Ana-PEG corona (8th overall). Given its enrichment and multivalency, IgM is likely responsible for GV aggregation.

Lipid transport proteins were enriched on both GV types, comprising 23.1% and 38.6% of the Ana and Ana-PEG coronas, respectively, compared to 5.2% of serum (**Fig. 2-5b**). Apolipoprotein E (ApoE) and apolipoprotein C-I (ApoC-I) were the most prominent. On Ana, they ranked 2nd and 4th in overall abundance with 130-fold and 50-fold enrichment relative to serum, respectively (**Fig. 2-S13**). On Ana-PEG, they were 1st and 2nd with 200-fold and 90-fold enrichment, respectively. Ana-PEG also enriched several other proteins that are typically found in low concentration in serum, such as apolipoprotein C-II, apolipoprotein

C-III, platelet factor 4, and profilin-1 (**Fig. 2-5d, 2-S13**). Neither GV type appreciably adsorbed albumin despite its high concentration in serum.

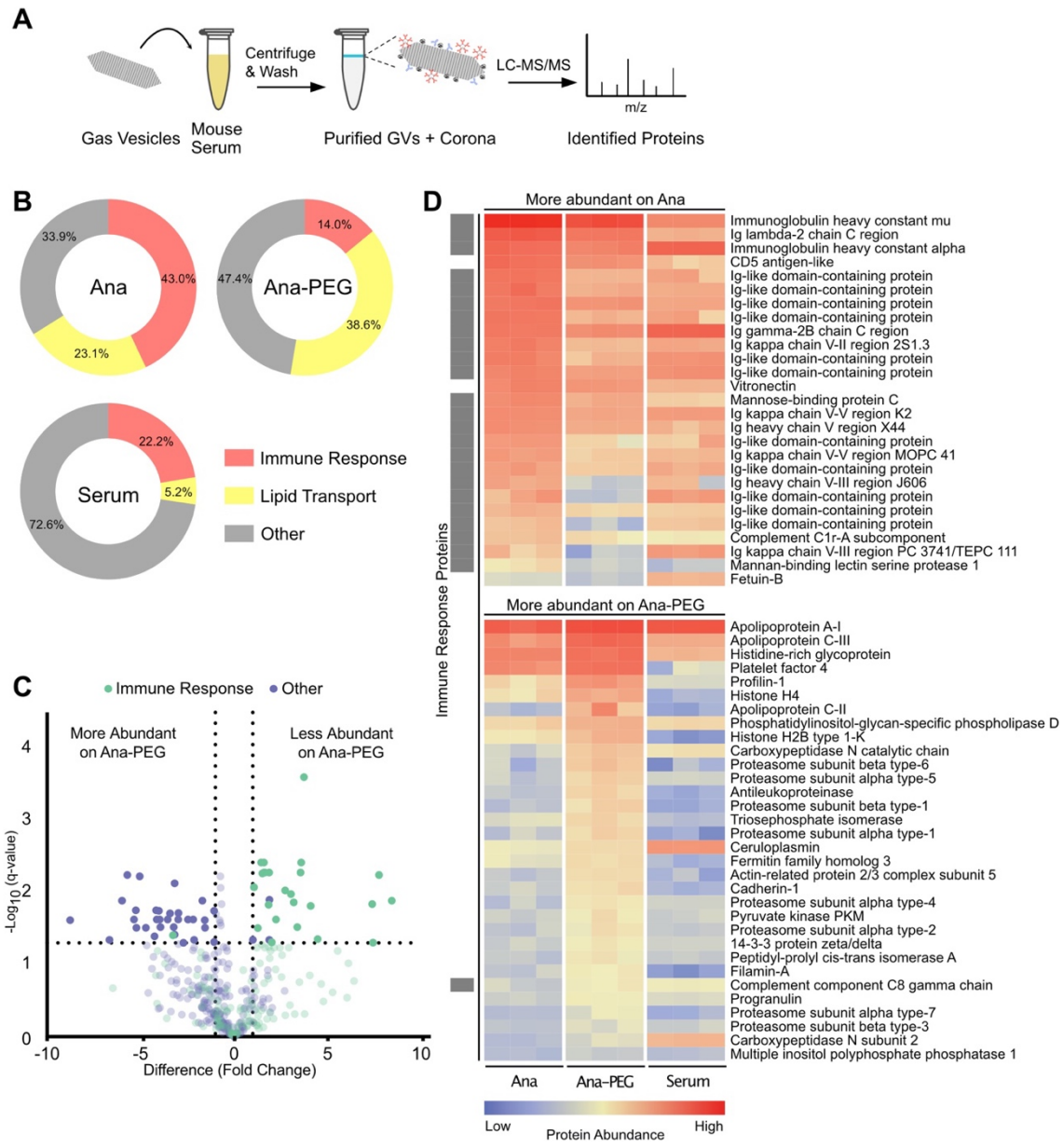

Figure 2-5. Characterization of the GV protein corona. **A)** Schematic of corona analysis protocol. GVs were incubated in outbred mouse serum for 1 h at 37°C, purified by centrifugation, and processed for LC-MS/MS. **B)** Donut charts of relative abundances of immune response and lipid transport proteins, as classified by gene ontology. **C)** Volcano plot of protein abundance on Ana compared to Ana-PEG. Abundances were compared by multiple unpaired t-test analysis using the false discovery rate method of Benjamini and Hochberg. Proteins with a false discovery rate of 5% and $\log_2$ fold-change greater than 1 were deemed differentially abundant. Proteins that were not differentially abundant are shown translucently. **D)** Heat map of differentially abundant proteins on Ana compared to Ana-PEG, shown with a mouse serum control. Immune response proteins are indicated by a gray box on the left.

2.4 Discussion

Our results demonstrate that blood components significantly influence GV behavior in the blood stream, highlighting opportunities for optimizing GV-based diagnostic and therapeutic agents. Injected GVs rapidly adsorb to RBCs, resulting in large hemodynamic contrast enhancement. Additionally, GVs acquire a serum protein corona that is rich in apolipoproteins and immunoglobulins. This corona facilitates rapid clearance and enhanced immune response upon repeated exposure. Surface passivation reduces RBC and protein adsorption, providing a modest extension of circulation time at the expense of diminished blood flow contrast.

GV-based diagnostic agents could benefit from strategies to modify the protein corona, which can mask elements required for molecular detection and response. Potential techniques include genetic functionalization of the GV surface[21], ligand conjugation to serum-equilibrated GVs[41], fusion of peptides to recruit specific serum proteins[42], and adsorption of an artificial corona[43]. These strategies could also enable *in vitro* diagnostic applications, such as clustering-based detection in which GVs selectively enriched with specific proteins are combined with the corresponding antibodies, allowing for rapid optical

and acoustic measurements via flotation and enhanced ultrasound backscatter[14,44], respectively. Furthermore, the GV corona can aid in proteomics by reducing the dynamic range of protein concentrations in biological fluids, facilitating detection of low-abundance components[45]. GVs are advantageous for these applications due to easy buoyancy-based isolation and use of structural proteins as internal concentration standards.

To maximize the translational utility of GVs, immunogenic components should be identified and eliminated. However, it remains unclear whether GVs alone are immunogenic, as other residual cyanobacterial proteins persist after purification. Future work could study responses to urea-treated GVs lacking these proteins[29], identify problematic epitopes by analyzing peptides displayed on antigen-presenting cells after lysosomal processing of the GV[46], and redesign production and purification processes to address these challenges.

Enhancing GV binding to RBCs could potentially alleviate immunogenicity concerns by inducing peripheral tolerance[47,48], while also improving contrast in functional ultrasound imaging[15] and extending GV circulation time[49,50]. Approaches include covalent linkage to engineered RBCs[49] or incorporating RBC affinity ligands to enhance binding in situ[50]. Future work should examine the impact of GV adsorption on RBC structure and function, including morphology, longevity, and gas exchange.

In conclusion, our study uncovered key insights into GV interactions with blood components, uncovering the mechanisms underlying their recognition by the body and the delicate balance between circulation half-life and contrast enhancement. By understanding

the impact of these interactions on safety and efficacy, we move closer to optimizing GV performance as injectable agents and realizing the full potential of this promising technology.

2.5 Methods

Chemicals

All chemicals were purchased from Sigma-Aldrich and used without further purification unless otherwise noted.

GV preparation

Native gas vesicles were isolated from *Anabaena flos-aquae* as previously described and stored in 1x phosphate-buffered saline (PBS)[29]. Concentrations were measured by optical density at 500 nm with a NanoDrop ND-1000 (Thermo Scientific). The following relations were used for stoichiometry calculations: OD 1 GV = 114 pM GV = 4.41 uM gvpA. GVs producing nonlinear contrast were prepared by removing gvpC as previously described[21]. Fluorescently labeled GVs were prepared by adding 90 μM Alexa Fluor 647 N-hydroxysuccinimide ester (Invitrogen, prepared as 10 mM stock solution in DMSO) to a suspension of OD 30 GVs (5000 dye per GV). After rotating gently at room temperature for 2 h, excess dye was removed by two rounds of overnight dialysis through a regenerated cellulose membrane (12-14 kDa MWCO, Repligen) followed by two rounds of centrifugation.

Polymer coating

GV-alkynes were prepared by adding 26.46 mM propargyl-N-hydroxysuccinimide ester (250 mM stock solution in DMSO) to a suspension of OD 50 GVs (120 alkyne/gvpA). After

rocking gently for 4 h at room temperature, the GVs were purified by 4 rounds of centrifugation (600xg, 2h).

For a typical CuAAC reaction, 55.5 mg m-PEG-azide (10 kDa, BroadPharm), 110 µL DMSO, 12 µL PBS, and 54 µL aminoguanidine hydrochloride[51] (11.11 mg/mL in PBS) were combined in a 2 mL microcentrifuge tube. 60 µL of $CuSO_4$ pentahydrate (7.4 mg/ml in water) was mixed with 60 µL BTTAA[52] (Click Chemistry Tools, 77.4 mg/ml in PBS) in a PCR tube, and 108 µL of this mixture was added to the reaction. After the mPEG dissolved completely, 1.5 mL GVs (OD 50) and 54 µL sodium ascorbate (59.4 mg/mL freshly made in PBS) were added. The mixture was rotated slowly overnight at room temperature and purified by 4 rounds of centrifugation (600xg, 2h). Other polymer formulations were similarly prepared.

GV characterization

Dynamic light scattering: A disposable cuvette containing 300 µL of a GV suspension diluted to approximately OD 0.2 was placed in a ZetaPALS particle analyzer and analyzed with the ZetaPALS Particle Sizing software using an angle of 90°, thin shell setting, run length of 15 s, and 6 runs per sample.

Zeta potential: An electrode (SZP, Brookhaven Instruments) was inserted into a mixture of 50 µL of OD 2 GVs and 1500 µL Milli-Q water in a disposable cuvette (BI-SCP, Brookhaven Instruments). Measurements were performed with a ZetaPALS particle analyzer (Brookhaven Instruments) running the ZetaPALS Zeta Potential software. Charge was calculated using the Smoluchowski model from 5 runs of 15 cycles.

Pressurized absorbance spectroscopy: 350µL OD 0.3 GVs were added to a flow-through quartz cuvette with a path length of 1 cm (Hellma Analytics). Hydrostatic pressure was applied from a 1.5 MPa nitrogen gas source through a single valve pressure controller (PC series, Alicat Scientific). Pressure was ramped from 0 to 900 kPa in 25 kPa increments with

a 7 s equilibration period prior to measurement of absorbance at 600 nm with a microspectrometer (STS-VIS, Ocean Optics). Data were normalized to absorbance at 0 kPa and 900 kPa. Midpoint of collapse was derived from linear interpolation at normalized OD of 0.5.

TEM: GVs were buffered exchanged into water and diluted to approximately OD 0.5. 3 μL of sample was spotted onto Formvar/carbon 200 mesh copper grids (#0801, Ted Pella) that were rendered hydrophilic by treatment with oxygen plasma (K100X, Emitech). After 90 s, sample was wicked off and stained for 1 min with 3 μL 1% uranyl acetate solution. Grids were imaged using a Tecnai T12 LaB6 120 kV transmission electron microscope (FEI Company) equipped with a Gatan UltraScan 2000 x 2000 CCD camera and DigitalMicrograph software interface (v3.9.0, Gatan Inc). Images were processed with FIJI[53].

MALDI-MS: Matrix-assisted laser desorption/ionization mass spectrometry (MALDI-MS) analysis of GV and GV-alkyne was performed with a Bruker Autoflex MALDI-time-of-flight mass spectrometer in linear positive ion mode. The GV sample was desalted by repeated flotation purification using 0.1% v/v TFA in water and concentrated to about OD_{500} = 100. The GV sample was mixed 1:5 with sinapinic acid (10 mg/mL) dissolved in 30% acetonitrile + 0.01% TFA. The mixture was sonicated for 10 min and spotted onto the MALDI target plate.

Small molecule and polymer synthesis

Synthesis of CTA1 (**Fig. 2-S14**): 4-Cyano-4-(ethylsulfanylthiocarbonyl) sulfanylvpentanoic acid N-hydroxysuccinimide ester[54] (600 mg, 1.66 mmol, 1 equiv) was dissolved in 10 mL dichloromethane, and 1-azido-3-aminopropane[55] (183 mg, 1.83 mmol, 1.1 equiv) and triethylamine (0.58 mL, 4.16 mmol, 2.5 equiv) were added. The mixture was stirred at 23 °C

for 14.5 h. The mixture was purified by column chromatography (3:2 hexanes:ethyl acetate) to yield the product as orange oil (404 mg, 1.17 mmol, 70.4% yield).

Synthesis of zwitterionic polymer (**Fig. 2-S15**): The polymer was synthesized by reversible addition-fragmentation chain transfer (RAFT) polymerization. The monomer[56] (1.765 g, 5.010 mmol, 58 equiv), **CTA1** (30 mg, 0.086 mmol, 1 equiv), and AIBN (2.8 mg, 0.017 mmol, 0.2 equiv) were dissolved in DMSO (5.4 mL) and freeze-pump-thawed three times. The polymerization under argon atmosphere was initiated by immersing the flask into a 70 °C oil bath. The polymerization was quenched after 4.5 h by freezing with liquid nitrogen and exposing to air. The reaction mixture was precipitated into cold acetone, then the precipitate was redissolved in methanol and precipitated into cold ether. The precipitate was dried *in vacuo* to yield the *tert*-butyl ester protected polymer (926 mg). The carboxylate groups on the polymer was deprotected by stirring the polymer (750 mg) in 1.5 mL TFA at 23 °C for 1 h, then neutralized with NaOH solution. The polymer was purified by dialysis in water (MWCO 3.5 kDa Spectra/Por regenerated cellulose membrane, Spectrum Chemical, New Brunswick NJ). The water was removed by lyophilization to yield the polymer.

Characterization: Mass spectrometry of **CTA1** was performed on a JEOL JMS-T2000GC AccuTOF GC-Alpha system using FD ionization. Infrared (IR) spectra were recorded on a Perkin Elmer Paragon 1000 spectrometer using neat samples on ATR diamond, and are reported in frequency of absorption (cm^{-1}). ^{1}H NMR spectra were recorded on a Varian Inova 500 spectrometer (500 MHz), and ^{13}C NMR spectrum was recorded on a Bruker Ascend 400 spectrometer with Prodigy broadband cryoprobe (400 MHz)

In vitro ultrasound imaging

Images were acquired using a 128-element linear array probe (L22-14vX, Verasonics) with a center frequency of 18 MHz, elevation focus of 8 mm, elevation width of 1.6 mm, and

element pitch of 0.10 mm. The transducer was connected to a programmable ultrasound scanner (Verasonics Vantage 128) operating on Vantage 4.4.0 software.

Phantoms were cast out of 1% agarose in PBS using custom printed molds containing pairs of 2-mm diameter cylindrical wells. Samples for imaging were mixed 1:1 with 2% low melt agarose in PBS, incubated for 10 s at 42°C, and quickly loaded into the wells. After solidification, the phantoms were placed on top of an acoustically absorbent material and immersed in PBS to couple the sample with the imaging transducer. Linear imaging was performed using a conventional B-mode pulse sequence consisting of 89 ray lines, each transmitted from a 40-element aperture at 18 MHz as a 2.5 cycle pulse with an 8-mm focus. Nonlinear imaging was performed with the same parameters using an amplitude modulation pulse sequence[32].

The imaging sequence for each sample consisted of 10 frames acquired at a transmit voltage of 1.6 V, 20 frames at 20 V, and 10 more frames at 1.6 V. Circular regions of interest were drawn in each well, and signal intensities were calculated by subtracting average pixel value across the last 10 frames from that of the first 10 frames.

In vivo imaging

All *in vivo* experiments were performed under protocols approved by the Institutional Animal Care and Use Committee at the California Institute of Technology. Imaging experiments were performed on 8-12 week old female BALB/cJ mice (Jackson Laboratory) and 12 week old male NSG mice (Jackson Laboratory).

Mice were maintained under 1.5% isoflurane anesthesia on a temperature-controlled imaging platform set to 38.5°C (Stoelting Co.) and head-fixed in a stereotaxic frame (Knopf). A catheter with a 30G needle was inserted into a lateral tail vein and the mouse was depilated with Nair, taking care to limit contact time to minimize scalp injury. A high-frequency transducer (L22-14vX, Verasonics) was coupled to the head through a column of ultrasound

gel (centrifuged at 300xg, 20 min to remove bubbles) and positioned to capture a full coronal section at an arbitrary plane along the rostrocaudal axis.

Ultrafast power Doppler images were acquired at 0.25 Hz as previously described[15,23]. Briefly, the pulse sequence consisted of 11 tilted plane waves varying from −10° to 10°. Each plane wave contained 4 cycles transmitted at a center frequency of 15 MHz with a voltage of 3 V. An ensemble of 250 coherently compounded frames, collected at a frame rate of 500 Hz, was processed through a singular value decomposition filter (cutoff of 20) to produce a single power Doppler image. GVs (100 μL OD 50) were manually injected as a bolus 300 s after the start of acquisition. For multiple injection experiments, mice were given a second dose of GVs after 1 or 4 weeks.

Pixel-wise signal enhancement was calculated as the ratio of intensity at each time point relative to mean intensity in the first 75 frames. Time courses were extracted by averaging signal enhancement within a manually drawn region of interest encompassing the cortex. Each curve was smoothed using a 20-unit median filter. To calculate half-life, an exponential decay function was fitted to each curve from its maximum to the end of acquisition.

RBC incubation

Whole blood was collected from 8-12 week old female BALB/c mice by cardiac puncture using EDTA as an anti-coagulant. 500 μL of blood was aliquoted into 2 mL microcentrifuge tubes, diluted with 1.3 mL PBS, and centrifuged at 1000xg for 10 min. After discarding the supernatant, the cells were resuspended to approximately 1.8 mL in PBS and centrifuged again. After repeating this process once more, the RBCs were resuspended in PBS to approximately 4x the volume of the cell pellet (25% hematocrit).

Ultrasound imaging: 10 μL purified RBCs were mixed with 50 μL OD2 GVs which were urea-treated to produce nonlinear contrast. After incubating at room temperature for 1 h,

samples were diluted with 900 µL PBS and centrifuged at 200xg for 8 minutes. The supernatant was removed, and this wash process was repeated once before concentrating the samples to approximately 60 µL. RBC only controls were prepared by mixing 10 µL RBCs with 50 µL PBS. GV only controls were prepared by mixing 50 µL OD2 GVs with 10 µL PBS. As described above, samples were loaded into phantoms and imaged using an amplitude modulation pulse sequence.

Flow cytometry: Purified RBCs were washed and resuspended to approximately 1e10 cells/mL in 1%w/v bovine serum albumin (BSA) in Hanks' Balanced Salt Solution (HBSS, Gibco). 10 µL OD10 GVs labeled with AF647, 10 µL RBCs, and 80 µL HBSS were combined in a 1.5 mL microcentrifuge tube. After incubating at 37°C for 1 h, samples were diluted with 1 mL HBSS and centrifuged at 600xg for 10 min. The supernatant was removed, and this wash process was repeated two more times before suspending in 100 µL 1% BSA in HBSS. RBCs were labeled with 0.2 µL FITC anti-mouse TER119 (BioLegend cat#116205) for 30 minutes at room temperature. Samples were washed by three rounds of centrifugation and resuspended in 1 mL 1% BSA/HBSS. 50 µL of each sample was analyzed on a MACSQuant Analyzer 10 Flow Cytometer (Miltenyi Biotec) using the B1 and R1 channels for FITC-TER119 and AF647-GV, respectively. Data were analyzed in FlowJo. Single cells were isolated by FSC-H vs. FSC-A and displayed as R1-H vs. B1-H.

Serum incubation

GVs (5 µL OD10) were mixed with 45 µL mouse serum and incubated undisturbed for 1 h at 37°C. Outbred mouse serum was purchased from Sigma Aldrich. To prepare serum from BALB/c and NSG mice, blood was extracted by cardiac puncture, allowed to clot at room temperature for 15 min, centrifuged at 1000xg for 10 min, and the supernatant was carefully

collected by pipette. GV antisera were prepared from BALB/c mice 10 days after immunization with 100 µL OD 50 Ana or Ana-PEG.

Trans-illumination images were acquired before and after incubation using a Chemi-Doc gel imager (Bio-Rad). For ultrasound imaging, the samples were gently mixed, loaded into a phantom, and imaged as described above using a B-mode pulse sequence. (commercial or freshly prepared from BALB/c or NSG mice by cardiac puncture)

LC-MS/MS

GVs (100 µL OD50) were mixed with normal mouse serum and incubated for 1 h at 37°C under gentle rotation. GVs were purified, exchanged into water, and concentrated over 4 rounds of centrifugation. 20 µL of these samples were transferred to 1.5 mL Low Protein Binding microcentrifuge tubes, resuspended in 980 µL of ultrapure water (Barnstead GenPure 18.2 $M\Omega cm^{-1}$), and centrifuged at 600xg for 30 min. After removing the subnatant, the GVs were resuspended to a total volume of approximately 74 µL with ultrapure water. Mouse serum controls were prepared by diluting 100 µL of the mouse serum into 900 µL of ultrapure water, then transferring 10 µL of this solution into three 1.5 mL Low Protein Binding microcentrifuge tubes (Sarstedt, Thermo Fisher) and diluting to 74 µL with ultrapure water. 10 µL of 500 mM ammonium bicarbonate, 10 µL of 10% (w/v) sodium deoxycholate (Fluka Analytical), and 4 µL of 250 mM dithiothreitol (Bio Basic) were added to each tube. The samples were incubated at 80°C for 10 minutes, then cooled to room temperature. 10 µL of 450 mM iodoacetamide was added to each sample. The samples were incubated for 30 minutes in the dark at room temperature, then 2 uL of Sequencing Grade Modified Trypsin (Promega) was added to each sample. After incubating overnight in the dark at room temperature, 100 µL of ethyl acetate followed by 5 µL of 10% (w/w) formic acid was added to each sample. The samples were vortexed for 1 minute to mix thoroughly, then centrifuged at 1000xg for 10 minutes to allow the aqueous and organic phases to fully separate. The organic (supernatant) phase was removed by pipette, and the aqueous layer was transferred

to fresh 1.5 mL Low Protein Binding microcentrifuge tubes. Samples were stored at −20°C prior to characterization.

Digested peptides were submitted to the SPARC BioCentre (The Hospital for Sick Children, Peter Gilgan Centre for Research and Learning) for LC–MS/MS using an Orbitrap Fusion Lumos Tribrid Mass Spectrometer (Thermo Scientific). Data were analyzed using Proteome Discoverer v.2.5.0.400. Peptides were identified by searching against mouse (Uniprot_UP000000589_Mouse_15092020) UniProt reference databases.

A minimum protein confidence threshold of 95%, a minimum of 2 identified peptides, and a minimum peptide confidence threshold of 95% were used. Spectral counts and precursor intensity of each protein were analyzed using intensity-based absolute quantification (iBAQ) with Scaffold v.5.2.0 (Proteome Software Inc.). Gene Ontology Annotations for Mouse (https://www.ebi.ac.uk/GOA/downloads), downloaded October 10, 2022, were used to determine whether proteins were associated with immune response. Proteins annotated as part of an immunoglobulin complex, involved in complement activation, or involved in complement binding were deemed to be associated with immune response. Donut plots were created based on the geometric mean of abundance for each protein across the three replicates. The quantified protein data were log2-transformed and analyzed with Perseus v2.0.7.0 (MaxQuant).

A multiple unpaired t-test analysis using the false discovery rate method of Benjamini and Hochberg was used to identify differentially abundant proteins on the two gas vesicle types.

Proteins identified with a false discovery rate of 5% and a log2 fold-change greater than 1 were deemed differentially abundant.

Statistical analysis

Sample sizes were chosen based on preliminary experiments to yield sufficient power for the proposed comparisons. Statistical methods are described in applicable figure captions.

2.6 Supplementary Information

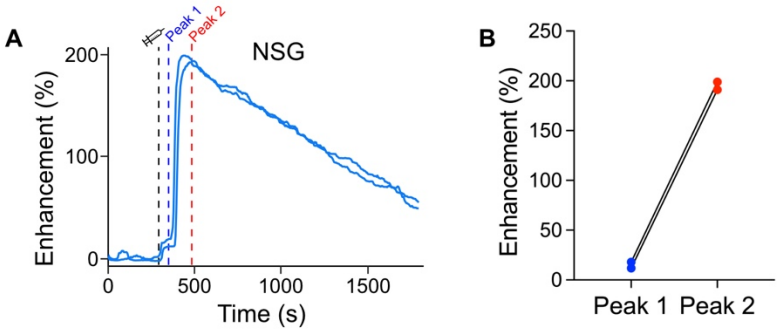

Figure 2-S1. The second wave of hemodynamic contrast is independent of antibodies. **A)** Time courses of Doppler signal enhancement following IV injection of 100 µL OD 50 Ana into NSG mice. N = 2. Dashed lines mark time of injection (black, 300 s), peak 1 (blue, 350 s), peak 2 (red, 480 s). **B)** Enhancement at the indicated timepoints in time courses from panel B.

	GV	RBC	Water
Radius, r (µm)	0.062	2.215	
Density, ρ (kg/m^3)	1.2	1110	1000, denoted as ρ_w
Compressibility, κ (m^2/N)	7.65e-6	3.48e-10	4.5e-10, denoted as κ_w
Wavenumber, k (m^{-1})			10000
Scattering cross section (σ_S, nm^2) of a single particle	1.53e-7	1.83e-7	

$$\sigma_S = \frac{4\pi k^4 r^6}{9}\left[\left|\frac{\kappa - \kappa_w}{\kappa_w}\right|^2 + 3\left|\frac{\rho - \rho_w}{2\rho + \rho_w}\right|^2\right]$$

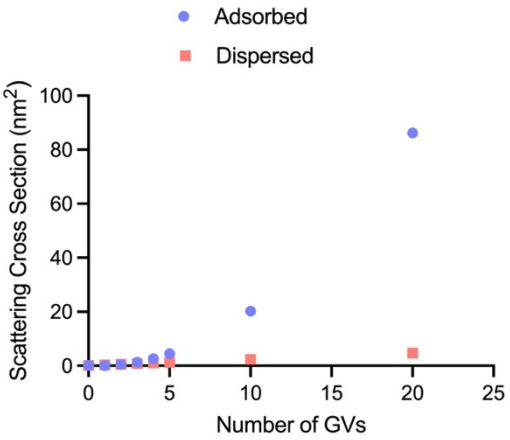

Figure 2-S2. Modeling of scattering cross section. **A)** Particles were modeled as uniform spheres using published volume[57], density[58], and compressibility[59,60] parameters. Density and compressibility of RBC-GV complexes were calculated as volume-weighted averages of the values for RBCs and GVs alone. The wavenumber was chosen based on a 15 MHz acoustic wave in a medium with a speed of sound of 1500 m/s. Scattering cross section was calculated using the equation shown[31]. **B)** Scattering cross section of a single RBC with the indicated number of GVs. The dispersed case was calculated by summing the cross sections of individual particles, while the adsorbed case was calculated based on a single particle with volume-weighted parameters.

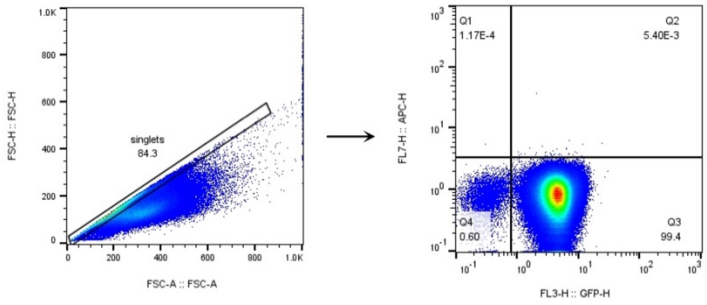

Figure 2-S3. Gating strategy for flow cytometry of RBCs. Single cells were gated based on FSC-H vs FSC-A. Quadrants were defined based on an RBC-only control sample.

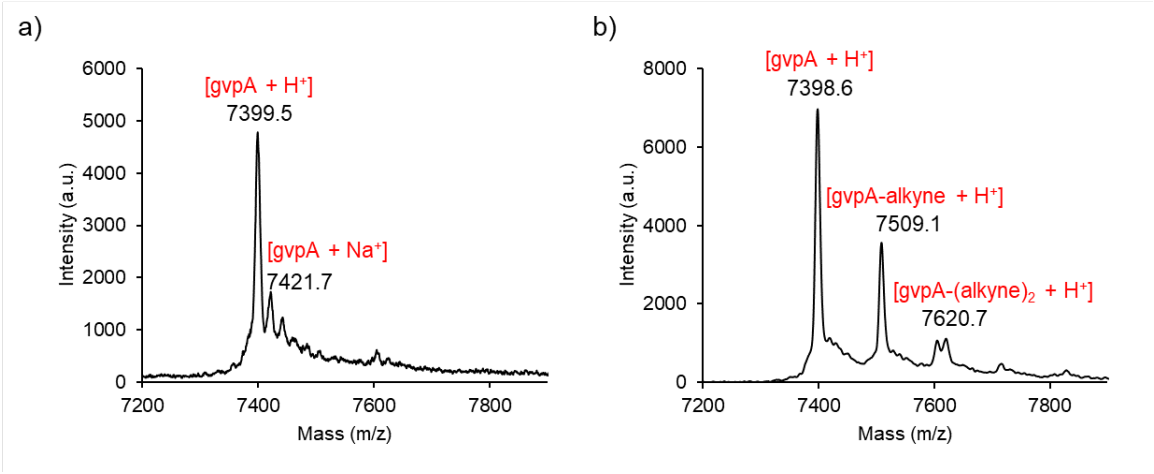

Figure 2-S4. MALDI mass spectrum of Ana (**A**) and Ana-alkyne (**B**).

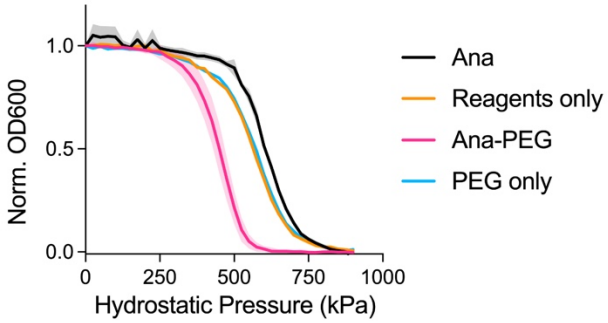

Figure 2-S5. Hydrostatic collapse pressure of GVs mixed with CuAAC reagents in the absence of mPEG-azide or mixed with mPEG-azide without CuAAC reagents. N = 3. Curves for Ana and Ana-PEG shown for comparison. Thick lines, mean; shaded area, ±SEM.

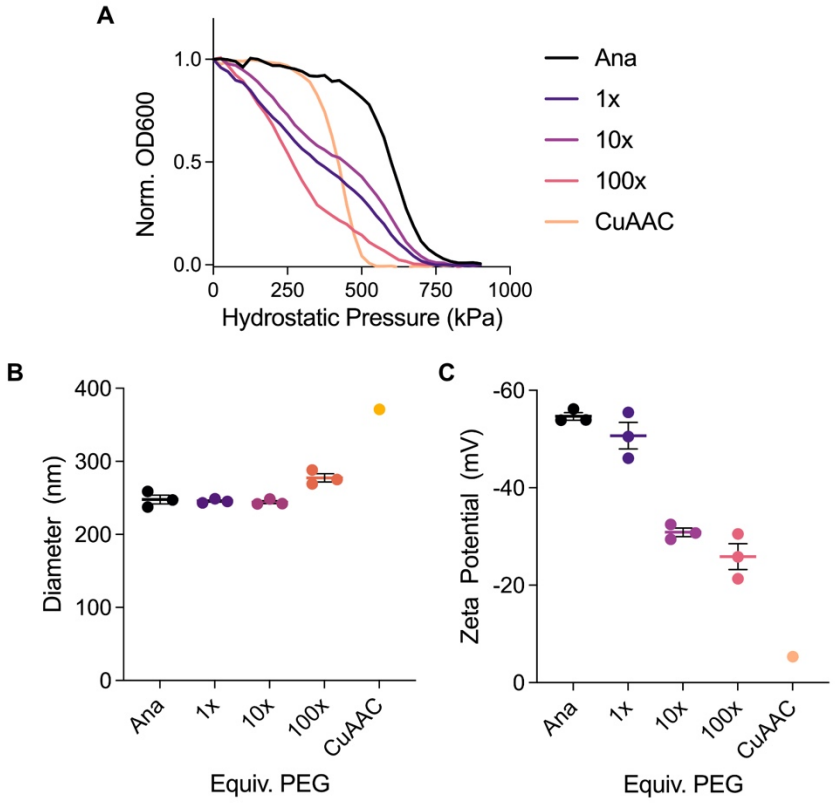

Figure 2-S6. Direct functionalization with NHS-PEG. **A)** Representative hydrostatic collapse pressure curves for GVs reacted with the indicated ratio of NHS-PEG, calculated relative to gvpA.

Curves for unmodified Ana and Ana-PEG prepared by CuAAC are shown for comparison. N = 3. **B)** Dynamic light scattering measurements, shown with Ana and Ana-PEG. N = 3. **C)** Zeta potential measurements, shown with Ana and Ana-PEG. N = 3.

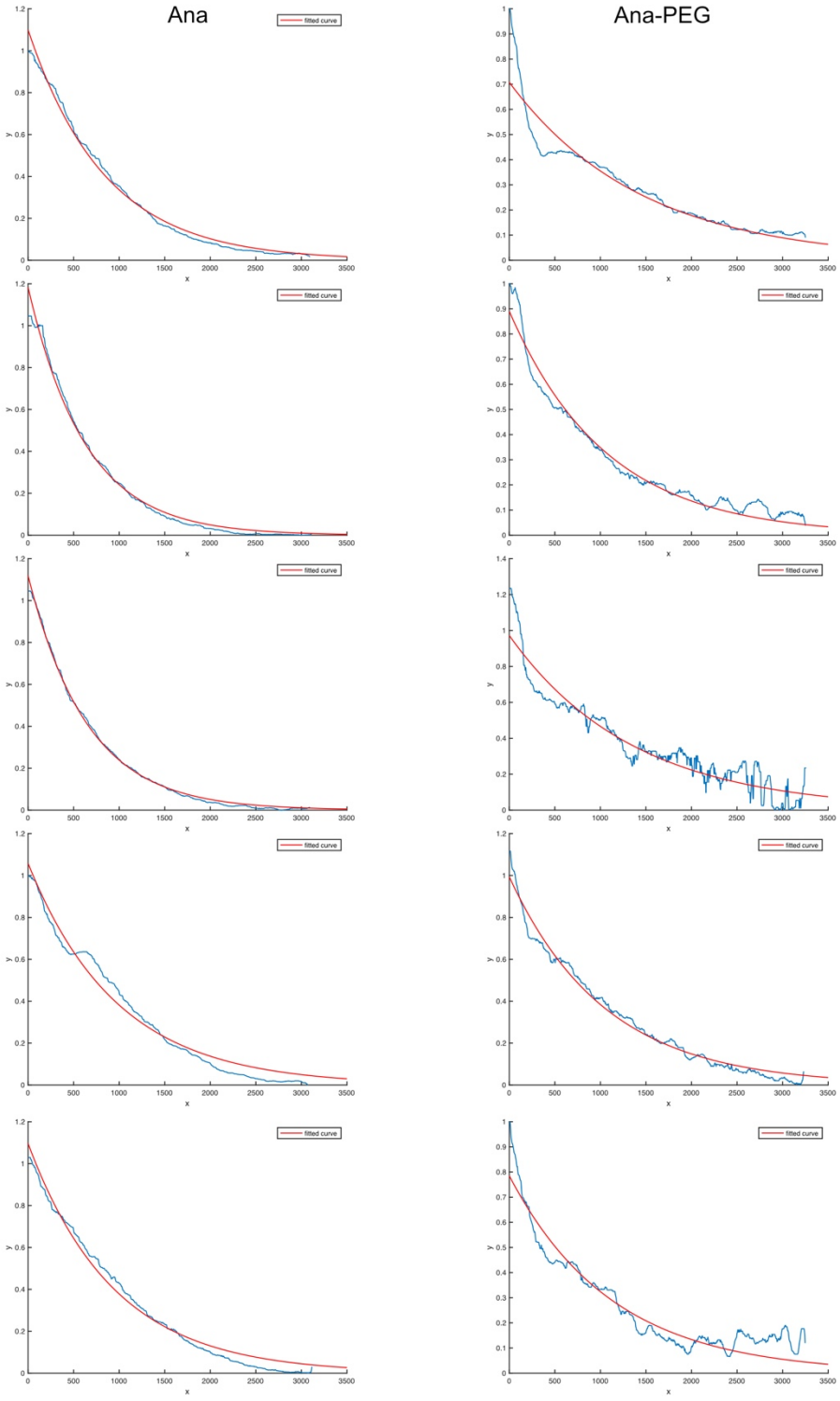
Ana
Ana-PEG
fitted curve
x
y

Figure 2-S7. Signal enhancement time courses from Ana and Ana-PEG fit to an exponential decay function.

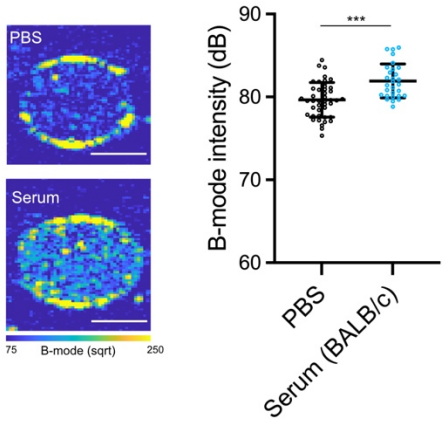

Figure 2-S8. Ultrasound imaging of Ana GVs exposed to serum from naïve BALB/c mice. Left: Representative B-mode images after incubation at 37 °C for 1 h in PBS or serum. Right: Mean B-mode intensity within each well. N = 24. Welch's t-test (***, $p < 0.001$).

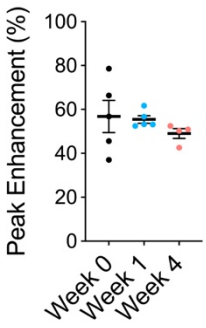

Figure 2-S9. Peak signal enhancement in time courses from Fig. 2-4e.

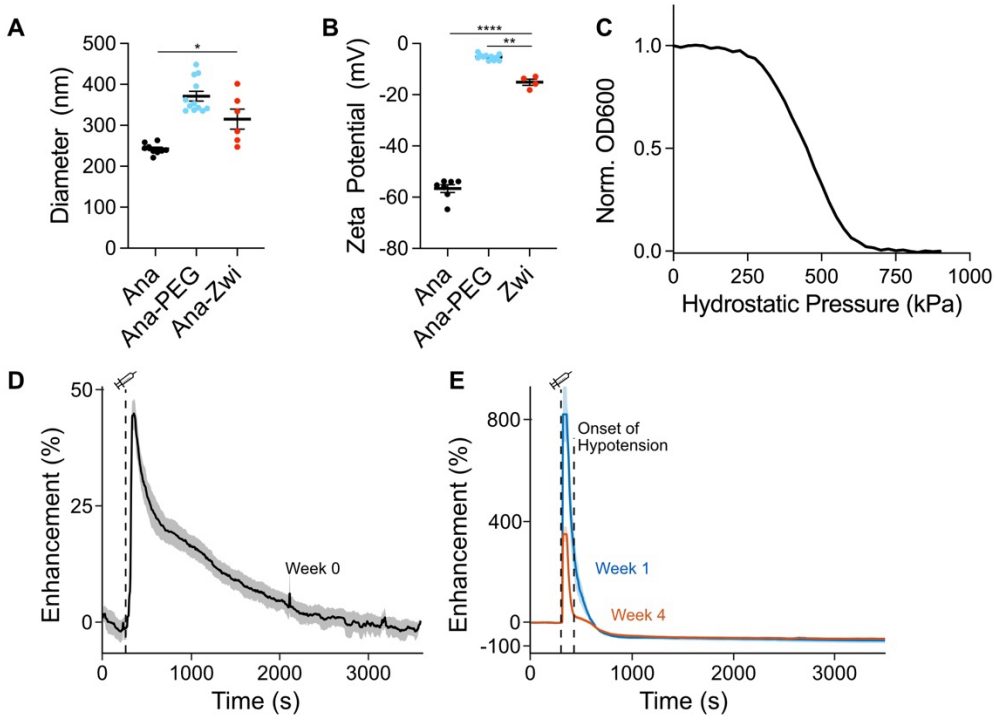

Figure 2-S10. Functionalization with zwitterionic polymer does not reduce immunogenicity. **A)** DLS measurements of GVs coated with polyzwitterion. N = 6. Welch's t-test, (*, $p<0.05$). **B)** Zeta potential measurements. N = 4. Welch's t-test, (**, $p<0.01$; ****, $p<0.0001$). **C)** Representative hydrostatic collapse pressure curve of Ana-Zwi. **D)** Mean hemodynamic signal enhancement time course following IV injection of 100 µL OD 50 Ana-Zwi at 300 s (dashed line). Shaded area represents ±SEM. N = 4. **E)** Mean hemodynamic signal enhancement following a second injection of Ana-Zwi after 1 (N = 2) or 4 weeks (N = 3). Dashed black line, time of injection (300 s); dashed red line, onset of hypotension (500 s); thick lines, mean; shaded area, ±SEM.

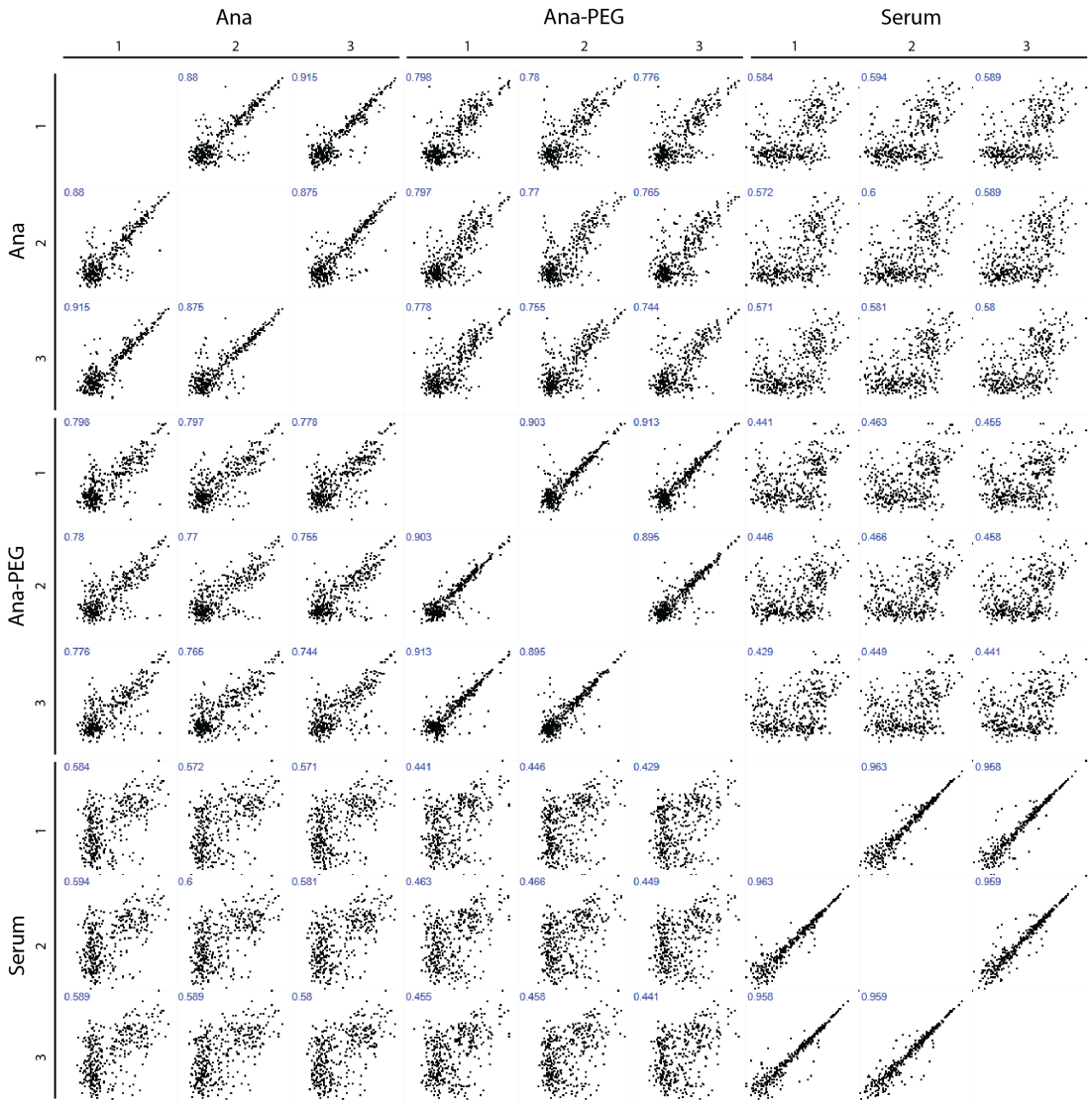

Figure 2-S11. Multi-scatter plot of protein abundances in each sample. Pearson correlation coefficient (R) is shown in the top left of each subplot.

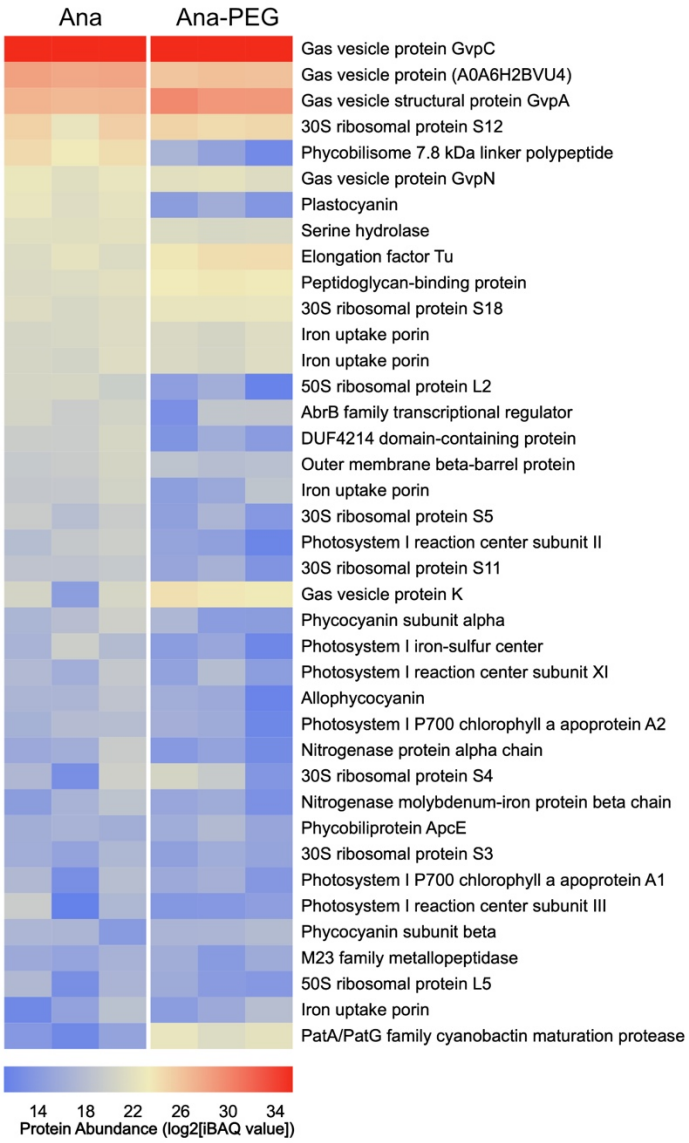

Figure 2-S12. Heat map of cyanobacterial proteins detected by LC-MS/MS.

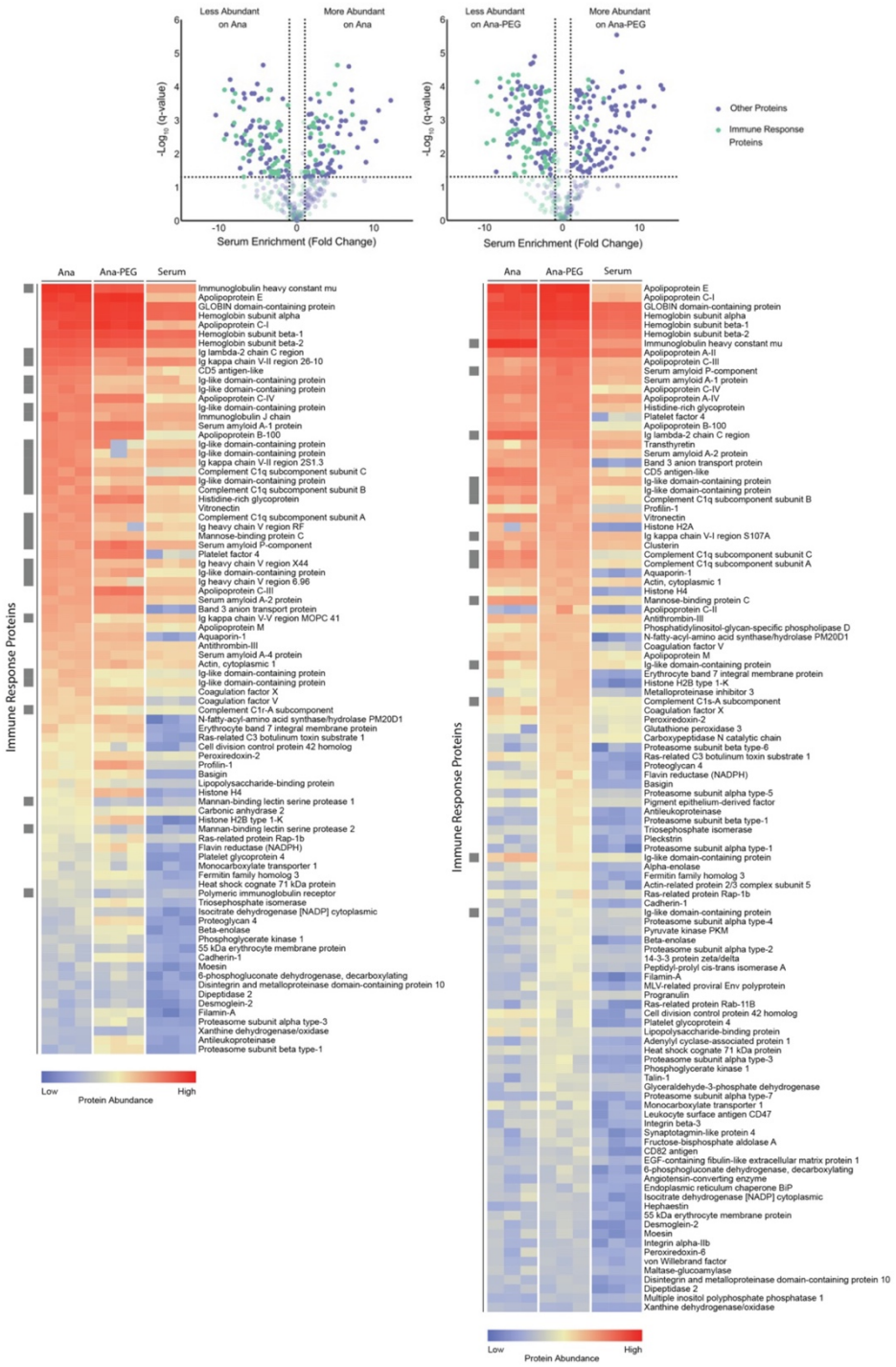
Less Abundant on Ana
More Abundant on Ana
Less Abundant on Ana-PEG
More Abundant on Ana-PEG
-Log10 (q-value)
Serum Enrichment (Fold Change)
Other Proteins
Immune Response Proteins
Ana
Ana-PEG
Serum
Immune Response Proteins
Immunoglobulin heavy constant mu
Apolipoprotein E
GLOBIN domain-containing protein
Hemoglobin subunit alpha
Apolipoprotein C-I
Hemoglobin subunit beta-1
Hemoglobin subunit beta-2
Ig lambda-2 chain C region
Ig kappa chain V-II region 26-10
CD5 antigen-like
Ig-like domain-containing protein
Ig-like domain-containing protein
Apolipoprotein C-IV
Ig-like domain-containing protein
Immunoglobulin J chain
Serum amyloid A-1 protein
Apolipoprotein B-100
Ig-like domain-containing protein
Ig-like domain-containing protein
Ig kappa chain V-II region 2S1.3
Complement C1q subcomponent subunit C
Ig-like domain-containing protein
Complement C1q subcomponent subunit B
Histidine-rich glycoprotein
Vitronectin
Complement C1q subcomponent subunit A
Ig heavy chain V region RF
Mannose-binding protein C
Serum amyloid P-component
Platelet factor 4
Ig heavy chain V region X44
Ig-like domain-containing protein
Ig heavy chain V region 6.96
Apolipoprotein C-III
Serum amyloid A-2 protein
Band 3 anion transport protein
Ig kappa chain V-V region MOPC 41
Apolipoprotein M
Aquaporin-1
Antithrombin-III
Serum amyloid A-4 protein
Actin, cytoplasmic 1
Ig-like domain-containing protein
Ig-like domain-containing protein
Coagulation factor X
Coagulation factor V
Complement C1r-A subcomponent
N-fatty-acyl-amino acid synthase/hydrolase PM20D1
Erythrocyte band 7 integral membrane protein
Ras-related C3 botulinum toxin substrate 1
Cell division control protein 42 homolog
Peroxiredoxin-2
Profilin-1
Basigin
Lipopolysaccharide-binding protein
Histone H4
Mannan-binding lectin serine protease 1
Carbonic anhydrase 2
Histone H2B type 1-K
Mannan-binding lectin serine protease 2
Ras-related protein Rap-1b
Flavin reductase (NADPH)
Platelet glycoprotein 4
Monocarboxylate transporter 1
Fermitin family homolog 3
Heat shock cognate 71 kDa protein
Polymeric immunoglobulin receptor
Triosephosphate isomerase
Isocitrate dehydrogenase [NADP] cytoplasmic
Proteoglycan 4
Beta-enolase
Phosphoglycerate kinase 1
55 kDa erythrocyte membrane protein
Cadherin-1
Moesin
6-phosphogluconate dehydrogenase, decarboxylating
Disintegrin and metalloproteinase domain-containing protein 10
Dipeptidase 2
Desmoglein-2
Filamin-A
Proteasome subunit alpha type-3
Xanthine dehydrogenase/oxidase
Antileukoproteinase
Proteasome subunit beta type-1
Low
High
Protein Abundance
Apolipoprotein E
Apolipoprotein C-I
GLOBIN domain-containing protein
Hemoglobin subunit alpha
Hemoglobin subunit beta-1
Hemoglobin subunit beta-2
Immunoglobulin heavy constant mu
Apolipoprotein A-II
Apolipoprotein C-III
Serum amyloid P-component
Serum amyloid A-1 protein
Apolipoprotein C-IV
Apolipoprotein A-IV
Histidine-rich glycoprotein
Platelet factor 4
Apolipoprotein B-100
Ig lambda-2 chain C region
Transthyretin
Serum amyloid A-2 protein
Band 3 anion transport protein
CD5 antigen-like
Ig-like domain-containing protein
Ig-like domain-containing protein
Complement C1q subcomponent subunit B
Profilin-1
Vitronectin
Histone H2A
Ig kappa chain V-I region S107A
Clusterin
Complement C1q subcomponent subunit C
Complement C1q subcomponent subunit A
Aquaporin-1
Actin, cytoplasmic 1
Histone H4
Mannose-binding protein C
Apolipoprotein C-II
Antithrombin-III
Phosphatidylinositol-glycan-specific phospholipase D
N-fatty-acyl-amino acid synthase/hydrolase PM20D1
Coagulation factor V
Apolipoprotein M
Ig-like domain-containing protein
Erythrocyte band 7 integral membrane protein
Histone H2B type 1-K
Metalloproteinase inhibitor 3
Complement C1s-A subcomponent
Coagulation factor X
Peroxiredoxin-2
Glutathione peroxidase 3
Carboxypeptidase N catalytic chain
Proteasome subunit beta type-6
Ras-related C3 botulinum toxin substrate 1
Proteoglycan 4
Flavin reductase (NADPH)
Basigin
Proteasome subunit alpha type-5
Pigment epithelium-derived factor
Antileukoproteinase
Proteasome subunit beta type-1
Triosephosphate isomerase
Pleckstrin
Proteasome subunit alpha type-1
Ig-like domain-containing protein
Alpha-enolase
Fermitin family homolog 3
Actin-related protein 2/3 complex subunit 5
Ras-related protein Rap-1b
Cadherin-1
Ig-like domain-containing protein
Proteasome subunit alpha type-4
Pyruvate kinase PKM
Beta-enolase
Proteasome subunit alpha type-2
14-3-3 protein zeta/delta
Peptidyl-prolyl cis-trans isomerase A
Filamin-A
MLV-related proviral Env polyprotein
Progranulin
Ras-related protein Rab-11B
Cell division control protein 42 homolog
Platelet glycoprotein 4
Lipopolysaccharide-binding protein
Adenylyl cyclase-associated protein 1
Heat shock cognate 71 kDa protein
Proteasome subunit alpha type-3
Phosphoglycerate kinase 1
Talin-1
Glyceraldehyde-3-phosphate dehydrogenase
Proteasome subunit alpha type-7
Monocarboxylate transporter 1
Leukocyte surface antigen CD47
Integrin beta-3
Synaptotagmin-like protein 4
Fructose-bisphosphate aldolase A
CD82 antigen
EGF-containing fibulin-like extracellular matrix protein 1
6-phosphogluconate dehydrogenase, decarboxylating
Angiotensin-converting enzyme
Endoplasmic reticulum chaperone BiP
Isocitrate dehydrogenase [NADP] cytoplasmic
Hephaestin
55 kDa erythrocyte membrane protein
Desmoglein-2
Moesin
Integrin alpha-IIb
Peroxiredoxin-6
von Willebrand factor
Maltase-glucoamylase
Disintegrin and metalloproteinase domain-containing protein 10
Dipeptidase 2
Multiple inositol polyphosphate phosphatase 1
Xanthine dehydrogenase/oxidase
Low
High
Protein Abundance

Figure 2-S13. Protein abundances relative to serum. Top: Volcano plots of protein abundances on Ana (left) and Ana-PEG (right) compared to serum. Abundances were compared by multiple unpaired t-test analysis using the false discovery rate method of Benjamini and Hochberg. Proteins with a false discovery rate of 5% and $\log_2$ fold-change greater than 1 were deemed differentially abundant. Proteins that were not differentially abundant are shown translucently. Bottom: Heat map of differentially abundant proteins on Ana (left) and Ana-PEG (left) compared to serum. Immune response proteins are indicated by a gray box on the left.

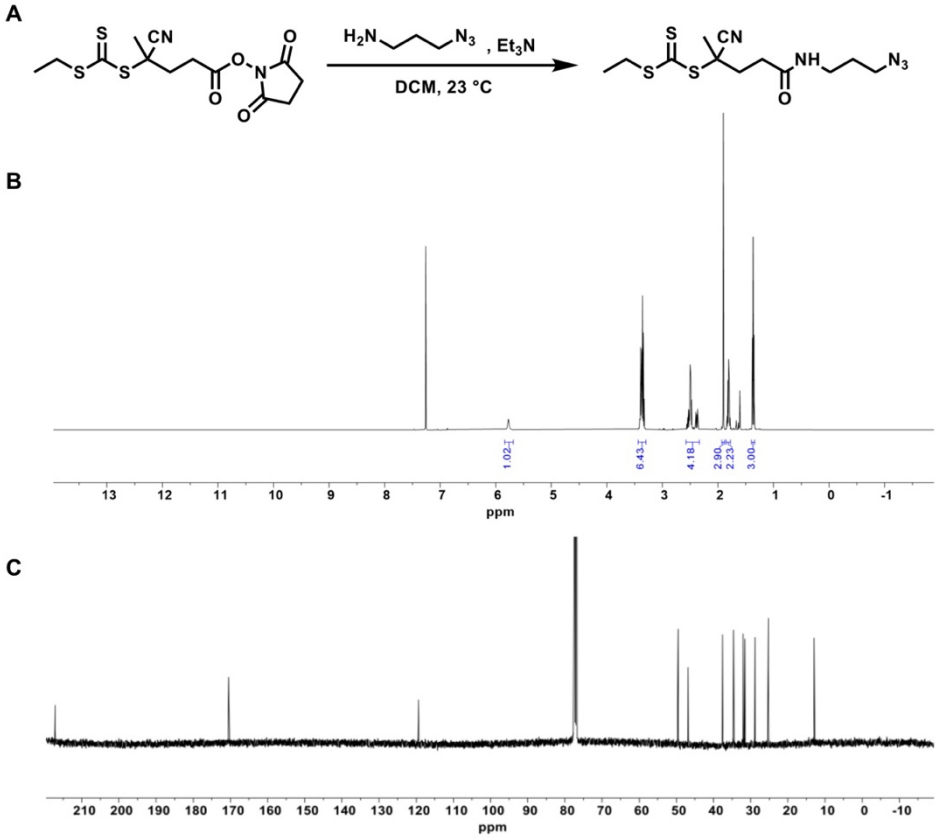

Figure 2-S14. Synthesis of CTA1. **A)** Reaction scheme. ^{1}H (**B**, 500 MHz) and ^{13}C (**C**, 101 MHz) NMR spectra of **CTA1** in $CDCl_3$. ^{1}H NMR (500 MHz in $CDCl_3$) δ: 5.77 (br s, 1H), 3.41–3.34 (m, 6H), 2.56–2.47 (m, 4H), 1.90 (s, 3H), 1.81 (p, J = 7.43 Hz, 2H), 1.37 (t, J = 6.60 Hz, 3H). ^{13}C NMR (101 MHz in $CDCl_3$) δ: 217.18, 170.51, 119.35, 49.53, 46.83, 37.58, 34.58, 32.01, 31.51, 28.85, 25.24, 12.90. MS $[C_{12}H_{19}N_5OS_3]^{+\bullet}$ calculated 345.07462, observed 345.07442. IR: 3292, 3084, 2929, 2871, 2093, 1645, 1548, 1447, 1375, 1260, 1152, 1116, 1073, 1031, 969, 942, 861, 801, 642 cm^{-1}.

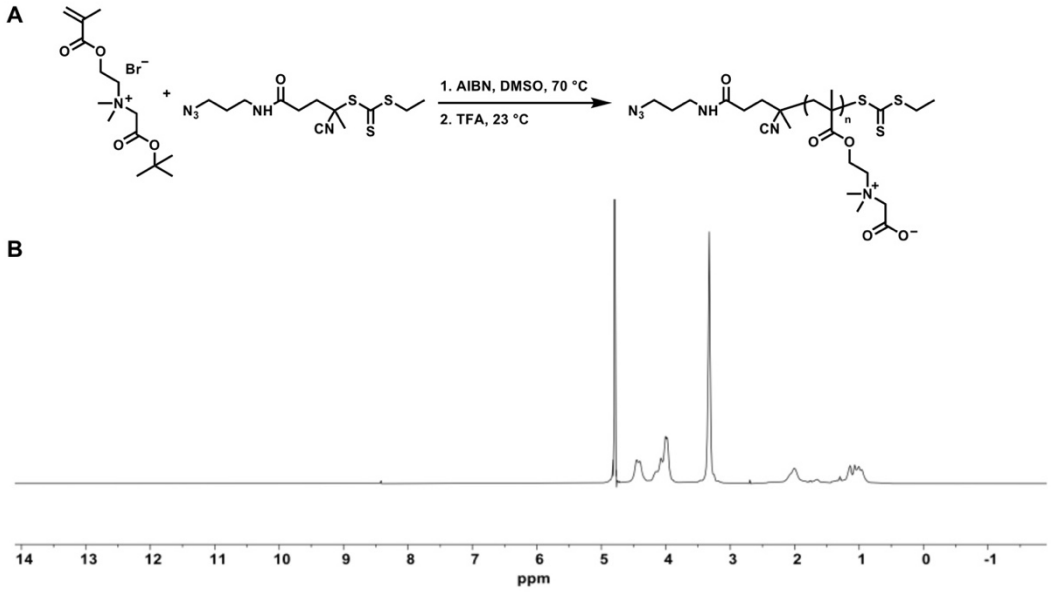

Figure 2-S15. Synthesis of zwitterionic polymer. **A)** Reaction scheme. **B)** ^{1}H NMR (500 MHz) spectrum of zwitterionic polymer in D_2O. ^{1}H NMR (500 MHz in D_2O) δ: 4.55–4.30, 4.23–3.88, 3.45–3.21, 2.45–2.37, 2.17–1.88, 1.73–1.57, 1.46–0.83. M_n = 16.3 kDa, $Đ$ = 1.25 (aqueous SEC). IR: 3382, 3027, 2966, 1722, 1623, 1472, 1452, 1421, 1386, 1335, 1263, 1234, 1147, 1058, 958, 936, 892, 845, 748, 712 cm^{-1}.

References

1. Chen, G., Roy, I., Yang, C. & Prasad, P. N. Nanochemistry and nanomedicine for nanoparticle-based diagnostics and therapy. *Chem. Rev.* **116**, 2826–2885 (2016).
2. Monopoli, M. P., Åberg, C., Salvati, A. & Dawson, K. A. Biomolecular coronas provide the biological identity of nanosized materials. *Nat. Nanotechnol.* **7**, 779–786 (2012).
3. Corbo, C. *et al.* The impact of nanoparticle protein corona on cytotoxicity, immunotoxicity and target drug delivery. *Nanomed.* **11**, 81–100 (2016).
4. Lazarovits, J., Chen, Y. Y., Sykes, E. A. & Chan, W. C. W. Nanoparticle–blood interactions: the implications on solid tumour targeting. *Chem. Commun.* **51**, 2756–2767 (2015).
5. Ngo, W. *et al.* Identifying cell receptors for the nanoparticle protein corona using genome screens. *Nat. Chem. Biol.* **18**, 1023–1031 (2022).
6. Lazarovits, J. *et al.* Supervised learning and mass spectrometry predicts the in vivo fate of nanomaterials. *ACS Nano* **13**, 8023–8034 (2019).
7. Walkey, C. D. *et al.* Protein corona fingerprinting predicts the cellular interaction of gold and silver nanoparticles. *ACS Nano* **8**, 2439–2455 (2014).
8. Jokerst, J. V., Lobovkina, T., Zare, R. N. & Gambhir, S. S. Nanoparticle PEGylation for imaging and therapy. *Nanomed.* **6**, 715–728 (2011).
9. Cooley, M. B. *et al.* Characterization of the interaction of nanobubble ultrasound contrast agents with human blood components. *Bioact. Mater.* **19**, 642–652 (2023).
10. Ferguson, L. T. *et al.* Dual affinity to RBCs and target cells (DART) enhances both organ- and cell type-targeting of intravascular nanocarriers. *ACS Nano* **16**, 4666–4683 (2022).
11. Anderson, H. L., Brodsky, I. E. & Mangalmurti, N. S. The evolving erythrocyte: Red blood cells as modulators of innate immunity. *J. Immunol.* **201**, 1343–1351 (2018).
12. Maresca, D. *et al.* Biomolecular ultrasound and sonogenetics. *Annu. Rev. Chem. Biomol. Eng.* **9**, 229–252 (2018).
13. Walsby, A. E. Gas vesicles. *Microbiol. Rev.* **58**, 94–144 (1994).
14. Shapiro, M. G. *et al.* Biogenic gas nanostructures as ultrasonic molecular reporters. *Nat. Nanotechnol.* **9**, 311–316 (2014).
15. Maresca, D. *et al.* Acoustic biomolecules enhance hemodynamic functional ultrasound imaging of neural activity. *NeuroImage* **209**, 116467 (2020).
16. Rabut, C. *et al.* Ultrafast amplitude modulation for molecular and hemodynamic ultrasound imaging. *Appl. Phys. Lett.* **118**, 244102 (2021).
17. Hurt, R. C. *et al.* Genomically mined acoustic reporter genes for real-time in vivo monitoring of tumors and tumor-homing bacteria. *Nat. Biotechnol.* 1–13 (2023).
18. Sawyer, D. P. *et al.* Ultrasensitive ultrasound imaging of gene expression with signal unmixing. *Nat. Methods* **18**, 945–952 (2021).
19. Hao, Y., Li, Z., Luo, J., Li, L. & Yan, F. Ultrasound molecular imaging of epithelial mesenchymal transition for evaluating tumor metastatic potential via targeted biosynthetic gas vesicles. *Small* **19**, 2207940 (2023).

20. Wang, G. *et al.* Surface-modified GVs as nanosized contrast agents for molecular ultrasound imaging of tumor. *Biomaterials* **236**, 119803 (2020).
21. Lakshmanan, A. *et al.* Molecular engineering of acoustic protein nanostructures. *ACS Nano* **10**, 7314–7322 (2016).
22. Lakshmanan, A. *et al.* Acoustic biosensors for ultrasound imaging of enzyme activity. *Nat. Chem. Biol.* **16**, 988–996 (2020).
23. Ling, B. *et al.* Biomolecular ultrasound imaging of phagolysosomal function. *ACS Nano* **14**, 12210–12221 (2020).
24. Bar-Zion, A. *et al.* Acoustically triggered mechanotherapy using genetically encoded gas vesicles. *Nat. Nanotechnol.* **16**, 1403–1412 (2021).
25. Lu, G. J. *et al.* Genetically encodable contrast agents for optical coherence tomography. *ACS Nano* **14**, 7823–7831 (2020).
26. Farhadi, A. *et al.* Genetically encoded phase contrast agents for digital holographic microscopy. *Nano Lett.* **20**, 8127–8134 (2020).
27. Lu, G. J. *et al.* Acoustically modulated magnetic resonance imaging of gas-filled protein nanostructures. *Nat. Mater.* **17**, 456–463 (2018).
28. Shapiro, M. G. *et al.* Genetically encoded reporters for hyperpolarized xenon magnetic resonance imaging. *Nat. Chem.* **6**, 629–634 (2014).
29. Lakshmanan, A. *et al.* Preparation of biogenic gas vesicle nanostructures for use as contrast agents for ultrasound and MRI. *Nat. Protoc.* **12**, 2050–2080 (2017).
30. Fisher, N. G. *et al.* Myocardial and microcirculatory kinetics of BR14, a novel third-generation intravenous ultrasound contrast agent. *J. Am. Coll. Cardiol.* **39**, 530–537 (2002).
31. Cobbold, R. S. C. *Foundations of Biomedical Ultrasound*. (Oxford University Press, 2007).
32. Maresca, D. *et al.* Nonlinear ultrasound imaging of nanoscale acoustic biomolecules. *Appl. Phys. Lett.* **110**, 073704 (2017).
33. Yao, Y., Jin, Z., Ling, B., Malounda, D. & Shapiro, M. G. Self-assembly of protein superstructures by physical interactions under cytoplasm-like conditions. *Biophys. J.* **120**, 2701–2709 (2021).
34. Baumgarth, N., Tung, J. W. & Herzenberg, L. A. Inherent specificities in natural antibodies: a key to immune defense against pathogen invasion. *Springer Semin. Immunopathol.* **26**, 347–362 (2005).
35. Kozma, G. T. *et al.* Pseudo-anaphylaxis to polyethylene glycol (PEG)-coated liposomes: Roles of anti-PEG IgM and complement activation in a porcine model of human infusion reactions. *ACS Nano* **13**, 9315–9324 (2019).
36. Ibrahim, M. *et al.* Polyethylene glycol (PEG): The nature, immunogenicity, and role in the hypersensitivity of PEGylated products. *J. Controlled Release* **351**, 215–230 (2022).
37. Liu, S. & Jiang, S. Zwitterionic polymer-protein conjugates reduce polymer-specific antibody response. *Nano Today* **11**, 285–291 (2016).
38. Cabanach, P. *et al.* Zwitterionic 3D-printed non-immunogenic stealth microrobots. *Adv. Mater.* **32**, 2003013 (2020).

39. Tuttle, A. H., Philip, V. M., Chesler, E. J. & Mogil, J. S. Comparing phenotypic variation between inbred and outbred mice. *Nat. Methods* **15**, 994–996 (2018).
40. Jones, K., Savulescu, A. F., Brombacher, F. & Hadebe, S. Immunoglobulin M in health and diseases: How far have we come and what next? *Front. Immunol.* **11**, (2020).
41. Stordy, B. *et al.* Conjugating ligands to an equilibrated nanoparticle protein corona enables cell targeting in serum. *Chem. Mater.* **34**, 6868–6882 (2022).
42. Zhang, Z. *et al.* Brain-targeted drug delivery by manipulating protein corona functions. *Nat. Commun.* **10**, 3561 (2019).
43. Oh, J. Y. *et al.* Cloaking nanoparticles with protein corona shield for targeted drug delivery. *Nat. Commun.* **9**, 4548 (2018).
44. Kim, S., Zhang, S. & Yoon, S. Multiplexed ultrasound imaging using spectral analysis on gas vesicles. *Adv. Healthc. Mater.* **11**, 2200568 (2022).
45. Blume, J. E. *et al.* Rapid, deep and precise profiling of the plasma proteome with multi-nanoparticle protein corona. *Nat. Commun.* **11**, 3662 (2020).
46. Caron, E. *et al.* Analysis of major histocompatibility complex (MHC) immunopeptidomes using Mass spectrometry. *Mol. Cell. Proteomics* **14**, 3105–3117 (2015).
47. Kontos, S., Kourtis, I. C., Dane, K. Y. & Hubbell, J. A. Engineering antigens for in situ erythrocyte binding induces T-cell deletion. *Proc. Natl. Acad. Sci.* **110**, E60–E68 (2013).
48. Pishesha, N. *et al.* Engineered erythrocytes covalently linked to antigenic peptides can protect against autoimmune disease. *Proc. Natl. Acad. Sci.* **114**, 3157–3162 (2017).
49. Shi, J. *et al.* Engineered red blood cells as carriers for systemic delivery of a wide array of functional probes. *Proc. Natl. Acad. Sci.* **111**, 10131–10136 (2014).
50. Kontos, S. & Hubbell, J. A. Improving protein pharmacokinetics by engineering erythrocyte affinity. *Mol. Pharm.* **7**, 2141–2147 (2010).
51. Hong, V., Presolski, S. I., Ma, C. & Finn, M. G. Analysis and optimization of copper-catalyzed azide–alkyne cycloaddition for bioconjugation. *Angew. Chem. Int. Ed.* **48**, 9879–9883 (2009).
52. Besanceney-Webler, C. *et al.* Increasing the efficacy of bioorthogonal click reactions for bioconjugation: A comparative study. *Angew. Chem. Int. Ed.* **50**, 8051–8056 (2011).
53. Schindelin, J. *et al.* Fiji: An open-source platform for biological-image analysis. *Nat. Methods* **9**, 676–682 (2012).
54. Benoit, D. S. W., Srinivasan, S., Shubin, A. D. & Stayton, P. S. Synthesis of folate-functionalized RAFT polymers for targeted siRNA delivery. *Biomacromolecules* **12**, 2708–2714 (2011).
55. Schatz, C., Louguet, S., Le Meins, J.-F. & Lecommandoux, S. Polysaccharide-block-polypeptide copolymer vesicles: Towards synthetic viral capsids. *Angew. Chem. Int. Ed.* **48**, 2572–2575 (2009).
56. Cao, Z., Yu, Q., Xue, H., Cheng, G. & Jiang, S. Nanoparticles for drug delivery prepared from amphiphilic PLGA zwitterionic block copolymers with sharp contrast in polarity between two blocks. *Angew. Chem. Int. Ed.* **49**, 3771–3776 (2010).

57. de Jong, K. *et al.* Short survival of phosphatidylserine-exposing red blood cells in murine sickle cell anemia. *Blood* **98**, 1577–1584 (2001).
58. Norouzi, N., Bhakta, H. C. & Grover, W. H. Sorting cells by their density. *PLoS ONE* **12**, e0180520 (2017).
59. Shung, K. K., Krisko, B. A. & Ballard, J. O., III. Acoustic measurement of erythrocyte compressibility. *J. Acoust. Soc. Am.* **72**, 1364–1367 (1982).
60. Fine, R. A. & Millero, F. J. Compressibility of water as a function of temperature and pressure. *J. Chem. Phys.* **59**, 5529–5536 (1973).

Chapter 3

BIOMOLECULAR ULTRASOUND IMAGING OF PHAGOLYSOSOMAL FUNCTION

Ling, B., Lee, J., Maresca, D., Lee-Gosselin, A., Malounda, D., Swift, M. B., & Shapiro, M. G. Biomolecular ultrasound imaging of phagolysosomal function. *ACS Nano* **14**, 12210-12221 (2020). https://doi.org/10.1021/acsnano.0c05912

3.1 Abstract

Phagocytic clearance and lysosomal processing of pathogens and debris are essential functions of the innate immune system. However, the assessment of these functions in vivo is challenging because most nanoscale contrast agents compatible with non-invasive imaging techniques are made from non-biodegradable synthetic materials that do not undergo regular lysosomal degradation. To overcome this challenge, we describe the use of an all-protein contrast agent to directly visualize and quantify phagocytic and lysosomal activities in vivo by ultrasound imaging. This contrast agent is based on gas vesicles (GVs), a class of air-filled protein nanostructures naturally expressed by buoyant microbes. Using a combination of ultrasound imaging, pharmacology, immunohistology and live-cell optical microscopy, we show that after intravenous injection, GVs are cleared from circulation by liver-resident macrophages. Once internalized, the GVs undergo lysosomal degradation, resulting in the

elimination of their ultrasound contrast. By non-invasively monitoring the temporal dynamics of GV-generated ultrasound signal in circulation and in the liver and fitting them with a pharmacokinetic model, we can quantify the rates of phagocytosis and lysosomal degradation in living animals. We demonstrate the utility of this method by showing how these rates are perturbed in two models of liver dysfunction: phagocyte deficiency and non-alcoholic fatty liver disease. The combination of proteolytically-degradable nanoscale contrast agents and quantitative ultrasound imaging thus enables non-invasive functional imaging of cellular degradative processes.

3.2 Introduction

The reticuloendothelial system (RES), also known as the mononuclear phagocyte system, is a network of phagocytic immune cells that is essential for organismal development and homeostasis; malfunctions in this system may lead to increased susceptibility to infections[1,2] and are associated with the pathogenesis of a variety of conditions, including neurodegeneration,[3,4] chronic liver disease[5] and many others.[6] Cells of the RES, such as monocytes, macrophages and dendritic cells, continuously sample their surroundings, mediating the recognition and clearance of abnormal and senescent cells, debris and foreign particulates.[7,8] Additionally, they interface with the adaptive immune system by presenting lysosomally-processed antigens to lymphocytes and secreting cytokines to stimulate the proper inflammatory response.[8-10] Phagocytosis and lysosomal degradation are thus vital processes of RES-mediated immunoregulation.

Non-invasive functional imaging of phagocytosis and lysosomal activities will enable early detection and monitoring of non-alcoholic fatty liver disease (NAFLD) and other conditions resulting from RES dysfunction. NAFLD currently affects over 25% of the global population and its progression is associated with chronic hepatic inflammation.[11] Due to the large patient population and broad range of outcomes which include hepatitis, cirrhosis, fibrosis and hepatocellular carcinoma, rapid and non-invasive diagnostic methods are needed to stratify patients into defined risk groups.[5,11] Ultrasound is well suited for this task due to its wide availability, portability, low operational costs and high tissue penetrance.[12] Based on *in vitro* observations that pro-inflammatory macrophages suppress phagocytosis[13] and lysosomal degradation,[14,15] one would expect livers in patients with NAFLD to exhibit reduced accumulation and extended persistence of intravenously-administered nanoscale contrast agents. Indeed, clinical studies have confirmed the former.[16,17] However, the latter cannot be evaluated with currently available technologies because agents compatible with non-invasive imaging modalities are typically made from synthetic materials which do not undergo regular lysosomal degradation.[7,8]

Here, we describe the use of an all-protein nanoscale contrast agent to visualize and quantify both phagocytic clearance and lysosomal degradation *in vivo* using ultrasound imaging. This contrast agent is based on gas vesicles (GVs), a class of air-filled protein nanostructures natively formed inside certain photosynthetic microorganisms as a means to regulate buoyancy.[18] GVs comprise a rigid, 2 nm-thick protein shell allowing the free exchange of gas but preventing the internal condensation of liquid water, thereby forming a thermodynamically stable capsule of air with a hydrodynamic diameter of approximately 250

nm.[19] They are easily isolated from cultures of their native cyanobacterial hosts[20] and can be expressed heterologously in bacteria[21,22] and mammalian cells.[23] Because sound waves are strongly reflected by air-water interfaces, GVs have been developed as contrast agents for ultrasound imaging.[19, 24-27] Due to their innate stability, GVs are able to withstand repeated insonation without loss of contrast.[19] However, when the GV shell is compromised by mechanical or chemical disruption, the gaseous contents it encloses rapidly and irreversibly dissolve into the surrounding media, leading to the elimination of ultrasound contrast.[19,21,27]

Based on their nanoscale dimensions and all-protein composition, which distinguishes them from other classes of ultrasound contrast agents[28-31], we hypothesized that we could use GVs as a contrast agent to non-invasively visualize the phagocytic and lysosomal functions of hepatic macrophages *in vivo*. Previous studies have shown that intravenously injected GVs are rapidly taken up by the liver.[32,33] If this uptake is mediated by macrophages and the internalized GVs undergo lysosomal proteolysis, this would manifest in the initial transfer of ultrasound contrast from the bloodstream to the liver, followed by its elimination with kinetics representative of natural RES clearance and degradation. Measurement of these processes would thus provide a quantitative picture of the complete phagocytic and lysosomal degradation pathways. This rate-based approach would improve upon previous Kupffer cell imaging techniques[16,34-36] which are limited to the assessment of phagocytosis. In this study, we test this hypothesis by visualizing the temporal dynamics of GV ultrasound contrast in the blood and liver, establishing the cellular and molecular pathways mediating GV uptake and degradation, and developing a

pharmacokinetic model to parametrize RES activity from hemodynamic and liver ultrasound signals. Finally, we demonstrate the diagnostic utility of functional imaging of macrophage phagolysosomal activity in two models of liver disease: clodronate-mediated macrophage deficiency and diet-induced NAFLD.

3.3 Results & Discussion

3.3.1 Gas vesicle blood clearance, liver uptake and degradation can be monitored by ultrasound

We started by quantifying the kinetics of GV uptake and degradation in healthy C57BL/6 mice (**Fig. 3-1a**). We first visualized intravascular GVs with ultrafast power Doppler imaging, leveraging the ability of intravenously (IV) injected GVs to enhance blood flow contrast.[25] We chose the brain as our target organ due to its practical advantages in mouse experiments: hemodynamic signals can be conveniently measured through intact skin and skull[25,37] and head-fixation reduces motion artifacts. We acquired images of a single coronal plane at a center frequency of 15 MHz and frame rate of 0.25 Hz (**Fig. 3-1b**). Following a 300-s baseline, we IV injected 100 μL of purified GVs isolated from *Anabaena flos-aquae* (OD_{500}30, corresponding to 2.1 x 10^{11} particles[20]) and tracked the ensuing distribution and clearance (**Fig. 3-1c**). As expected, the introduction of GVs caused a marked increase in hemodynamic signal, peaking at approximately 100 s after injection, and returning to baseline with an apparent circulation half-life of 232 s (**Fig. 3-1c, Fig. 3-S1**).

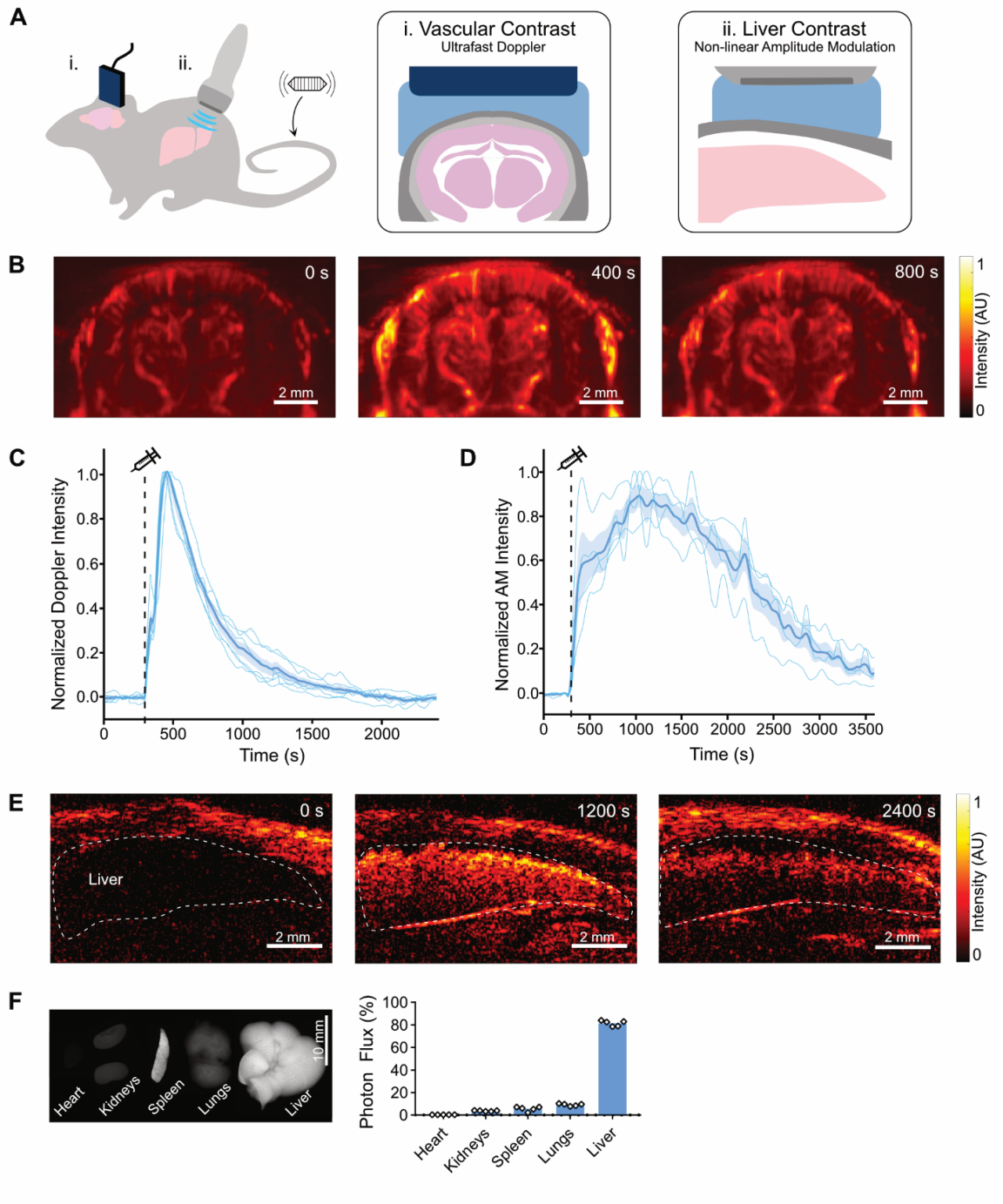

Figure 3-1: Non-invasive ultrasound imaging of GV clearance and elimination in vivo. **A)** Diagram of imaging setups used to measure GV contrast in the blood and liver. Inset i, intravascular persistence of purified GVs was visualized by ultrafast power Doppler imaging of the brain. Inset

ii, hepatic persistence of GVs modified to produce non-linear contrast was visualized by amplitude modulation imaging of the liver. **B)** Representative power Doppler images of a coronal cross section of the brain following GV injection. Scale bars, 2 mm. **C-D)** Normalized time courses of ultrafast Doppler signal enhancement in the brain (**C**, N = 6) and AM signal in the liver (**D**, N = 4). Dashed lines, time of GV injection (300 s); thin lines, individual trials; thick lines, mean; shaded areas, ± SEM. **E)** Representative AM images of a liver cross section following GV injection. Scale bars, 2 mm. **F)** Biodistribution of fluorescently-labeled GVs 1 h after IV injection. Representative fluorescence image of excised organs (left; scale bar, 10 mm). Percentage of total collected photons originating from each organ (right). N = 5. Error bars not shown.

Next, we quantified GV uptake and degradation in the liver by imaging this organ during and after IV injection (**Fig. 3-1a**). To maximize GV specificity, we injected GVs modified to produce non-linear ultrasound contrast[27] and imaged with a non-linear amplitude modulation (AM) pulse sequence[24] (**Fig. 3-1, d-e**). Following injection of 100 μL GVs at OD_{500} 30, we observed the accumulation of non-linear contrast in the liver—reaching a maximum after approximately 10 min—followed by a gradual loss of signal until only 10% remained at the end of one hour (**Fig. 3-1d**). Notably, the maximum occurs just as contrast in the blood returns to baseline (**Fig. 3-S2**). The apparent half-life of GVs in the liver—20 min—is substantially longer than their circulation time, and on a timescale consistent with lysosomal processing.[38-40] To independently confirm liver uptake, we acquired fluorescence images of mouse organs excised 1h after IV injection of GVs labeled with a far-red fluorescent dye (**Fig. 3-1f**). In line with previous investigations of GV biodistribution,[32,33] the liver was the dominant organ for GV uptake, emitting 81.4% of collected photons. The lungs (7.8%) and spleen (5.5%) had minor roles in GV clearance, while the heart and kidneys had no discernible role.

3.3.2 GVs are primarily cleared by liver macrophages

To identify the cells involved in GV clearance, we performed immunofluorescence imaging of liver sections obtained from mice perfused 1h after IV injection of fluorescently-labeled GVs (**Fig. 3-2a**). Based on the apparent active degradation of GVs, as suggested by the gradual decline of liver ultrasound contrast, we hypothesized that GVs would be taken up by Kupffer cells—resident macrophages lining the hepatic sinusoids which are implicated in the clearance of many nanoparticles.[7] We tested this hypothesis by defining antibody-stained F4/80$^+$ Kupffer cell regions through image segmentation by Ilastik[41] and quantifying the localization of GVs with respect to these borders (**Fig. 3-S3**). On average, 60% of GV-containing pixels resided within Kupffer cells (**Fig. 3-2b**).

To confirm the role of Kupffer cells in GV clearance, we ablated phagocytic cells by IV administration of 30 mg/kg liposome-encapsulated clodronate[42] (**Fig. 3-2c**). 48h later, we measured GV circulation times with hemodynamic ultrasound (**Fig. 3-2d**). Compared to mice treated with saline-filled control liposomes, clodronate-treated mice had a nearly 7-fold enhancement in GV circulation time, with half-life increasing from 274 s to 1670 s (**Fig. 3-S2**). Our results are in line with previous observations that treatment with 50 mg/kg clodronate increased the circulation half-life of 100 nm gold nanoparticles 13-fold.[1] Taken together, our data shows that GVs are mainly filtered from the blood by Kupffer cells.

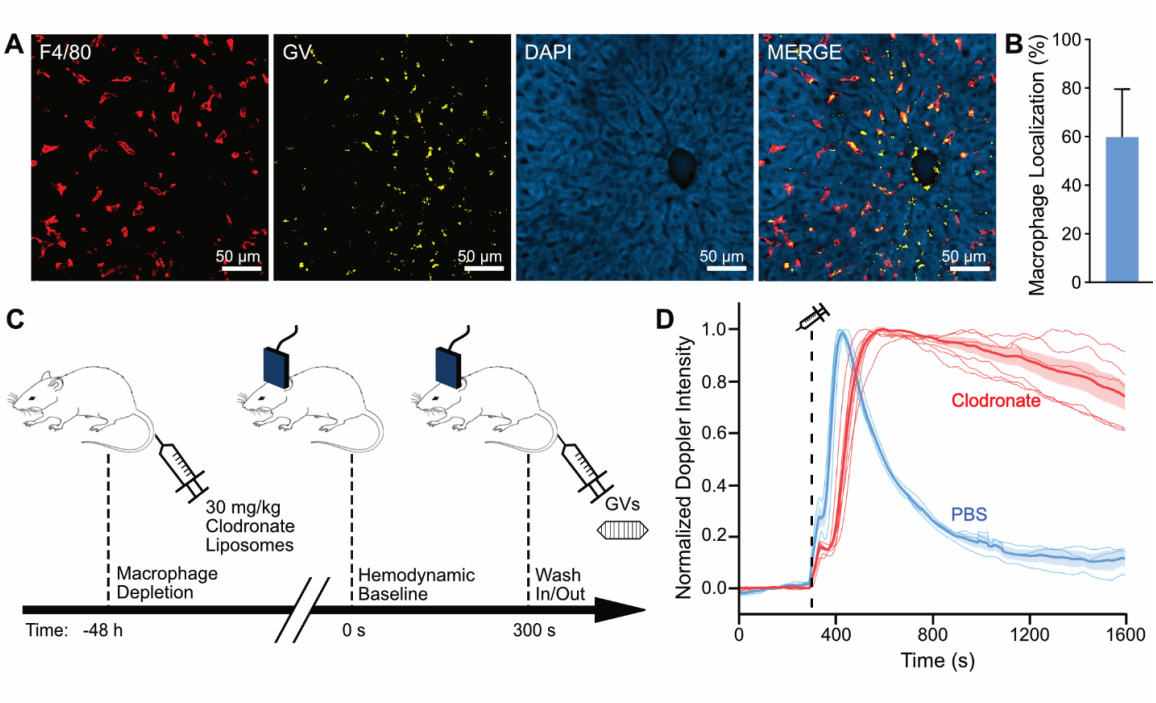

Figure 3-2: Liver macrophages are the primary mediators of GV clearance. **A)** Immunofluorescent confocal micrographs of 75-µm sections of liver tissue obtained from healthy mice 1h after IV injection of fluorescently-labeled GVs. Sections were stained with anti-F4/80 (macrophages) and DAPI. Scale bars, 50 µm. **B)** Percentage of detected GVs found within macrophage regions based on segmentation with ilastik. Error bars indicate ± SD. N = 3 biological replicates, 78 total fields of view. **C)** Experimental timeline. Macrophages were depleted by IV injection of 30 mg/kg liposomal clodronate 48 h before GV injection. **D)** Normalized Doppler signal enhancement time courses following IV injection of GVs in mice pre-treated with clodronate (red, N = 6) or saline liposomes (blue, N = 3). Dashed line, time of GV injection (300 s); thin lines, individual trials; thick lines, mean; shaded areas, ± SEM.

3.3.3 GVs are degraded in the lysosome following phagocytosis

Having established their uptake by liver macrophages, we next studied what happens to GVs following phagocytosis. Macrophages typically internalize nanoparticles into membrane-bound organelles—phagosomes—that are then trafficked along the phagolysosomal pathway. During this maturation process, the phagosomes acquire v-ATPase proton pumps to acidify their contents prior to fusion with the lysosome;[43] this low pH environment is

required for lysosomal enzyme activity. To visualize the movement of GVs along this pathway *in vitro*, we incubated murine macrophages (RAW264.7) with a dilute suspension of GVs dually-labeled with Alexa Fluor (AF647) and pHrodo Red—a pH-sensitive dye that fluoresces weakly at pH 7 and brightly at pH 3—and imaged them with live-cell confocal optical microscopy (**Fig. 3-3a**). Focusing on individual cells, we initially observed punctate spots of AF647 signal, likely corresponding to GVs concentrated within phagosomes, which matured over the next several minutes to produce strong pHrodo signal, indicating acidification of their environment (**Fig. 3-3b**). Zooming out to observe population-level dynamics revealed that the proportion of GVs in acidified compartments, as parametrized by the ratio of pHrodo to AF647 signal, grew continuously during a 1-hour incubation (**Fig. 3-3, c-d**). This rise was abolished when v-ATPase was inhibited by pretreatment with 100 nM bafilomycin A1 (BafA1),[44] thereby confirming that GVs undergo phagolysosomal processing in macrophages.

Lysosomal proteolysis is expected to break down the GV shell, resulting in GV collapse, gas dissolution and the disappearance of ultrasound contrast. To confirm this effect in vitro, we exposed RAW264.7 cells to GVs for 30 min. At predetermined time intervals, we detached the cells from their solid substrate and loaded them into an agarose phantom for imaging with a non-linear cross-propagating amplitude modulation pulse sequence (xAM)[26] (**Fig. 3-3e**). In control cells pretreated with 0.01% v/v dimethyl sulfoxide (DMSO), the signal declined with a half-life of approximately 3 h (**Fig. 3-3, f-g**). Conversely, in cells pretreated with BafA1 to block the activity of the pH-dependent lysosomal enzymes, we observed signal that persisted for at least 5 h without decay. These results confirm that GVs are

digested within macrophage lysosomes in a process that can be monitored with non-linear ultrasound imaging. The reason that this process happens somewhat more slowly in vitro compared to the liver may be the accelerated rate of phagosome maturation in primary macrophages[45].

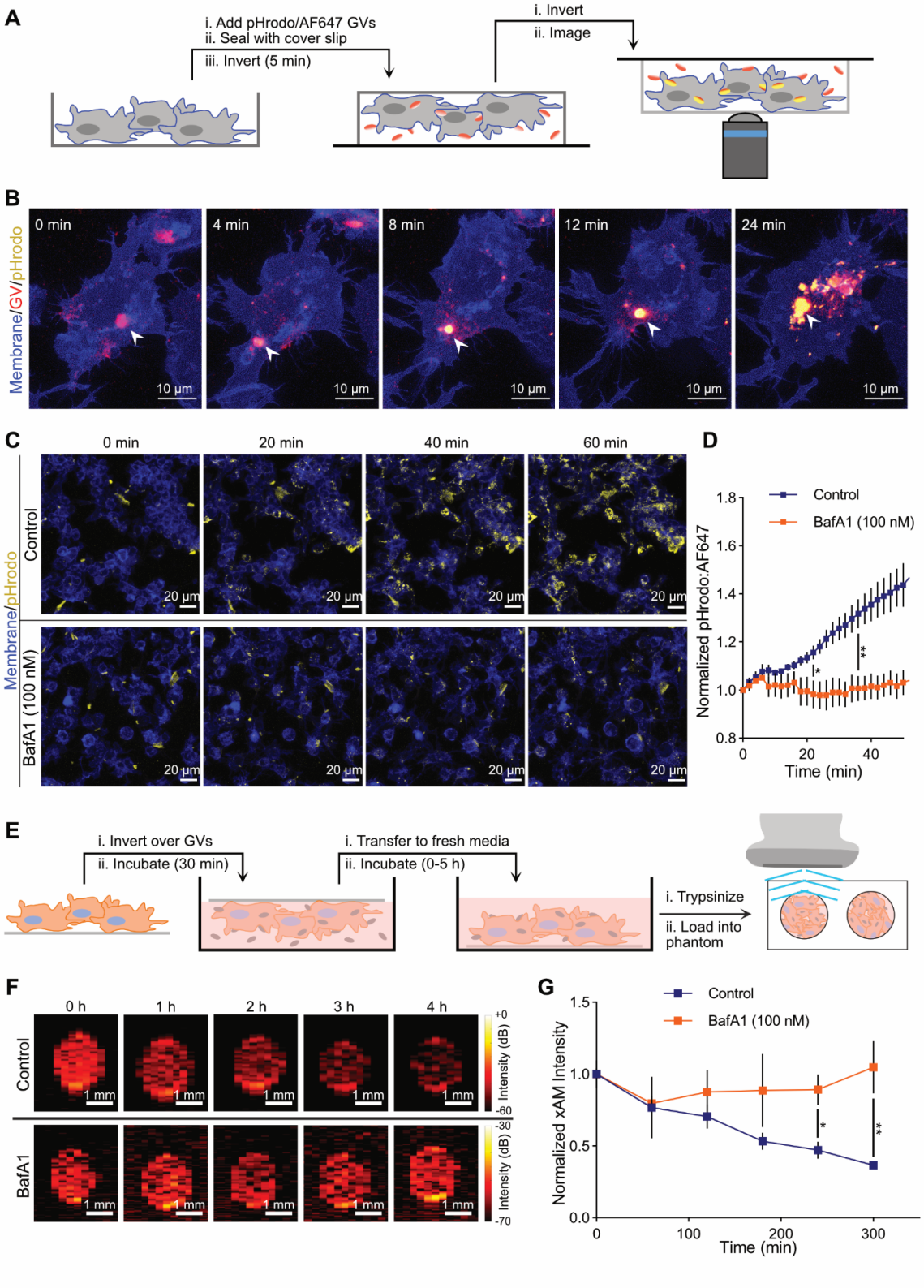
A
i. Add pHrodo/AF647 GVs
ii. Seal with cover slip
iii. Invert (5 min)
i. Invert
ii. Image
B
Membrane/GV/pHrodo
0 min
4 min
8 min
12 min
24 min
10 μm
C
0 min
20 min
40 min
60 min
Control
BafA1 (100 nM)
Membrane/pHrodo
20 μm
D
Control
BafA1 (100 nM)
Normalized pHrodo:AF647
Time (min)
E
i. Invert over GVs
ii. Incubate (30 min)
i. Transfer to fresh media
ii. Incubate (0-5 h)
i. Trypsinize
ii. Load into phantom
F
0 h
1 h
2 h
3 h
4 h
Control
BafA1
1 mm
Intensity (dB)
G
Control
BafA1 (100 nM)
Normalized xAM Intensity
Time (min)

Figure 3-3: Internalized GVs are degraded within lysosomes, resulting in loss of ultrasound contrast. **A)** Diagram of live cell confocal microscopy protocol. Murine macrophages (RAW264.7) expressing membrane-localized fluorescent protein (blue) were incubated with GVs dually-labeled with AF647 (red) and pHrodo (yellow) to track localization and pH, respectively. **B)** Representative images of a single cell at different time points following GV uptake. A phagosome maturation event is indicated by the white arrows. Scale bars, 10 μm (63x objective). **C)** Representative population-level images of cells pre-treated with DMSO (top) or 100 nM bafilomycin A1 (bottom) following GV uptake. The AF647 channel is not shown. Scale bars, 20 μm (20x objective). **D)** Ratio of pHrodo to AF647 signals in images from **c**, normalized to the initial timepoint. Error bars represent ± SEM. N = 4. Welch's t test (*: $p<0.05$; **: $p<0.001$). **E)** Diagram of uptake protocol for ultrasound imaging. RAW264.7 cells were incubated for 30 min with GVs modified to produce non-linear signal, transferred to GV-free media for predetermined periods of time, and loaded into an agarose phantom for non-linear xAM imaging. **F)** Representative xAM images of cell pellets pre-treated with DMSO (top) or 100 nM bafilomycin A1 (bottom) at the indicated times after GV uptake. Scale bars, 1 mm. **G)** Time course of xAM signal intensity in cell pellets, normalized to the initial timepoint. Error bars represent ± SEM. N = 4-10 per timepoint. Welch's t-test (*: $p<0.05$; **: $p<0.01$).

3.3.4 GV pharmacokinetics can be used to monitor disease progression

The results presented thus far confirm that upon IV injection, GVs are filtered from the blood by liver macrophages and subsequently catabolized in the lysosome (**Fig. 3-4a**). This process can be described with a two-compartment pharmacokinetic model comprising the blood and liver, whose rate constants parametrize the concurrent processes of phagocytosis and lysosomal degradation (**Fig. 3-4b**), with contrast enhancement linearly proportional to intact GV concentration in each compartment (**Fig. 3-S4**). By fitting this model to the dynamics of GV ultrasound contrast in the vasculature and liver *in vivo*, we can thus non-invasively quantify macrophage phagolysosomal function (**Fig. 3-4c**, input data shown in **Fig. 3-S5**). The assumption that ultrasound signal time courses are representative of true pharmacokinetics is based on two key observations: GVs are stable under our imaging parameters, so changes in signal are due to active biological processes; and GVs are primarily taken up by liver macrophages, with increases in liver AM contrast matched by decreases in

brain Doppler contrast. For simplicity, we further assume each process to be first-order and neglect the initial distribution dynamics during GV infusion by considering timepoints occurring after the peak in Doppler signal. Using this approach, we calculated rates of 0.167 min^{-1} and 0.041 min^{-1} for uptake and degradation, respectively, in healthy mice (**Fig. 3-4d**, **Table 3-S1**).

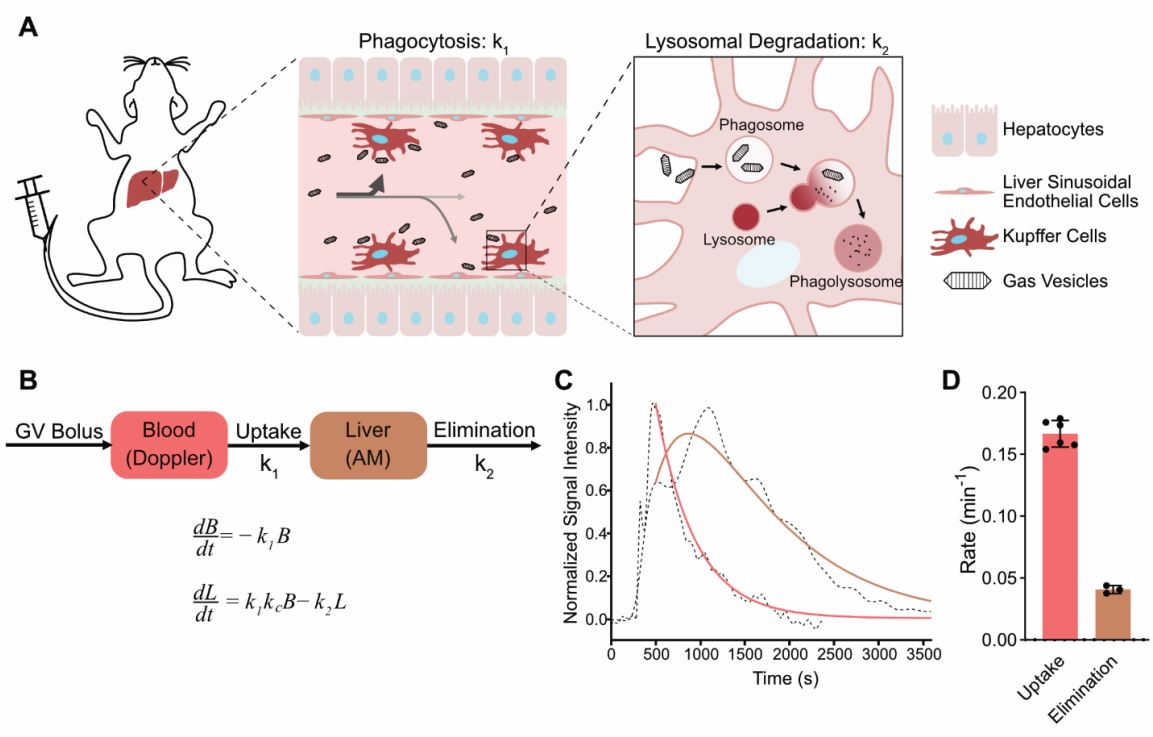

Figure 3-4: Quantification of phagocytic and lysosomal activities in mouse liver macrophages. **A)** Proposed GV clearance pathway. Upon IV infusion, GVs are phagocytosed from the blood by liver-resident macrophages and degraded by lysosomal proteolysis. **B)** Pharmacokinetic model of GV clearance. Fitting this model to GV signal time courses enables quantification of macrophage function. Uptake and degradation rates are represented by k_1 and k_2, respectively, and k_c is a correction factor that enables conversion between the two imaging modes and accounts for uptake in other tissues. **C)** Representative plot of vascular and liver ultrasound signal time courses in healthy mice (dashed lines) and corresponding fitted curves (solid lines). **D)** Uptake and elimination rates obtained by fitting model to data from Fig. 3-1, c-d. Error bars represent ± SD.

Having established a method to quantify liver macrophage function, we next evaluated its ability to detect pathological disruption of the RES. First, we administered two doses of liposomal clodronate—0.40 mg/kg and 30 mg/kg—to partially or fully deplete Kupffer cells in the liver. Histological evaluation confirmed that 31% of the Kupffer cell population remained at the lower dose, decreasing to 16% at the higher dose (**Fig. 3-5a; Fig. 3-S6**). Interestingly, *ex vivo* imaging of organ fluorescence revealed that most GVs are still cleared by the liver (**Fig. 3-5b**). However, closer inspection of liver sections with immunofluorescence showed GVs tending to localize to the sinusoidal margins, suggesting uptake by liver sinusoidal endothelial cells (LSECs) (**Fig. 3-S7**). This is consistent with a recent study showing that LSECs upregulate phagocytic activity upon depletion of nearby Kupffer cells.[7] Based on these results, we expected that GVs would circulate longer in the blood in clodronate-treated animals due to diminished phagocytic potential, and that their residence time in the liver would increase due to less efficient lysosomal degradation by non-macrophage cells. Indeed, fitting our model to the normalized hemodynamic Doppler (**Fig. 3-5c**) and liver AM (**Fig. 3-5d**) signal time courses yielded uptake and degradation rates substantially lower than those of healthy mice (**Fig. 3-5e**). Specifically, phagocytosis rates were reduced by 66% and 82% at the low and high doses of clodronate, while proteolysis rates were reduced by 27% and 57%, respectively. Notably, phagocytosis rates were proportional to the macrophage population.

For our second model of RES dysfunction, we imaged mice with NAFLD. This disease is characterized by liver infiltration of pro-inflammatory M1-polarized macrophages[5,46] which have lower phagocytic[13,17,34,47] and lysosomal activities[15] than the

normally anti-inflammatory Kupffer cells.[48] We induced NAFLD by feeding mice with a methionine- and choline-deficient (MCD) diet[5,49] and performed ultrasound imaging after 4 weeks of this treatment (**Fig. 3-5f**). Histological evaluation confirmed the appearance of widespread steatosis, a hallmark of NAFLD (**Fig. 3-5f**). In line with our hypothesis, diseased mice had significantly suppressed phagocytic and lysosomal functions: uptake rate was reduced by 35% while degradation rate was reduced by 58% (**Fig. 3-5, g-i**). We verified that these differences are not due to saturation of the smaller livers of MCD mice[50] by GVs (**Fig. 3-S8**). When we simulated therapeutic intervention by reverting to a control diet for 3 additional weeks, the steatosis subsided (**Fig. 3-5f**) and phagolysosomal activity returned to its original level (**Fig. 3-5, g-i**). Compared to age-matched litter-mate controls, these "recovered" mice showed a slight decrease in degradation rate but no discrepancies in uptake rate (**Fig. 3-S9**, **Table 3-S1**). Taken together, our results demonstrate the capability of GV-enhanced ultrasound to non-invasively visualize macrophage malfunction as a biomarker of disease.

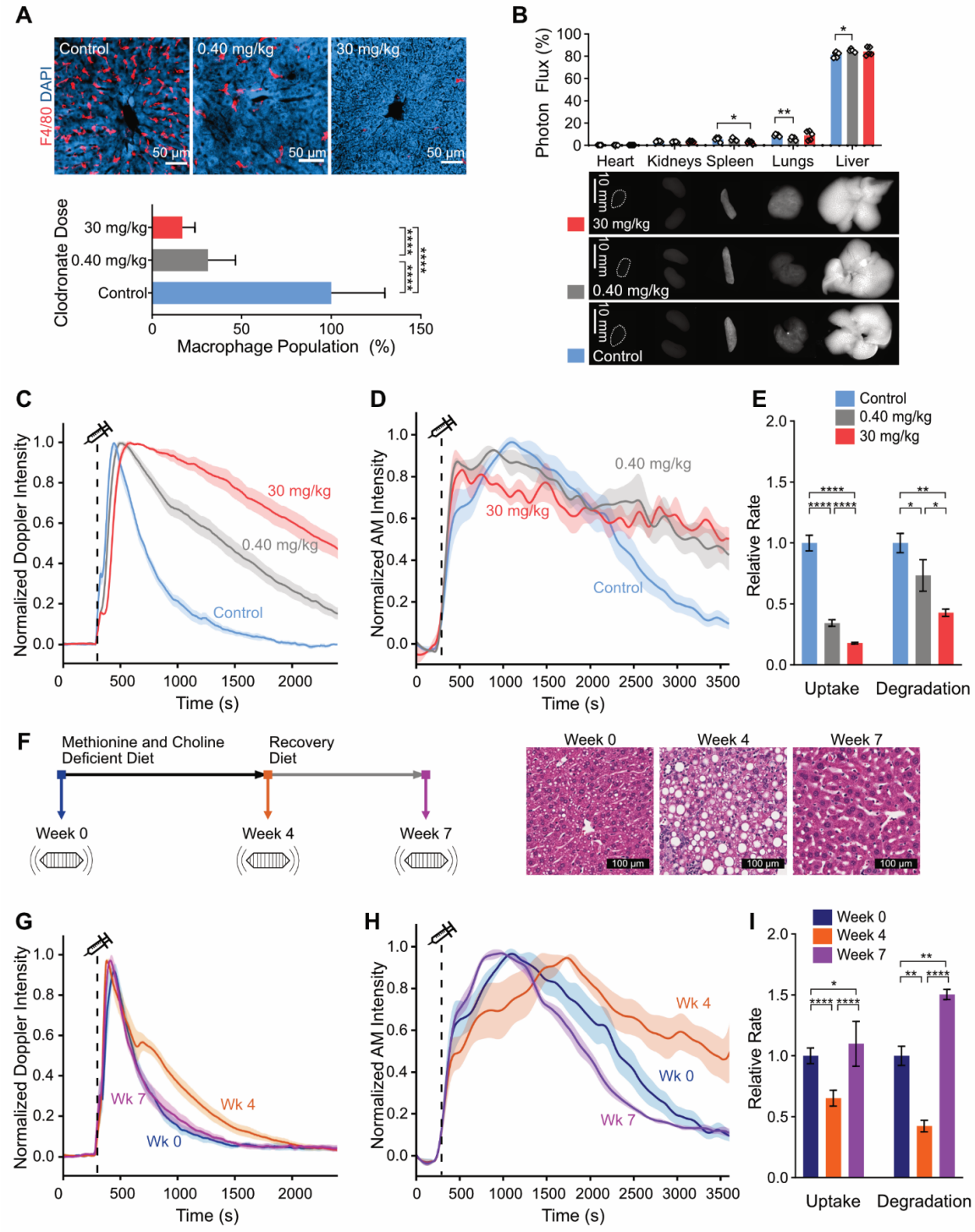

Figure 3-5: Monitoring disease progression by functional imaging of phagolysosomal activity. **A)** Macrophage population in response to clodronate dose. Top: Representative immunofluorescence

confocal micrographs of liver sections labeled with anti-F4/80 (macrophages) and DAPI. Scale bars, 50 μm. Bottom: Macrophage population determined by segmentation with ilastik, normalized to the mean from control livers. Error bars represent ± SD. N = 3 biological replicates, >100 total fields of view. Welch's t-test (****: $p<0.0001$). **B)** Biodistribution of fluorescently-labeled GVs 1h after injection. Bottom: Representative fluorescence images of excised organs. Due to their low fluorescence, the hearts are circled with dashed lines. Scale bars, 10 mm. Top: Percentage of collected photons originating from each organ. Error bars not shown. N = 5. Welch's t-test (*: $p<0.05$; **: $p<0.001$). **C-D)** Normalized time courses of Doppler signal enhancement in the brain (**C**) and AM signal in the liver (**D**) following GV injection in clodronate-treated mice**.** Dashed lines, time of GV injection (300 s); thick lines, mean; shaded areas, ± SEM. N = 4-6. **E**) Uptake and degradation rates obtained by fitting the model in Fig. 4b to each distinct combination of time courses from **C** and **D**, normalized to those of healthy mice. Error bars represent ± SD. Welch's t-test (*: $p<0.05$; **: $p<0.01$; ***: $p<0.001$; ****: $p<0.0001$). **F)** Left: Timeline of NAFLD induction. Mice were fed with a methionine and choline deficient diet for 4 weeks, followed by an additional 3 weeks with a control diet. Right: Representative images of H&E stained liver sections. Scale bars, 100 μm. **G-H)** Normalized time courses of Doppler signal enhancement in the brain (**G**) and AM signal in the liver (**H**) following GV injection in mice with NAFLD. Dashed lines, time of GV injection (300 s); thick lines, mean; shaded areas, ± SEM. N = 4-5. **I,** Uptake and degradation rates obtained by fitting the model in Fig. 4b to the time courses in **G** and **H**, normalized to those of healthy (Week 0) mice. Error bars represent ± SD. Welch's t-test (**: $p<0.01$; n.s: $p>0.05$).

3.4 Conclusions

GVs are advantageously positioned to image *in vivo* phagolysosomal function due to their inherent stability at ambient conditions, susceptibility to natural proteolytic degradation and dependence on shell integrity for ultrasound contrast. When combined with a simple pharmacokinetic model, GV imaging makes it possible to parametrize macrophage activity in terms of phagocytosis and lysosomal degradation rates, clearly delineating healthy and disease states, as demonstrated in two models of RES deficiency.

The diagnostic power of macrophage functional imaging arises from the dependence of phagolysosomal kinetics on cellular phenotype which, in turn, reflects the local tissue and inflammatory microenvironment. Moving forward, this capability could be refined by application of GVs engineered to display surface ligands,[27] as phenotype-specific responses

to certain particle-bound domains may augment differences in degradative behavior.[51] Methods to alter GV biodistribution would enable targeting and functional assessment of macrophages in tissues other than the liver. Additionally, the ability to genetically express GVs[23] could enable study of intracellular proteolytic processes, such as autophagy and proteasomal degradation.

To maximize the translational utility of this technology, three aspects could be improved. First, imaging parameters should be optimized for clinical use. In this study, we separately acquired ultrafast Doppler and non-linear AM images to maximize signal specificity. However, simultaneous multiplexed imaging of blood and liver signals would greatly streamline diagnostic use. This could be accomplished by intercalating amplitude modulation images with Doppler images of the liver, enabling GV quantitation in both compartments with a single, stationary transducer. Second, while GV administration at doses similar to those used in our experiments does not result in acute, adverse health effects in mice,[19] clinical translation would require formal studies of dose-limiting and long-term toxicity. In addition, to support long-term monitoring of individual subjects, it would be useful to better understand the immunogenicity of GVs and the impact of repeated injections, as the development of antibodies may skew clearance kinetics.[52] Finally, in some applications it may be useful to image GVs with other imaging modalities, such as magnetic resonance imaging[28,29] and optical coherence tomography;[53] adaptation of phagolysosomal imaging to these modalities would facilitate applications where the efficacy of ultrasound may be limited.

In summary, the combination of nanoscale, lysosomally-degradable contrast agents and quantitative ultrasound imaging enables non-invasive assessment of macrophage function as a disease-relevant biomarker. This technology will broaden the diagnostic capabilities of biomolecular ultrasound and motivate further methods for non-invasive characterization of cellular function.

3.5 Methods

GV preparation and quantification

Native gas vesicles (GVs) were isolated from *Anabaena flos-aquae* as previously described.[20] Concentrations were measured by optical density (OD) at 500 nm using a spectrophotometer (NanoDrop ND-1000, Thermo Scientific). Stripped GVs were prepared by treatment of native GVs with 6M urea solution followed by two rounds of centrifugally-assisted flotation and removal of the subnatant.[20] Fluorescently-labeled gas vesicles were prepared by mixing GVs at OD 10 in 1x phosphate-buffered saline (PBS) with 6 μM Alexa Fluor 647 NHS Ester (Invitrogen, prepared as 10 mM solution in dimethyl sulfoxide). Dually-labeled GVs were prepared by mixing GVs at OD10 with 6 μM pHrodo Red succinimidyl ester (Invitrogen, prepared as 10 mM solution in dimethyl sulfoxide) and 18 μM Alexa Fluor 647 NHS Ester (Invitrogen, prepared as 10 mM solution in dimethyl sulfoxide). After rotating in the dark at 25°C for 1 h, the reactions were quenched with Tris-HCl. Prior to use, all GVs were buffer exchanged into 1x PBS by two rounds of overnight dialysis through a regenerated cellulose membrane (12-14 kD MWCO, Repligen).

Cell culture

RAW264.7 (TIB-71) and HEK293T (CRL-3216) cells were ordered from the American Type Culture Collection (ATCC). Cells were cultured on tissue culture treated 10-cm dishes in Dulbecco's Modified Eagle Medium (DMEM) supplemented with 10% Fetal Bovine Serum and 1% penicillin/streptomycin.

Lentiviral transduction. Plasmid constructs were designed with SnapGene (GSL Biotech) and assembled with Gibson Assembly reagents from New England Biolabs. Briefly, mWasabi[54] was inserted downstream of a 20-AA palmitoylation tag from GAP43 and expressed under the EF-1α promoter (gift from Dan I. Piraner[55]). This plasmid was then transfected along with third-generation lentiviral vector and helper plasmids (kind gifts from the laboratory of David Baltimore) into HEK293T cells using polyethyleneimine (PEI). Following a 12 h incubation, PEI-containing media was replaced with fresh media supplemented with 10 mM sodium butyrate (Sigma Aldrich). Viral particles were concentrated 48 h later *via* ultracentrifugation. RAW264.7 cells were transduced by spinfection. Briefly, concentrated virus was added to non-tissue culture treated 24-well plates coated with RetroNectin (Takara Bio). Following centrifugation (2,000xg, 2h), 4e5 RAW264.7 cells in 1 mL media were added to each well. The plates were spun again at 900xg for 50 min before transferring to the incubator. The brightest 10% of cells were selected with a BD FACSAria III (BD Biosciences) at the City of Hope Analytical Cytometry Core Facility.

Preparation of fibronectin-treated cover slips. Ethanol sterilized square (22 mm x 22 mm) #1.5H glass cover slips (Thorlabs) were individually placed into the wells of a 6-well plate and immersed in 2 mL PBS containing 10 μg fibronectin from bovine plasma (Sigma Aldrich) for 2h at room temperature. The fibronectin solution was then aspirated and the plates stored at 4°C until use. Sterile glass-bottom 35mm dishes (MatTek) were similarly coated with 2.5 μg fibronectin in 500 μL PBS.

Animal preparation and disease models

All *in vivo* experiments were performed on male C57BL/6J mice (The Jackson Laboratory) under protocols approved by the Institutional Animal Care and Use Committee at the California Institute of Technology.

Macrophage depletion. Liposome-encapsulated clodronate (Clodrosome, Encapsula NanoSciences) was administered through the lateral tail vein 48 h prior to imaging. Mice receiving a dose of 30 mg/kg were injected with undiluted liposome suspension, while mice receiving the lower dose of 0.40 mg/kg were injected with liposomes diluted 1:100 with sterile saline. Control mice were injected with the equivalent volume of undiluted PBS liposomes (Encapsome, Encapsula NanoSciences).

Diet-induced nonalcoholic fatty liver disease. 8-week old mice were free fed with either a methionine and choline deficient diet (5ADJ, TestDiet) or control diet (5CC7, TestDiet) for up to 4 weeks. Afterwards, all mice were fed the control diet for an additional 3 weeks. Because this dietary protocol often results in dramatic weight loss, the mice were monitored weekly for signs of adverse health. GV pharmacokinetics were measured at 2 weeks, 4 weeks and at the conclusion of the study. Immediately after ultrasound imaging, the mice were fixed *via* sequential transcardial perfusion of PBS and 10% neutral buffered formalin (Sigma Aldrich), and the livers were removed for histological assessment by the UCLA Translational Pathology Core Laboratory. Briefly, 4-µm sections were cut from paraffin-embedded organs, stained with hematoxylin & eosin, and imaged at 20x with a Leica Aperio slide scanner.

Ultrasound imaging

Transcranial ultrafast Doppler imaging. Mice (8-10 weeks old) were maintained under 1.5% isoflurane anesthesia on a temperature-controlled imaging platform with a rectal probe (Stoelting Co.). Following head depilation (Nair) and insertion of a catheter with a 30-g needle into the lateral tail vein (fixed in place with GLUture), the mice were head-fixed in a stereotaxic frame inside a light- and sound-proofed box on an optical table. A 16 MHz transducer (Vermon) connected to a programmable ultrasound scanner (Verasonics Vantage) was coupled to the head through a column of ultrasound gel (centrifuged at 2000xg, 10 min to remove bubbles). The transducer was positioned to capture a full coronal section at an arbitrary plane along the rostrocaudal axis. Once the internal temperature of the mouse stabilized at 37°C, power Doppler images were acquired every 4 s for up to 60 min using a

previously described functional ultrasound script with slight modifications.[25] Briefly, the pulse sequence consisted of 11 tilted plane waves (varying from -10 to 10 degrees), each containing 8-half-cycle emissions at a voltage of 15V (900 kPa peak positive pressure measured in free water tank). An ensemble of 250 coherently compounded frames, collected at a framerate of 500 Hz, was then processed through a singular value decomposition filter to isolate blood signals from tissue motion and generate a single power Doppler image. 300 s after the start of imaging, 100 μL OD30 native GVs were infused over 10 s by syringe pump. Pixel-wise signal enhancement was calculated as the ratio of intensity at each time point relative to its mean intensity in the first 75 frames. Time courses were then extracted by averaging signal enhancement within a manually defined region of interest encompassing the whole brain, processed with a 10-sample moving mean filter and normalized to the global maximum.

Liver amplitude modulation imaging. Mice (10-14 weeks) were maintained under 2% isoflurane anesthesia on a mouse heating pad controlled by a rectal probe (TCAT-2LV, Physitemp Instruments). After depilation of the abdomen (Nair) and insertion of a 30-g tail vein catheter, the mice were secured in a supine position with surgical tape. Ultrasound imaging was performed with an 18 MHz, 128-element linear array transducer (L22-14v, Verasonics) mounted on a custom-made manual translation stage and positioned such that the liver was at approximately 8 mm in depth. Once the internal temperature of the mouse stabilized at 37°C, B-mode and amplitude modulation images were simultaneously acquired every 4 s for up to 90 min. All images were reconstructed from 128 focused beam ray lines. Each ray line was transmitted at 18 MHz from a 32-element active aperture with a focal depth of 8 mm and peak positive pressure of 600 kPa (measured in free water tank). B-mode images were reconstructed from a single pulse, while amplitude modulation was implemented by first transmitting a single pulse from the full active aperture, followed by two pulses where the even and odd elements in the active aperture are sequentially silenced.[24] Stripped GVs (OD 30, 100 μL) were manually injected as a bolus after 300 s. Image processing and display were performed by internal Verasonics programs. Time courses were calculated as the

average signal intensity within a manually defined rectangular region of interest encompassing the liver. To enable comparison, the time courses were smoothed by robust locally weighted-regression using linear least squares, baseline corrected with respect to the first 75 time points and normalized to the global maximum.

In vitro macrophage imaging. Wild-type RAW264.7 cells were seeded onto fibronectin-coated cover slips (2e6 cells/2mL DMEM). After 24 h, the culture media was exchanged with fresh DMEM containing bafilomycin A1 (100 nM) or vehicle (0.01% v/v DMSO). Media of the same composition was used for all subsequent steps. Following a 1 h pretreatment, a GV suspension composed of 320 μL fresh media and 80 μL stripped GVs (OD10 in PBS) was dropped at the center of a UV-sterilized Parafilm-lined 6-well plate and a cover slip was floated on top, cell-side down. This GV suspension was freshly prepared immediately prior to uptake. After incubation at 37°C for 30 min, the cover slips were transferred to pre-warmed fresh media and incubated for the desired amount of time. The media was then aspirated and the cover slips were gently washed once with 2 mL room temperature PBS. Cells were detached with 500 μL 0.25% trypsin-EDTA (Genesee Scientific), neutralized with 1 mL media, and pelleted by centrifugation (300xg, 5 min, 4°C). From this point on, special care was taken to minimize exposure of the cells to temperatures above 4°C. The pellet was washed once with 1.4 mL ice-cold PBS and resuspended in 50 μL cold serum-free DMEM with 25 mM HEPES before loading into an ultrasound phantom (1% agarose in PBS). Cell densities were manually counted by hemocytometer.

The phantoms were imaged with a 128-element linear array transducer (L10-4v, Verasonics) mounted on a custom manual translation stage using a previously described cross-propagating amplitude modulation pulse sequence[26] that was modified to acquire single frames. Briefly, each frame consisted of 64 ray lines transmitted at 4V (400 kPa peak positive pressure in water) and 6 MHz from a 65-element aperture. Within the active aperture, amplitude modulation was implemented by sequentially sending a plane wave angled at 19.5° from the first 32 elements, a plane wave angled at -19.5° from the last 32 elements,

followed by simultaneous emission of both plane waves. The first 3 frames were saved along with a post-collapse image (after 10 insonations at 30 V). Signal intensities were extracted from manually selected circular regions of interest with diameters of 1.8 mm, baseline corrected by subtraction of signal from the post-collapse image, and adjusted for cell density. The time courses from each run were then normalized to the mean intensity from the samples harvested immediately after uptake (t=0).

GV contrast measurement. Phantoms were constructed as previously described.[19] Briefly, phantoms were made by embedding stripped GVs in 1% agarose in PBS and imaged with the same parameters used for liver imaging. Signal intensities were extracted from manually defined regions of interest.

Fluorescence imaging

Whole organ fluorescence. Mice were prepared as described above for transcranial neuroimaging, with the only modification being that the GVs were fluorescently-labeled with Alexa Fluor 647. Ninety minutes after GV injection, the mice were transcardially perfused with 30 mL of cold heparinized PBS (10 U/mL, Sigma Aldrich). The heart, lungs, kidneys, spleen, and liver were then carefully excised and stored in ice-cold Fluorobrite DMEM (Gibco) prior to analysis. Images were acquired on a Bio-Rad ChemiDoc MP imaging system using red epi-illumination and a 695/55 nm filter with an exposure time of 0.5 s. Integrated intensities were then calculated using the built-in "Analyze Particles" function in FIJI.

Immunofluorescence. Mice were prepared as described above for whole organ fluorescence. Ninety minutes after GV injection, the mice were transcardially perfused with 30 mL of cold heparinized PBS, followed immediately by 20 mL 10% neutral buffered formalin. The liver and spleen were removed and immersed in formalin overnight (4°C). Each organ was then sectioned with a vibrating microtome (75 μm, Compresstome, Precisionary Instruments). Slices were blocked and permeabilized (2h, rt) with PBS containing 10% goat serum (Sigma Aldrich), 0.2% Triton X-100 (Fisher Scientific), and 0.1% sodium azide (Sigma Aldrich).

Each slice was stained for macrophages with rat anti-mouse F4/80 (BioLegend, 1:200 dilution, overnight, 4°C) and Alexa Fluor 594 goat anti-rat IgG secondary antibody (2h, rt, 1:400 dilution). The sections were mounted with ProLong Diamond with DAPI (Invitrogen) and allowed to harden overnight before imaging with a Zeiss LSM 800 confocal microscope through a 10x or 20x objective. Imaging parameters prioritized signal specificity over speed.

Confocal microscopy images of entire liver slices were background subtracted in FIJI (20 px, rolling ball method). Randomly selected 500 px by 500 px regions of interest—simulating the sampling of arbitrary fields of view –were exported to Ilastik[41] for processing. The "Density Counting" workflow was used to count macrophages (**Fig. S6**). Images were also segmented into macrophage and non-macrophage regions with the "Pixel Classification" workflow and loaded into MATLAB for colocalization analysis (**Fig. S3**).

Live-cell imaging. 1e5 RAW264.7 cells expressing palmitoylated mWasabi were seeded on fibronectin-treated 35mm glass-bottom dishes. After 24 h, the culture media was exchanged with serum-free Fluorobrite DMEM containing 25 mM HEPES and either 100 nM bafilomycin A1 (Cayman Chemical) or vehicle (0.01% v/v DMSO). Following a 1 h incubation, this media was replaced with a 200 μL freshly-prepared suspension of OD 1.2 dually-labeled GVs. The well was then sealed with a UV-sterilized 18mm circular glass cover slip and inverted for 5 min at 37°C to allow for contact and uptake.

Laser scanning confocal images were acquired every 2 min for 1h on a Zeiss LSM 800 microscope with a large incubation chamber maintained at 37°C. High magnification images were acquired through a 63x oil immersion objective. Population level images were acquired through a 20x objective. In both cases, acquisition parameters were set to optimize speed. Image files were loaded into FIJI, visualized by maximum intensity projection, de-speckled with a 1-px median filter and quantified by integration of signal intensities across the entire field of view.

Pharmacokinetic modeling

A two-compartment pharmacokinetic model was implemented in MATLAB as the following system of ordinary differential equations:

$$(1)\ \frac{dB}{dt} = -k_1 B$$

$$(2)\ \frac{dL}{dt} = k_1 k_c B - k_2 L$$

where B represents GV contrast in the blood and L represents GV contrast in the liver. These variables were then directly parametrized with normalized Doppler and AM signal time courses, respectively, and the constants were derived by non-linear least squares curve fitting with initial values of 0 and bounds of 0 to 1. k_1 and k_2 represent rates of phagocytosis and lysosomal degradation, respectively. k_c is a constant relating the blood Doppler signal to the liver nonlinear signal. Input data were all distinct combinations of Doppler and AM time courses from each biological condition. Output values are tabulated in **Table 4-S1**.

Statistical analysis

Sample sizes were chosen based on preliminary experiments to yield sufficient power for the proposed comparisons. Statistical methods are described in applicable figure captions.

3.6 Supplementary Information

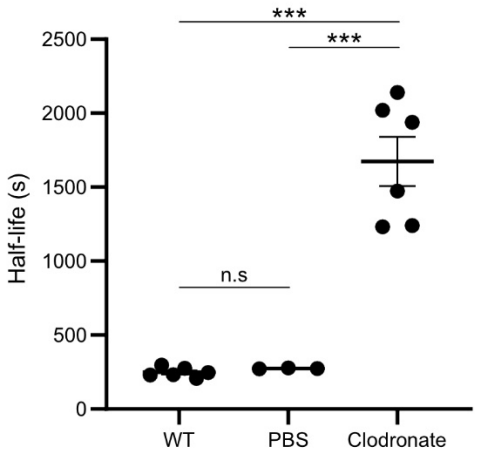

Figure 3-S1: Circulation half-life of GVs, as measured by Doppler signal enhancement. Half-life was calculated as the time required for normalized signal enhancement to decline from its maximum at 1 to 0.5. Error bars represent ± SEM. N=6 (WT), 3 (PBS liposomes), 6 (clodronate liposomes). Welch's t-test (***:$p<0.001$; n.s: $p>0.05$).

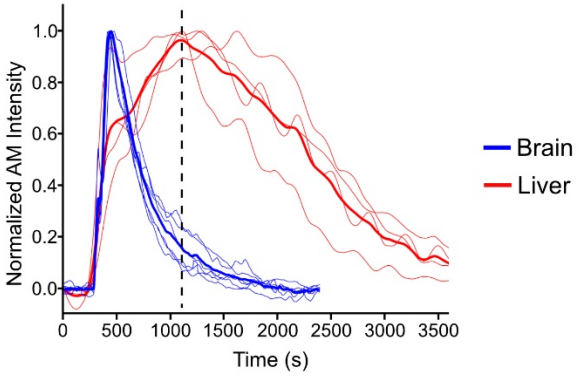

Figure 3-S2: Time courses of ultrasound contrast in the brain (blue, n = 6) and liver (red, n = 4) of healthy C57BL/6 mice. Ultrasound contrast is essentially transferred from the brain to the liver, with liver contrast reaching its maximum (dashed line) after brain contrast dissipates. Thin lines, individual trials; thick lines, mean.

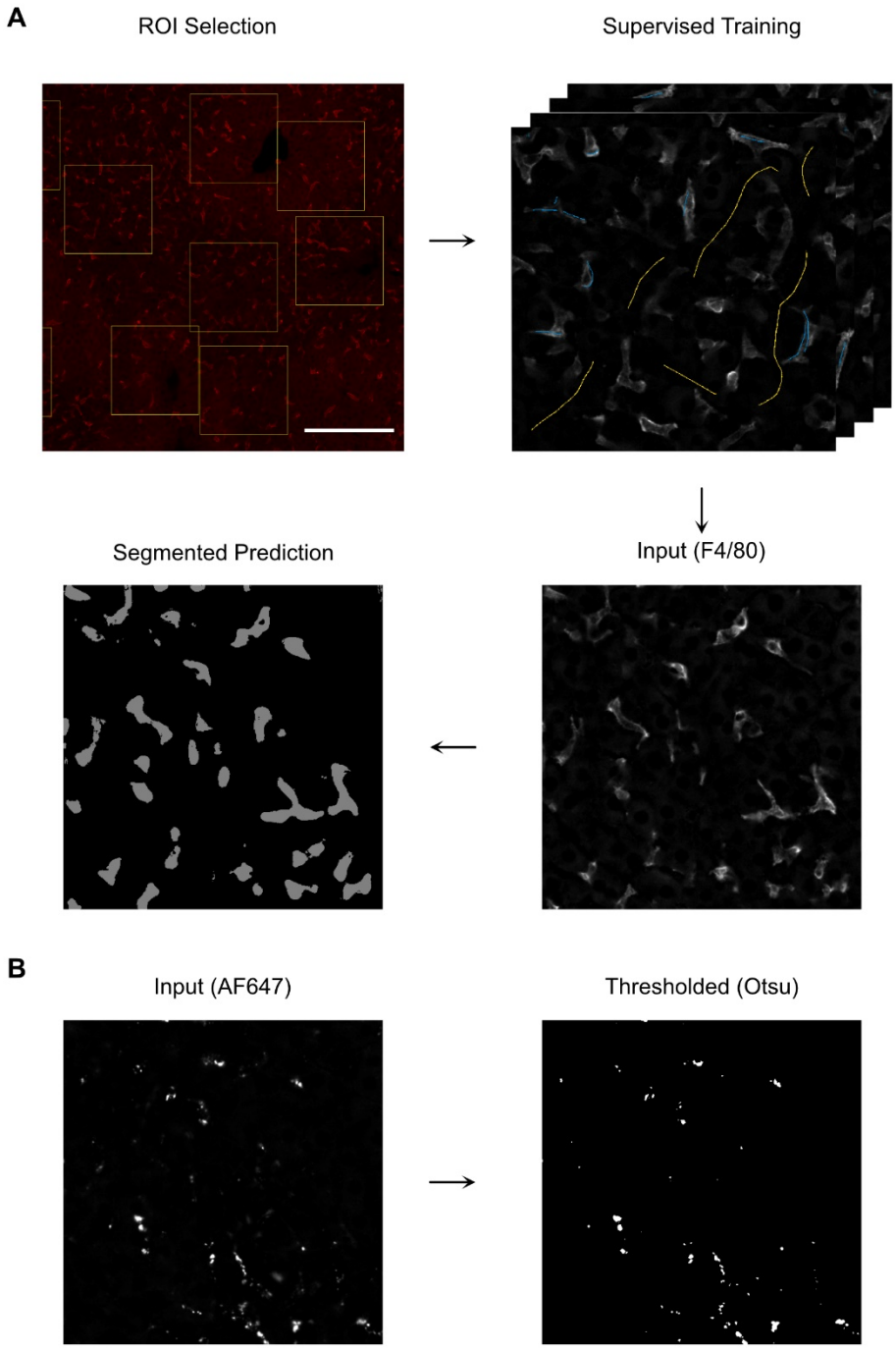

Figure 3-S3: Segmentation protocol. **A)** Non-overlapping 500 px x 500 px (approx. 200 µm) ROIs were extracted from confocal micrographs of liver slices stained with anti-F4/80 (acquired with 20x objective, scale bar: 200 µm). We trained our Pixel Classification algorithm in ilastik by labeling background and macrophage regions on a subset of our images. Then, we segmented the

remaining images by processing with the trained network. **B)** The corresponding images in the AF647 (GV) channel were automatically thresholded by Otsu's method, and colocalization was assessed in MATLAB.

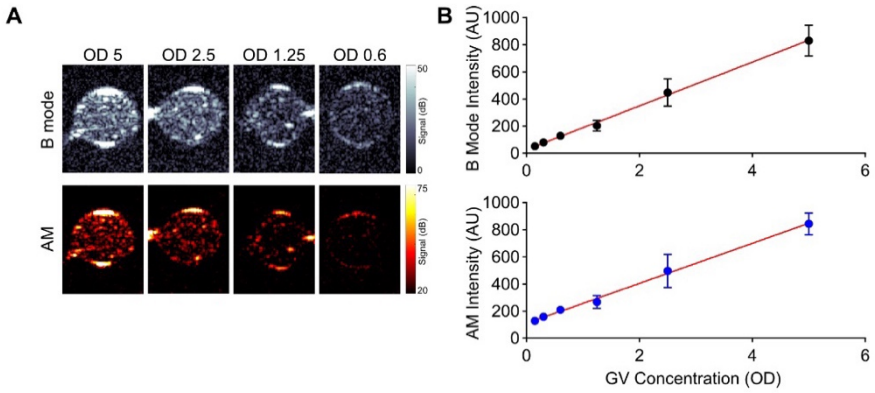

Figure 3-S4: Ultrasound contrast is linear with respect to GV concentration. **A)** Representative B mode and AM images of non-linear GVs embedded in 1% agarose. Wells are approx. 2 mm in diameter. **B)** B mode (top) and AM (bottom) signal intensities. N = 12.

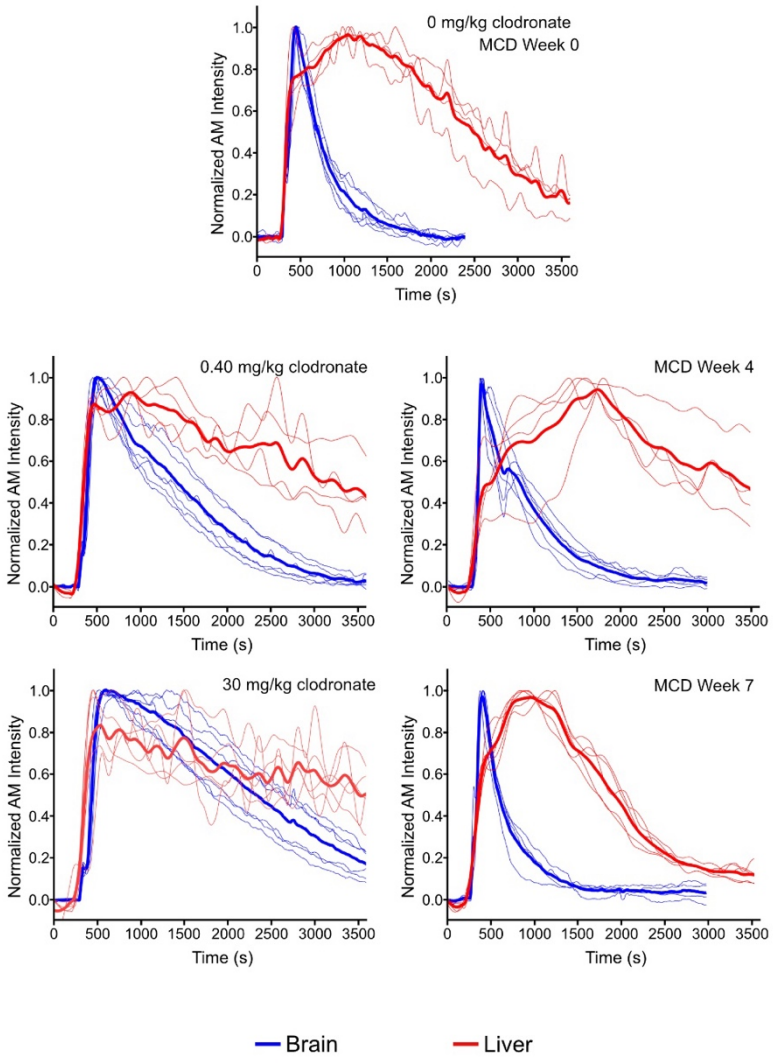

Figure 3-S5: Ultrasound signal time courses used for estimating pharmacokinetic parameters. Brain, blue lines; liver, red lines; thin lines, individual trials; thick lines, mean.

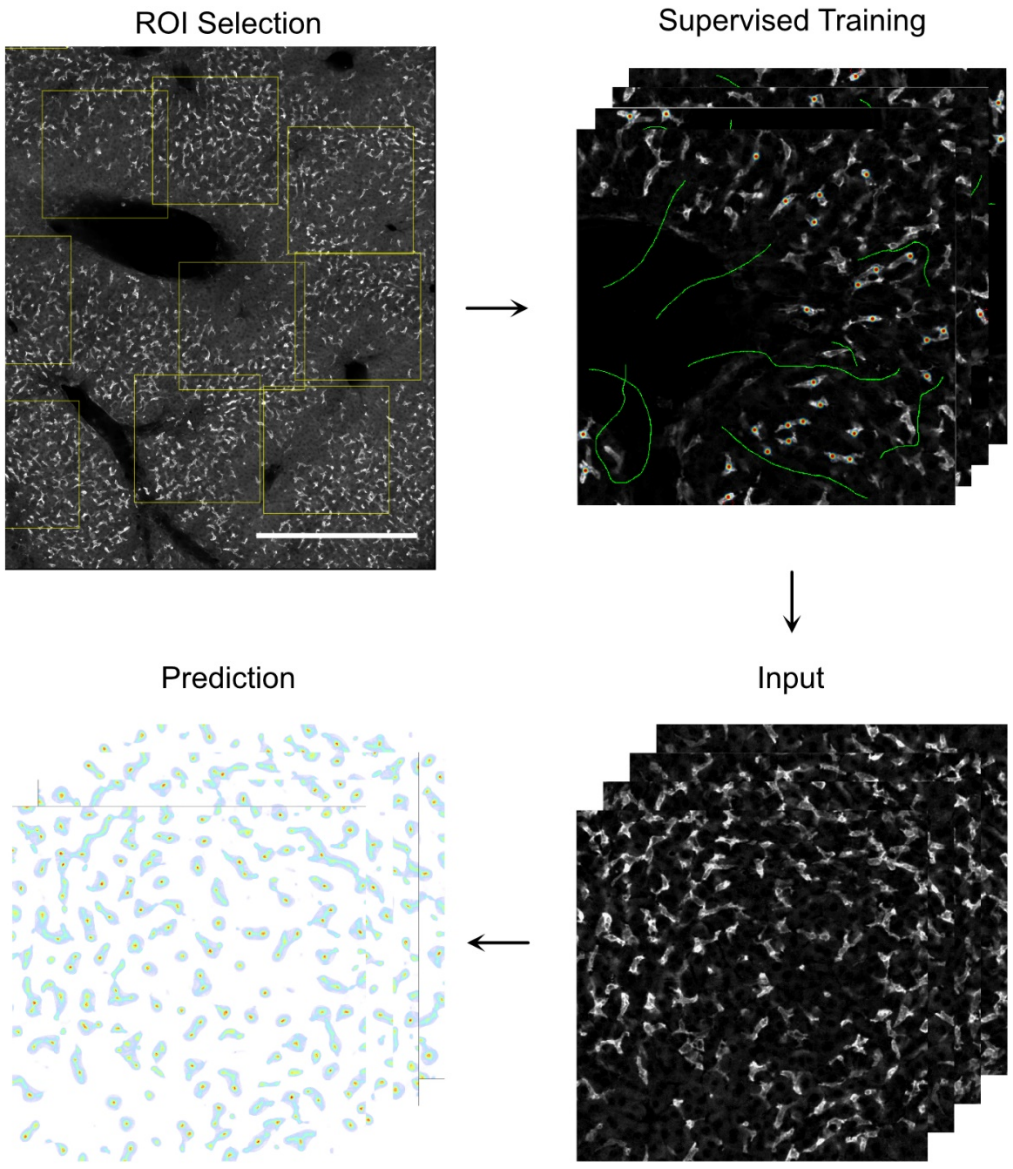

Figure 3-S6: Processing for macrophage counting. Non-overlapping 500 px x 500 px (approx. 400 µm) ROIs were extracted from confocal micrographs of liver slices stained with anti-F4/80 (acquired with 10x objective, scale bar: 500 µm). Using the Density Counting workflow in ilastik, we annotated a subset of these images for background and cell bodies. Then, we processed the remaining images with our trained algorithm to predict macrophage density.

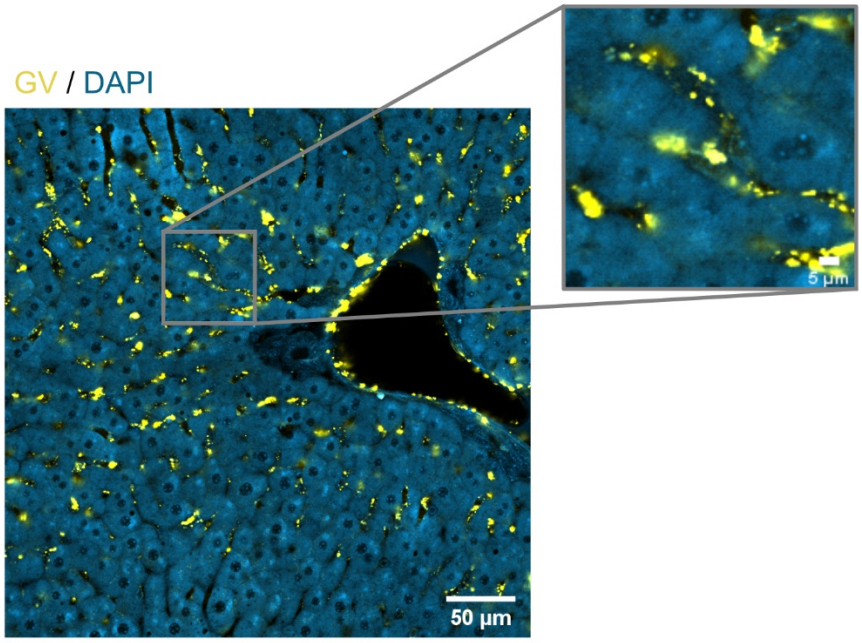

Figure 3-S7: Confocal microscopy image of a liver section from a mouse treated with 30 mg/kg clodronate demonstrating localization of GVs to the sinusoidal periphery. Scale bars: 50 µm. Inset: 5 µm.

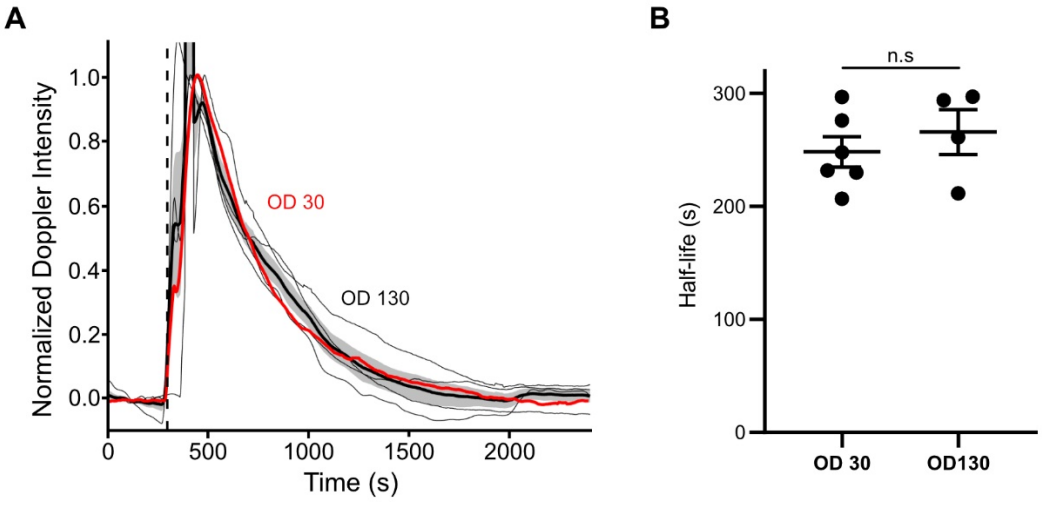

Figure 3-S8: Hepatic clearance does not saturate under experimental conditions. **A)** Time course of ultrafast Doppler signal enhancement following IV injection of purified GVs at 300 s (dashed line). Individual traces, shown as thin lines, were normalized to their respective maxima. The thick line represents the mean of N = 4 biological replicates. Shaded area represents ± SEM. **B)** Half-lives of signal enhancement following IV injection of 100 μL GVs at OD30 or OD130. Welch's t-test(n.s: p>0.05).

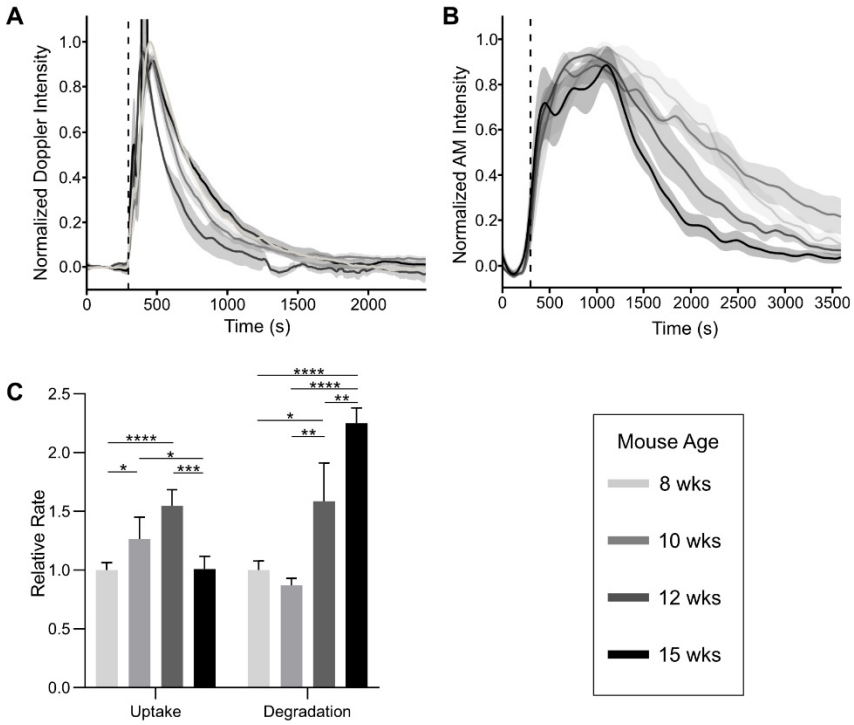

Figure 3-S9: Hepatic macrophage activity changes with age. **A)** Time course of Doppler signal enhancement in mice of different ages following GV injection. Shaded areas represent ± SEM. N = 4-6 **B)** Time course of liver AM signal. Shaded areas represent ± SEM. N=3-5 **C)** Rates of GV uptake and degradation relative to those of 8 week old mice. Error bars represent ± SD. N=3-5. Welch's t-test(*:p<0.05; **:p<0.01).

Condition	Uptake Rate (min^{-1}, ± SD)	Degradation Rate (min^{-1}, ± SD)	k_c (± SD)
0 mg/kg clodronate	0.1667 ± 0.0107	0.0407 ± 0.0032	0.7572 ± 0.2328
0.40 mg/kg clodronate	0.0574 ± 0.0045	0.0299 ± 0.0053	0.6073 ± 0.2587
30 mg/kg clodronate	0.0299 ± 0.0010	0.0175 ± 0.0012	0.3843 ± 0.4507
MCD: 0 weeks	0.1667 ± 0.0107	0.0407 ± 0.0032	0.7572 ± 0.2328
MCD: 4 weeks	0.1087 ± 0.0108	0.0172 ± 0.0019	0.7268 ± 0.2899
MCD: 7 weeks	0.1818 ± 0.0068	0.0612 ± 0.0017	1.0000 ± 0.0000
Age: 8 weeks	0.1667 ± 0.0107	0.0407 ± 0.0032	0.7572 ± 0.2328
Age: 10 weeks	0.2108 ± 0.0310	0.0354 ± 0.0025	0.6478 ± 0.0859
Age: 12 weeks	0.2577 ± 0.0229	0.0645 ± 0.0132	0.9576 ± 0.0752
Age: 15 weeks	0.1681 ± 0.0181	0.0916 ± 0.0052	0.8879 ± 0.1546

Table 3-S1: Constants derived from fitting pharmacokinetic model to ultrasound data. k_1, uptake rate; k_2, degradation rate; k_c, conversion constant.

References

1. Tavares, A. J. *et al.* Effect of removing Kupffer cells on nanoparticle tumor delivery. *Proc. Natl. Acad. Sci. U. S. A.* **114**, E10871–E10880 (2017).
2. Berg, R. D. *et al.* Lysosomal disorders drive susceptibility to tuberculosis by compromising macrophage migration. *Cell* **165**, 139–152 (2016).
3. Block, M. L., Zecca, L., & Hong, J.-S. Microglia-mediated neurotoxicity: Uncovering the molecular mechanisms. *Nat. Rev. Neurosci.* **8**, 57–69 (2007).
4. Wang, C. *et al.* Microglia mediate forgetting via complement-dependent synaptic elimination. *Science* **367**, 688–694 (2020).
5. Kazankov, K. *et al.* The role of macrophages in nonalcoholic fatty liver disease and nonalcoholic steatohepatitis. *Nat. Rev. Gastroenterol. Hepatol.* **16**, 145–159 (2019).
6. Netea, M. G. *et al.* A guiding map for inflammation. *Nat. Immunol.* **18**, 826–831 (2017).
7. Poon, W. *et al.* Elimination pathways of nanoparticles. *ACS Nano* **13**, 5785–5798 (2019).
8. Tsoi, K. M. *et al.* Mechanism of hard-nanomaterial clearance by the liver. *Nat. Mater.* **15**, 1212–1221 (2016).
9. Chow, A., Brown, B. D., & Merad, M. Studying the mononuclear phagocyte system in the molecular age. *Nat. Rev. Immunol.* **11**, 788–798 (2011).
10. Blanco, E., Shen, H., & Ferrari, M. Principles of nanoparticle design for overcoming biological barriers to drug delivery. *Nat. Biotechnol.* **33**, 941–951 (2015).
11. Anstee, Q. M., Reeves, H. L., Kotsiliti, E., Govaere, O., & Heikenwalder, M., From NASH to HCC: Current concepts and future challenges. *Nat. Rev. Gastroenterol. Hepatol.* **16**, 411–428 (2019).
12. Maresca, D. *et al.* Biomolecular ultrasound and sonogenetics. *Annu. Rev. Chem. Biomol. Eng.* **9**, 229–252 (2018).
13. MacParland, S. A. *et al.* Phenotype determines nanoparticle uptake by human macrophages from liver and blood. *ACS Nano* **11**, 2428–2443 (2017).
14. Russell, D. G., VanderVen, B. C., Glennie, S., Mwandumba, H., & Heyderman, R. S. The macrophage marches on its phagosome: Dynamic assays of phagosome function. *Nat. Rev. Immunol.* **9**, 594–600 (2009).
15. Canton, J., Khezri, R., Glogauer, M., & Grinstein, S. Contrasting phagosome pH regulation and maturation in human M1 and M2 macrophages. *Mol. Biol. Cell* **25**, 3330–3341 (2014).
16. Iijima, H. *et al.* Decrease in accumulation of ultrasound contrast microbubbles in non-alcoholic steatohepatitis. *Hepatol. Res.* **37**, 722–730 (2007).
17. Yoshikawa, S. *et al.* Crucial role of impaired Kupffer cell phagocytosis on the decreased Sonazoid-enhanced echogenicity in a liver of a nonalcoholic steatohepatitis rat model. *Hepatol. Res.* **40**, 823–831 (2010).
18. Walsby, A. E., Gas vesicles. *Microbiol. Rev.* **58**, 94–144 (1994).
19. Shapiro, M. G. *et al.* Biogenic gas nanostructures as ultrasonic molecular reporters. *Nat. Nanotechnol.* **9**, 311–316 (2014).
20. Lakshmanan, A. *et al.* Preparation of biogenic gas vesicle nanostructures for use as contrast agents for ultrasound and MRI. *Nat. Protoc.* **12**, 2050–2080 (2017).

21. Bourdeau, R. W. *et al.* Acoustic reporter genes for noninvasive imaging of microorganisms in mammalian hosts. *Nature* **553**, 86–90 (2018).
22. Farhadi, A. *et al.* Recombinantly expressed gas vesicles as nanoscale contrast agents for ultrasound and hyperpolarized MRI. *AICHE J.* **64**, 2927–2933 (2018).
23. Farhadi, A., Ho, G. H., Sawyer, D. P., Bourdeau, R. W., & Shapiro, M. G. Ultrasound imaging of gene expression in mammalian cells. *Science* **365**, 1469–1475 (2019).
24. Maresca, D. *et al.* Nonlinear ultrasound imaging of nanoscale acoustic biomolecules. *Appl. Phys. Lett.* **110**, 073704 (2017).
25. Maresca, D. *et al.* Acoustic biomolecules enhance hemodynamic functional ultrasound imaging of neural activity. *NeuroImage* **209**, 116467 (2020).
26. Maresca, D., Sawyer, D. P., Renaud, G., Lee-Gosselin, A., & Shapiro, M. G. Nonlinear X-wave ultrasound imaging of acoustic biomolecules. *Phys. Rev. X* **8**, 041002 (2018).
27. Lakshmanan, A. *et al.* Molecular engineering of acoustic protein nanostructures. *ACS Nano* **10**, 7314–7322 (2016).
28. Santiesteban, D. Y., Hallam, K. A., Yarmoska, S. K., & Emelianov, S. Y. Color-coded perfluorocarbon nanodroplets for multiplexed ultrasound and photoacoustic imaging. *Nano Res.* **12**, 741–747 (2019).
29. Sheeran, P. S. & Dayton, P. A. Phase-change contrast agents for imaging and therapy. *Curr. Pharm. Des.* **18**, 2152–2165 (2012).
30. Ferrara, K., Pollard, R., & Borden, M. Ultrasound microbubble contrast agents: Fundamentals and application to gene and drug delivery. *Annu. Rev. Biomed. Eng.* **9**, 415–447 (2007).
31. Cox, D. J. & Thomas, J. L. Ultrasound-induced dissolution of lipid-coated and uncoated gas bubbles. *Langmuir* **26**, 14774–14781 (2010).
32. Le Floc'h, J. *et al.* In vivo biodistribution of radiolabeled acoustic protein nanostructures. *Mol. Imaging Biol.* **20**, 230–239 (2018).
33. Yan, J., Yin, M., Foster, F. S., & Démoré, C. E. M. Tumor contrast imaging with gas vesicles by circumventing the reticuloendothelial system. *Ultrasound Med. Biol.* **46**, 359–368 (2020).
34. Cheong, H. *et al.* Phagocytic function of Kupffer cells in mouse nonalcoholic fatty liver disease models: Evaluation with superparamagnetic iron oxide. *J. Magn. Reson. Imaging* **41**, 1218–1227 (2014).
35. Smits, L. *et al.* Noninvasive differentiation between hepatic steatosis and steatohepatitis with MR imaging enhanced with USPIOs in patients with nonalcoholic fatty liver disease: A proof-of-concept study. *Radiology* **278**, 782–791 (2016).
36. Miyata, Y., Miyahara, T., & Moriyasu, F. Decreased accumulation of ultrasound contrast in the liver of nonalcoholic steatohepatitis rat model. *World J. Gastroenterol.* **17**, 4191–4198 **(**2011).
37. Macé, E. *et al.* Functional ultrasound imaging of the brain. *Nat. Methods* **8**, 662–664 **(**2011).
38. Oh, Y.-K. & Swanson, J. A., Different fates of phagocytosed particles after delivery into macrophage lysosomes. *J. Cell Biol.* **132**, 585–593 (1996).

39. Davidson, S. J. Proteolytic activity within lysosomes and turnover of pinocytic vesicles. A kinetic analysis. *Biochim. Biophys. Acta, Gen. Subj.* **411**, 282–290 (1975).
40. Harashima, H., Hirai, N., & Kiwada, H. Kinetic modelling of liposome degradation in peritoneal macrophages. *Biopharm. Drug Dispos.* **16**, 113–123 (1995).
41. Berg, S. *et al.* Ilastik: Interactive machine learning for (bio)image analysis. *Nat. Methods* **16**, 1226–1232 (2019).
42. van Rooijen, N. & Hendrikx, E. Liposomes for specific depletion of macrophages from organs and tissues. *Methods Mol. Biol.* **605**, 189–203 (2010).
43. Kinchen, J. M. & Ravichandran, K. S. Phagosome maturation: Going through the acid test. *Nat. Rev. Mol. Cell Biol.* **9**, 781–795 (2008).
44. Yoshimori, T., Yamamoto, A., Moriyama, Y., Futai, M., & Tashiro, Y. Bafilomycin A1, a specific inhibitor of vacuolar-type H^+-ATPase, inhibits acidification and protein degradation in lysosomes of cultured cells. *J. Biol. Chem.* **266**, 17707–17712 (1991).
45. Guo, M. *et al.* High-resolution quantitative proteome analysis reveals substantial differences between phagosomes of RAW264.7 and bone marrow derived macrophages. *Proteomics* **15**, 3169–3174 (2015).
46. Kassel, K. M., Guo, G. L., Tawfik, O., & Luyendyk, J. P. Monocyte chemoattractant protein-1 deficiency does not affect steatosis or inflammation in livers of mice fed a methionine-choline-deficient diet. *Lab. Invest.* **90**, 1794–1804 (2010).
47. Asanuma, T. *et al.* Super paramagnetic iron oxide MRI shows defective Kupffer cell function in non-alcoholic fatty liver disease. *Gut* **59**, 258–266 (2010).
48. Heymann, F. *et al.* Liver inflammation abrogates immunological tolerance induced by Kupffer cells. *Hepatology* **62**, 279–291 (2015).
49. Hebbard, L. & George, J. Animal models of nonalcoholic fatty liver disease. *Nat. Rev. Gastroenterol. Hepatol.* **8**, 35–44 (2011).
50. Itagaki, H., Shimizu, K., Morikawa, S., Ogawa, K., & Ezaki, T. Morphological and functional characterization of non-alcoholic fatty liver disease induced by a methionine-choline-deficient diet in C57BL/6 mice. *Int. J. Clin. Exp. Pathol.* **6**, 2683–2696 (2013).
51. Dill, B. D. *et al.* Quantitative proteome analysis of temporally resolved phagosomes following uptake via key phagocytic receptors. *Mol. Cell. Proteomics* **14**, 1334–1349 (2015).
52. Abu Lila, A. S., Kiwada, H., & Ishida, T. The accelerated blood clearance (ABC) phenomenon: Clinical challenge and approaches to manage. *J. Controlled Release* **172**, 38–47 (2013).
53. Lu, G. J. *et al.* Genetically encodable contrast agents for optical coherence tomography. *ACS Nano* **14**, 7823–7831 (2020).
54. Ai, H.-w., Olenych, S. G., Wong, P., Davidson, M. W., & Campbell, R. E. Hue-shifted monomeric variants of *Clavularia* cyan fluorescent protein: Identification of the molecular determinants of color and applications in fluorescence imaging. *BMC Biol.* **6**, 13 (2008).
55. Piraner, D. I., Wu, Y., & Shapiro, M. G. Modular thermal control of protein dimerization. *ACS Synth. Biol.* **8**, 2256–2262 (2019).

Chapter 4

TRULY TINY ACOUSTIC BIOMOLECULES FOR ULTRASOUND DIAGNOSTICS AND THERAPY

Ling, B., Gungoren, B., Yao, Y., Dutka, P., Lee, J., Lu, G. J., Swift, M. B., Shapiro, M. G. Truly tiny acoustic biomolecules for ultrasound diagnostics and therapy. *In preparation.*

4.1 Abstract

Nanotechnology offers significant advantages for medical imaging and therapy, including enhanced contrast and precision targeting. However, integrating these benefits into ultrasonography has been challenging due to the size and stability constraints of conventional bubble-based agents. Here we describe bicones, truly tiny acoustic reporters based on gas vesicles, a unique class of air-filled protein nanostructures naturally produced in buoyant microbes. We show that these sub-80 nm particles can be effectively detected both *in vitro* and *in vivo*, infiltrate tumors via leaky vasculature, deliver potent mechanical effects through

ultrasound-induced inertial cavitation, and are easily engineered for molecular targeting, prolonged circulation time, and payload conjugation.

4.2 Introduction

Ultrasound is a powerful modality for medical diagnostics and treatment due to its noninvasive nature, real-time imaging capabilities, and widespread accessibility[1]. Incorporation of nanomaterial probes could significantly enhance these benefits, enabling immune evasion, molecular targeting, extravasation, and multifunctional strategies for improved contrast and drug delivery[2,3]. Although such probes have proven successful in modalities such as nuclear and magnetic resonance imaging[4], designing truly nanoscale agents for ultrasound continues to pose a challenge. Conventional agents, formulated as lipid-shelled gas microbubbles, are typically limited by surface tension to sizes larger than 1 μm[5], while proposed submicron agents based on bubbles[6], droplets[7], phase-change[8,9], and gas-trapping particles[10–12] remain relatively large (>200 nm) and can be difficult to prepare.

In this study, we introduce bicones, truly tiny acoustic reporters based on gas vesicles (GVs), a class of air-filled protein nanostructures assembled by certain aquatic microbes for buoyancy regulation[13,14]. GVs comprise a corrugated protein shell of varying thickness (1-3 nm) that excludes liquid water while allowing dynamic gas exchange, creating a stable nanoscale pocket of air[15,16]. Acoustic waves strongly scatter at this air-liquid interface, enabling GVs to serve as contrast agents[14,17–20] and reporter genes[21–24] for ultrasound imaging. They are highly versatile, with physical and acoustic properties that are easily tuned by functionalizing the protein shell or by modifying their constituent genes[17,25]. Additionally,

GVs can serve as therapeutic platforms by stimulating ultrasound mechanotherapy[26] and photodynamic therapy[27].

GV formation begins as a soluble nucleation complex, progresses into a biconical structure, and ultimately elongates into a cylindrical shape[15,16]. We hypothesized that we could produce ultrasmall particles by inhibiting GV growth at the bicone stage. In this study, we test this idea and explore the potential applications of bicones in ultrasound imaging and therapy, evaluating their imaging contrast, tumor-targeting capacity, and interactions with focused ultrasound. Additionally, we devise surface engineering strategies to extend circulation time, target specific cells, and deliver protein cargo. Using these truly tiny acoustic biomolecules, we aim to integrate ultrasonography with nanomedicine.

4.3 Results

4.3.1 Bicones are truly tiny ultrasound contrast agents

We hypothesized that we could disrupt GV elongation by deleting gvpN, a protein essential for this process[28–30]. We modified a previously described bacterial GV cluster containing structural proteins from *Anabaena flos-aquae* and chaperones from *Bacillus megaterium*[22] and expressed this construct in *E. coli* (**Fig. 4-1A**). As hypothesized, transmission electron microscopy (TEM) showed uniformly small, biconical particles (**Fig. 4-1B**). Further deletions of gvpC, gvpR, gvpT, and gvpU did not affect morphology (**Fig. 4-S1**). Cryogenic electron microscopy (cryo-EM) showed that the bicone shell consisted of two low-pitch helices beginning at each tip and converging in the center (**Fig. 4-1C**), consistent with the structure of GVs[16]. Individual particles had an average diameter of 39.7 nm, length of 72.3

nm, and enclosed gas volume of 0.023 aL (76.3% of total volume, assuming a 2-nm thick shell[13]) (**Fig. 4-1D, Table 4-S1**). Bicones were colloidally stable in phosphate-buffered saline (PBS), with a hydrodynamic diameter of 58.4 nm, as measured by dynamic light scattering (DLS) (**Fig. 4-1E**) and zeta potential of −34.9 mV (**Fig. 4-1F**).

Bicones are expected to be highly resistant to external pressure, as shell stability is inversely related to diameter[31]. We tested this using pressurized absorbance spectroscopy, which measures optical density under increasing hydrostatic pressure to identify the threshold when GVs collapse and lose their internal gas content and consequent ability to scatter light[32]. Optical density decreased gradually between 0.9 MPa and 1.3 MPa, with a midpoint at 1.16 MPa (**Fig. 4-1G**). Notably, bicones are the sturdiest GV variant we have developed (**Fig. 4-S2**). To assess collapse under acoustic pressure, we embedded bicones in an agarose phantom and acquired B-mode ultrasound images at a center frequency of 15 MHz with increasing transducer driving voltage. Contrast diminished sharply at 2 MPa and was completely erased at 3 MPa, with a midpoint of approximately 2.4 MPa (**Fig. 4-S3**).

Having confirmed that our transducers could collapse bicones, we visualized them using BURST imaging[21]. This method maximizes sensitivity and specificity for GVs by capturing the transient signals generated during acoustic collapse. BURST signal correlated

linearly with concentration and was reliably detected at 0.5 nM, the lowest concentration tested (**Fig. 4-1H**).

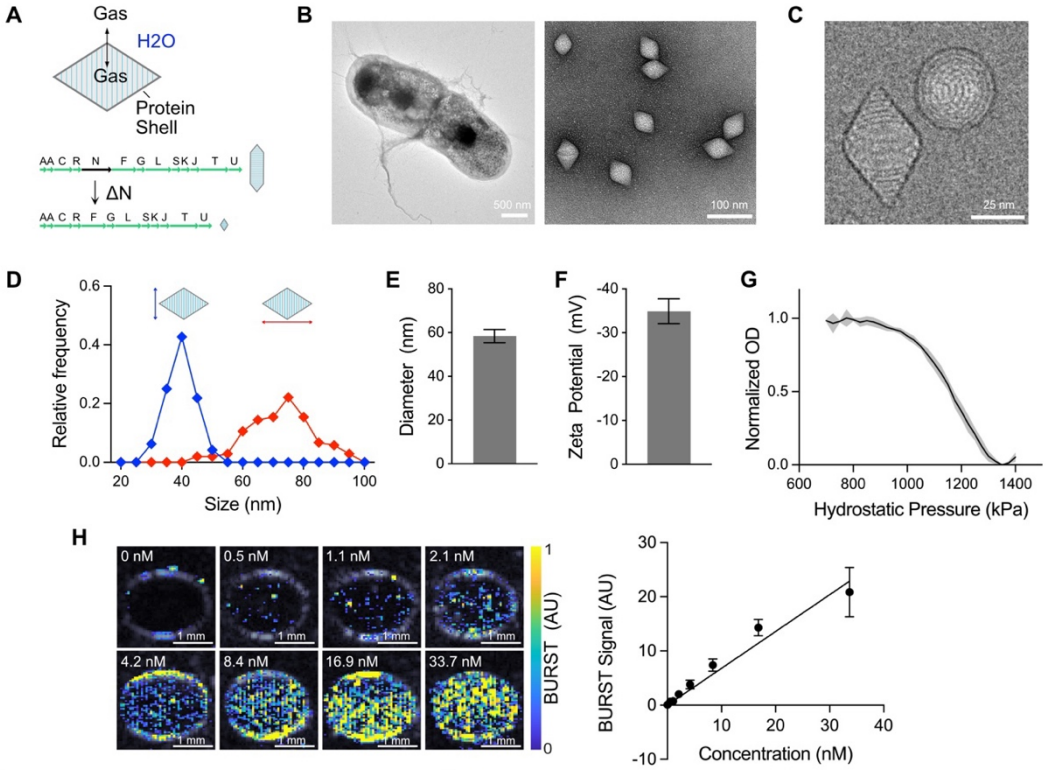

Figure 4-1. Bicones are truly nanoscale ultrasound contrast agents. A) Diagram of bicone structure and gene cluster. Gas can dynamically exchange through the bicone shell, forming a thermodynamically stable pocket of air. Deletion of the gvpN gene prevents GVs from growing beyond the bicone stage. **B)** Representative TEM images of bicones in *E. coli* (left, scale bar, 500 nm) and after purification (right, scale bar, 100 nm). **C)** Representative cryo-EM image of purified bicones showing the helical shell structure. Scale bar, 25 nm. **D)** Distribution of lengths and diameters of individual particles, measured manually from cryo-EM images. N = 100. **E)** DLS measurements of bicones in PBS. N = 35. Error bars, ±SD. **F)** Zeta potential measurements. N = 6. Error bars, ±SD. **G)** Pressurized absorbance spectroscopy measurements of bicones in PBS, normalized to starting OD. N = 6. Thick line, mean; shaded area, ±SEM. **H)** *In vitro* ultrasound imaging of bicones. Left: Representative BURST images of bicones embedded in an agarose phantom at concentrations between 0 nM and 33.6 nM, overlaid on a conventional B-mode image.

Scale bars, 1 mm. Right: Quantification of BURST signal within each well. Data were fit by linear regression, slope = 0.045. N = 12. Error bars, ±SEM.

4.3.2 Bicones enable visualization of tumors

We next investigated the ability of bicones to produce ultrasound contrast *in vivo*. We hypothesized that bicones could be visualized in mouse xenografts, as sub-100 nm nanoparticles are expected to target tumors through leaky vasculature[33–35]. To test this hypothesis, we intravenously (IV) administered 25 pmol bicones into nude mice bearing subcutaneous U-87 MG tumors and performed BURST imaging after 1 h. We chose this dose to maximize delivery by exploiting potential clearance saturation mechanisms[36]. We expected to see contrast only within several millimeters of the transducer focus due to energy attenuation by tissue and the high collapse pressure of bicones. Indeed, BURST signal was detected as a punctate band within the tumor, which was absent during a subsequent acquisition, confirming its specificity to intact particles (**Fig. 4-2A, 4-S4**). We validated tumor accumulation in a separate group of mice by measuring fluorescence of tumors resected 2 h after injection of bicones labeled with a near-infrared dye (**Fig. 4-S5**).

To examine biodistribution, we acquired fluorescence images of mouse organs excised at predetermined intervals following injection of bicones labeled with a far-red fluorescent dye (**Fig. 4-2B**). Fluorescence was highest in the liver, spleen, and kidneys. At 3 h post-injection, mean intensities in these organs were 30.5, 10.7, and 11.0, respectively, decreasing to 9.4, 3.9, and 4.1 at 24 h and 2.6, 1.2, and 1.7 at 48 h. The diminishing fluorescence over time is consistent with active elimination of bicones from the body, with the high kidney signal suggesting renal excretion of lysosomally degraded particles[18,37].

Overall, our data demonstrate that bicones are remarkably small acoustic biomolecules that can be easily produced in bacteria and detected both *in vitro* and *in vivo*.

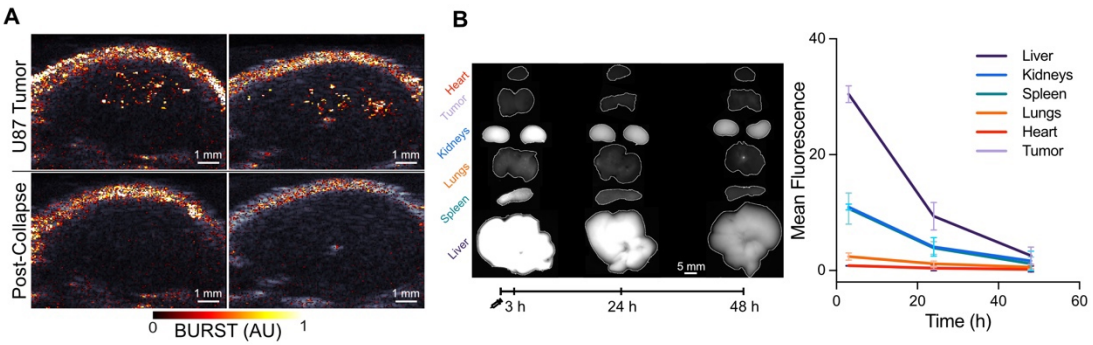

Fig. 4-2. Tumor imaging and biodistribution of bicones. A) *In vivo* ultrasound imaging of bicones. Representative BURST images of subcutaneous U87 MG tumors 1 h after intravenous injection of bicones, overlaid on a B-mode image. Bottom row shows a second acquisition at the same location, confirming signal was specific to intact bicones. Images here are from one of three mice (see **Fig. 4-S4**). Scale bars, 1 mm. **B)** Biodistribution of fluorescently labeled bicones. Left: Representative fluorescence images of mouse organs excised at the specified time after IV injection. Organs are outlined in white. Scale bar, 5 mm. Right: Mean fluorescence intensity within each organ. Data for spleen and tumor are obscured by kidneys and heart, respectively. N = 4 at each time point. Error bars, ±SEM.

4.3.4 Bicones can seed inertial cavitation

Having demonstrated bicone accumulation in tumors, we explored potential therapeutic applications. Specifically, we investigated their capacity to mediate focused ultrasound (FUS) mechanotherapy[26], which can precisely disrupt tissue, promote drug penetration, and eliminate diseased cells by locally inducing inertial cavitation[38]. This phenomenon involves the growth of a bubble—often nucleated by air carried in synthetic agents[11] or released during GV collapse[26]—through mass transfer and coalescence across several acoustic cycles,

culminating in a high-energy implosion (**Fig. 4-3A**). Bubbles undergoing this process generate distinct broadband acoustic emissions[26].

To test the ability of bicones to seed inertial cavitation, we insonated samples with a 330 kHz FUS transducer and recorded acoustic emissions using an orthogonally positioned imaging transducer as a passive cavitation detector (PCD) (**Fig. 4-3B**). We applied FUS to bicone suspensions in acoustically-transparent polymethylpentene (TPX) tubes, chosen to minimize attenuation. At a peak negative pressure (PNP) of 0.3 MPa, intact bicones (5 nM) generated broadband emissions of greater amplitude than both collapsed bicones and PBS (**Fig. 4-3C**). Specifically, PCD signals from intact bicones, collapsed bicones, and PBS were 96.1 dB, 72.6 dB, and 75.4 dB, respectively, rising to 111.0 dB, 104.4 dB, and 104.2 dB at 0.65 MPa PNP (**Fig. 4-3D**). Emissions from intact bicones were comparable to that of *Anabaena* GVs at the same gas fraction (**Fig. 4-S6**). Taken together, our data confirm that the gas content provided by bicones can seed inertial cavitation.

Given the low internal gas volume of bicones, we hypothesized that gas dissolved in the surrounding media is critical for successful cavitation. Indeed, degassing 4.2 nM bicone suspensions in a 20 kPa vacuum chamber reduced PCD signal from 109.4 dB to 95.6 dB when insonated at 0.65 MPa PNP (**Fig. 4-3E-F**). To ensure that this effect was not caused by a reduction in encapsulated air, we diluted samples fivefold to 0.82 nM in ambient conditions, assuming the bicones would retain only 20% of their usual gas content under the reduced pressure. This adjustment did not affect cavitation, thus confirming our hypothesis.

Notably, degassing also reduced PCD signal from collapsed bicones, indicating that the shell plays an important role in nucleating and stabilizing bubbles.

We next examined if bicones remain intact during cavitation. We anticipated that the solvatochromic dye 8-anilinonaphthalene-1-sulfonic acid (ANS) would fluoresce strongly upon binding to the hydrophobic interior of the bicone shell, which is exposed during the collapse process[39,40]. Indeed, bicones collapsed by either bath-sonication or hydrostatic pressure in the presence of 100 μM ANS significantly increased fluorescence (**Fig. 4-3G, 4-S7**). Fluorescence intensity at 480 nm was linearly related to the concentration of collapsed bicones (**Fig. 4-S8**). Using ANS as a convenient optical readout, we quantified collapse in 4.2 nM bicone suspensions after extended FUS insonation with 100 μs pulses at a 500 Hz repetition frequency. We calculated the percentage of collapsed particles based on fluorescence intensity relative to intact and bath-sonicated samples. Less than 5% of bicones collapsed after 3 min at 0.3 MPa PNP or 30 s at 0.65 MPa, while 95% collapsed after 3 min at 0.65 MPa or 30 s at 1.3 MPa (**Fig. 4-3H**). In contrast, 43% of Anabaena GVs collapsed

after just ten pulses at 0.65 MPa (**Fig. 4-S8**). Taken together, our data suggest that bicones can persistently seed cavitation at certain PNPs, provided that dissolved gas is replenished.

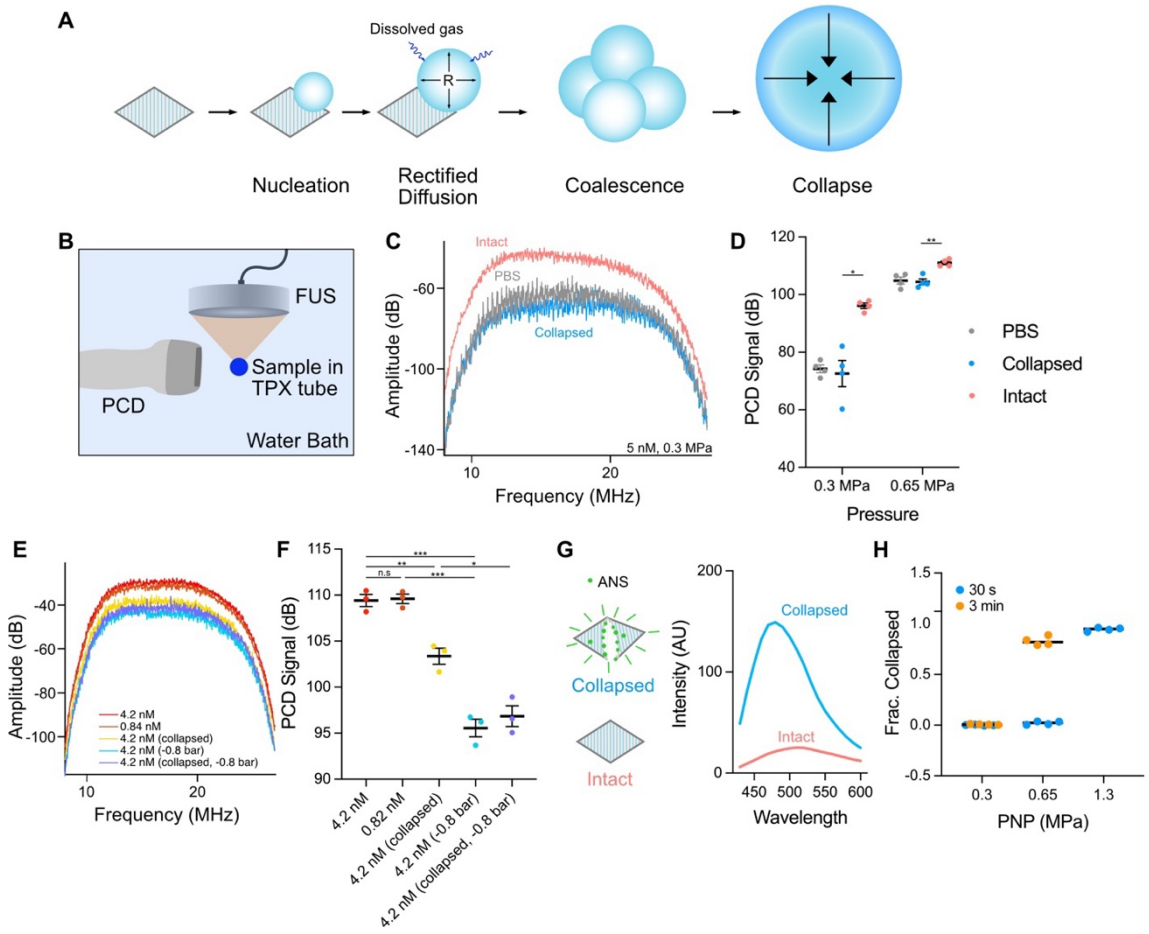

Figure 4-3. Bicones can induce ultrasound mechanotherapy. A) Mechanism of bicone-mediated inertial cavitation. Bubbles are nucleated by the gas content of bicones and grow through mass transfer and coalescence across multiple acoustic cycles, culminating in a high-energy implosion. **B)** Diagram of experimental setup to measure acoustic emissions induced by FUS. Samples contained in acoustically transparent TPX tubes were insonated with a 330-kHz FUS transducer and responses were detected by an orthogonally positioned imaging transducer. **C)** Representative frequency spectra of emissions from intact and pre-collapsed bicones (5 nM) insonated with a single FUS pulse at 0.3 MPa PNP, 30 cycles. **D)** Mean PCD signal from intact and pre-collapsed

bicones (5 nM) insonated with a single FUS pulse at various PNP, calculated by integrating frequency spectra from 8 MHz to 27 MHz. N = 4. Error bars, ±SEM. Welch's t-test (*, $p < 0.05$; **, $p < 0.01$). **E)** Representative frequency spectra from bicones (4.2 nM) at ambient conditions, degassed in a 20 kPa vacuum chamber, or diluted to 0.84 nM. Samples were insonated with a single pulse at 0.65 MPa PNP, 30 cycles. **F)** Mean PCD signal from spectra shown in panel E. N = 3. Error bars, ±SEM. Welch's t-test (*, $p < 0.05$; **, $p < 0.01$; ***, $p < 0.001$; n.s, $p \geq 0.05$). **G)** Left: ANS dye fluoresces upon binding the exposed hydrophobic interior of the bicone shell. Right: Representative emission spectra (ex. 380 nm) of intact and collapsed bicone suspensions containing 100 μM ANS. **H)** Fraction of bicones collapsed after exposure to 30 s or 3 min of FUS pulses at various PNP, calculated based on ANS fluorescence at 480 nm relative to intact and pre-collapsed samples. N = 4. Error bars not shown.

4.3.5 Polymer coated bicones have enhanced circulation

Having identified potential diagnostic and therapeutic applications for bicones, we next developed strategies to optimize their biocompatibility and longevity in the bloodstream. Specifically, we sought to coat bicones with methoxypolyethylene glycol (mPEG), a polymer widely used for immune evasion[41,42]. We focused on azide-alkyne cycloadditions[43–45], as these bio-orthogonal reactions are compatible with GVs[46] and enable convenient access to any azide-functionalized substrate. We attached alkyne groups to lysines on the bicone surface and conjugated 10 kDa azide-mPEG using a copper-catalyzed alkyne-azide cycloaddition (CuAAC) reaction[47] (**Fig. 4-4A**). Consistent with the addition of a PEG layer, hydrodynamic diameter increased from 58 nm to 97 nm (**Fig. 4-4B**) and zeta potential neutralized from −35 mV to −5 mV (**Fig. 4-4C**).

We tested the effectiveness of this modification by measuring apparent circulation time in BALB/c mice. We visualized circulating bicones with ultrafast power Doppler ultrasound imaging, leveraging their ability to enhance blood flow contrast[18,19]. Targeting a single coronal plane in the brain, we acquired images at a center frequency of 15 MHz and

frame rate of 0.25 Hz (**Fig. 4-4D**). After a 5 min baseline, we IV-injected 13 pmol bicones and monitored the ensuing changes in hemodynamic signal (**Fig. 4-4E**). In line with previous studies involving Anabaena GVs, unmodified bicones produced signal enhancement time courses with two distinct peaks, while PEGylated bicones only generated a single peak before returning to baseline monotonically. Fitting to an exponential decay function showed that unmodified bicones circulated with a half-life of 1400 s, while PEGylated bicones circulated with a half-life of 3000 s (**Fig. 4-4F, 4-S10**). Notably, this is an order of magnitude longer than most synthetic agents which typically circulate for only several minutes[1].

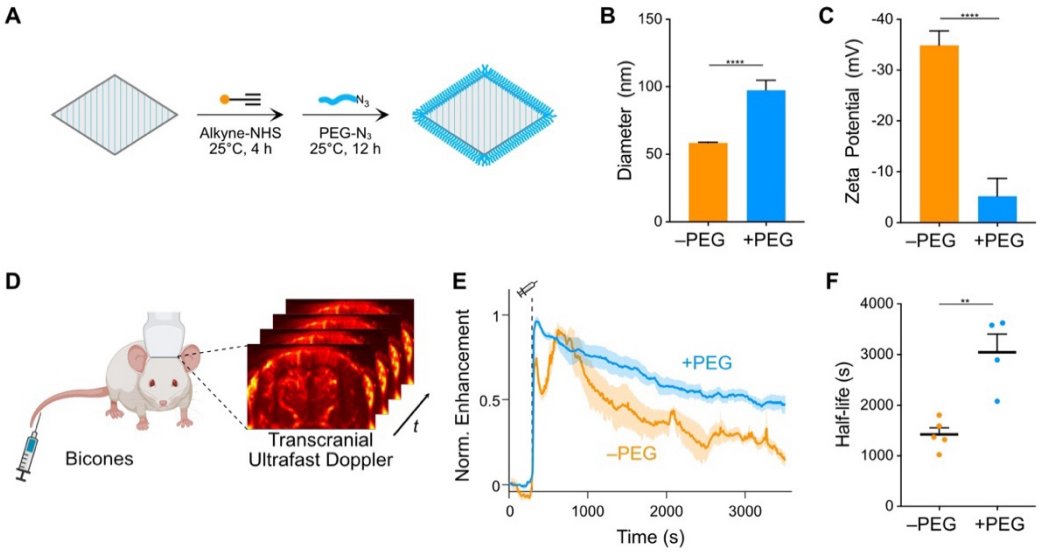

Figure 4-4. Extension of bicone circulation time. A) Diagram of PEGylation protocol. Lysines on the bicone surface were functionalized with alkyne groups and attached to 10 kDa mPEGs through a CuAAC reaction. **B-C)** DLS (**B**) and zeta potential (**C**) measurements of PEG-coated bicones. Data from Fig. 1 shown for comparison (–PEG). N = 5. Error bars, ±SEM. Welch's t-test (****, $p < 0.0001$). **D)** Diagram of experimental setup to determine circulation time. Intravascular bicones were visualized by ultrafast power Doppler ultrasound imaging of the brain. **E)** Normalized

time courses of hemodynamic contrast enhancement following IV injection of bicones. Time of injection (300 s) is indicated by a dashed line. Thick lines, mean; shaded area, ±SEM. N = 4-5. **F)** Circulation half-life calculated by fitting time courses in panel E to an exponential decay function. Error bars, ±SEM. Welch's t-test, (**, $p < 0.01$).

4.3.6 Biochemical functionalization for targeting

In addition to circulation time, retention at the target site is helpful for certain applications. We hypothesized that surface display of cyclic iRGD peptides could enhance cell-specific targeting by binding integrins and triggering internalization[48,49]. To test this hypothesis, we functionalized bicones with dibenzocyclooctyne (DBCO) and a far-red fluorophore, then attached approximately 1000 copies of azide-iRGD to each particle through a strain-promoted alkyne-azide cycloaddition (SPAAC) reaction[42,44] (**Fig. 4-5A**). This estimate assumes 100% conjugation efficiency following reaction with 1000 molar equivalents of DBCO and excess azide-iRGD. We incubated the human cancer cell lines U-87 MG and HT-1080 with these particles for 2 h at 37°C. After rinsing the cells with PBS to remove unbound bicones, we quantified binding by confocal microscopy (**Fig. 4-5B**). Mean fluorescence intensity per field of view increased from 11.4 to 20.9 for U-87 MG cells and from 2.0 to 9.1 for HT-1080 cells when comparing untargeted and targeted bicones (**Fig. 4-5C**). Notably, fluorescence increased with the number of iRGD peptides loaded on each particle (**Fig. 4-S11**). We further validated these results by analyzing the cells via flow cytometry (**Fig. 4-5D, 4-S12**). On average, 34.7% of U-87 MG and 60.3% of HT-1080 cells exposed to iRGD-bicones exhibited significant increases in fluorescence, compared to less than 3% of cells exposed to untargeted bicones (**Fig. 4-5E**). Taken together, our data show that bicone pharmacokinetics can be conveniently modulated by surface engineering, with a

combination of targeting and passivation likely providing the best results for tumor engagement.

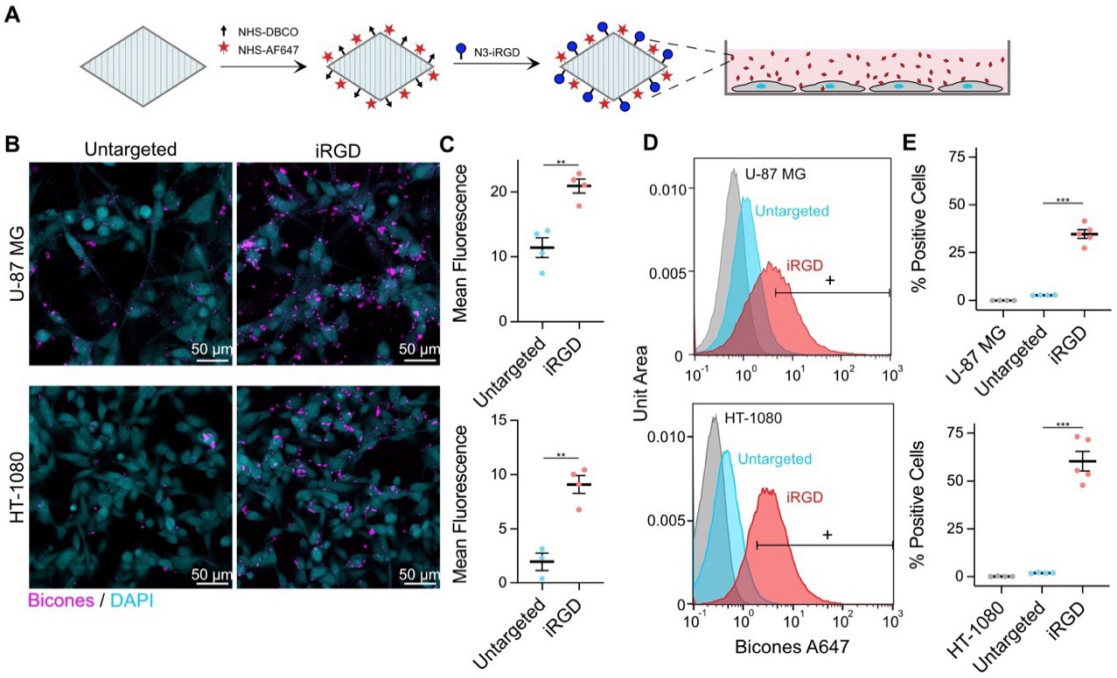

Figure 4-5. Active targeting with bicones. A) Diagram of iRGD conjugation protocol. Bicones were dually-labeled with DBCO and a fluorescent dye, then functionalized with cyclic iRGD peptides by a SPAAC reaction. Purified particles were incubated *in vitro* with human cancer cells. **B)** Representative confocal microscopy images of cells after incubation with bicones. Scale bars, 50 µm. **C)** Mean fluorescence intensity of the bicone channel in images from panel B. Top: U-87 MG; bottom: HT-1080. N = 4. Error bars, ±SEM. Welch's t-test, (**, $p < 0.01$). **D)** Representative flow cytometry histograms of U-87 MG (top) and HT-1080 (bottom) cells incubated with bicones. Bicone-positive cells were gated based on fluorescence in samples incubated with PBS only. **E)** Percentage of bicone-positive cells in histograms from panel D. N = 4-5. Error bars, ±SEM. Welch's t-test, (***, $p < 0.001$).

4.3.7 Genetic functionalization

As genetically encoded agents, bicones can also be functionalized by modification of their constituent proteins, providing a simple and scalable approach that is orthogonal to biochemical systems. Though previously achieved in full GVs via peptide fusion to GvpC[17,25,50], SDS-PAGE analysis showed that bicones lack this protein (**Fig. 4-S13**). To identify alternative options, we appended a FLAG tag[51] to each gene in the GV cluster and tested for association of the fusion protein with purified particles by anti-FLAG dot blot (**Fig. 4-6A**). GvpA and GvpG did not tolerate mutations, while staining from the GvpC and GvpF fusions were weak. However, GvpJ and GvpS produced strong staining. These proteins share homology with the primary structural protein GvpA, suggesting direct incorporation into the GV shell. Indeed, washing the particles with 6 M urea to remove surface-bound proteins[25] did not affect GvpJ or GvpS staining (**Fig. 4-S14**).

Using these new genetic handles, we developed a system to covalently conjugate recombinant proteins to the bicone surface. We fused SpyTag, a 13-residue peptide that spontaneously forms a covalent bond with its partner SpyCatcher domain under physiological conditions[52], to the ends of GvpC, GvpJ, and GvpS. We reacted the purified particles with the model payload SpyCatcher-mNeonGreen[25] (SC-mNG), chosen for easy quantitation of binding through fluorescence (**Fig. 4-6B**). After removing free protein, neither the GvpC mutant nor unmodified bicones exhibited any increase in fluorescence. In contrast, fluorescence from the GvpJ and GvpS fusions increased significantly. When SC-mNG was reacted with similar constructs expressed on GVs with GvpC[22], all three fusion proteins exhibited high fluorescence (**Fig. 4-S15**). Our results indicate that GvpJ and GvpS

are new molecular handles for GV functionalization which can be used in conjunction with the SpyTag-SpyCatcher system to facilitate convenient and modular bioconjugation.

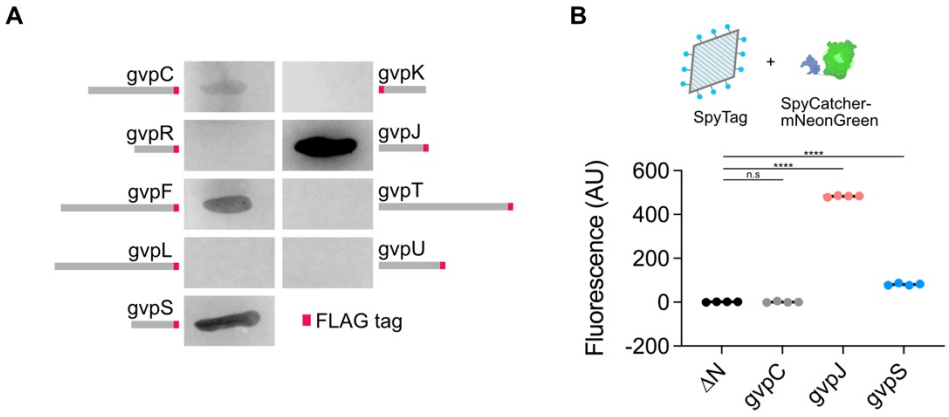

Figure 4-6. Genetic functionalization of bicones. A) Representative images of dot blots. A FLAG tag (shown in red) was appended to the end of each GV gene and the fusion protein was detected using an anti-FLAG antibody. **B)** Top: Bicones with SpyTag appended to gvpC, gvpJ, or gvpS were reacted with the fluorescent protein, SpyCatcher-mNeonGreen. Bottom: Mean fluorescence intensity of purified particles after conjugation. N = 4. Error bars, ±SEM. Welch's t-test, (****, $p<0.0001$; n.s, $p\geq0.05$).

4.4 Discussion

Our results establish bicones as versatile, truly nanoscale agents for ultrasound imaging and therapy. Bicones bridge the gap between ultrasound contrast agents and nanomedicine, unlocking applications beyond the capabilities of large, unstable bubble-based agents. Easily produced in bacteria, their small size allows for passive tumor targeting through leaky vasculature and repeated induction of inertial cavitation without collapsing. Looking beyond cancerous tissue, bicones could potentially enable molecular diagnostics and

mechanotherapy in the mucosal[53], pulmonary[54], and lymphatic systems[55], where larger particles are rapidly sequestered.

The functionality of bicones is further enhanced by the ease with which their surfaces can be modified. This confers additional capabilities, including extended circulation time, molecular targeting, and payload conjugation. Furthermore, their compatibility with CuAAC and SPAAC chemistry provides a convenient pathway for tailoring ligands to individual applications.

Bicones could also help to unravel fundamental aspects of GV formation. As an intermediate stage in GV assembly, proteins from the nucleation complex may be enriched and potentially detectable through mass spectrometry and other proteomic techniques. Cryo-EM analysis of the presumed assembly initiation sites at the tips and GvpA insertion regions at the middle of the shell could yield valuable insights into GV size regulation, informing our ability to modulate GV morphology[15,16].

However, two key improvements are necessary to enhance the utility of bicones. First, non-destructive imaging methods should be developed. While we used BURST imaging for its sensitivity, visualizing bicones without causing collapse would greatly streamline diagnostic applications. This challenge could be addressed by engineering shell proteins to generate nonlinear echoes and by analyzing acoustic responses for unique features that can be captured using specialized pulse sequences[25,56]. Second, a more comprehensive investigation of cavitation processes is required. While our data suggest that bicones can undergo repeated cavitation *in vitro*, *in vivo* demonstrations are yet to be conducted. Achieving this could unlock a multitude of drug delivery and therapeutic applications, with

bicones offering simpler production and functionalization processes compared to existing synthetic agents[11,57].

Over the long term, bicone production and purification processes should be optimized. Lengthy centrifugation steps are impractical at larger scales, and alternatives such as tangential flow filtration or chromatography could be explored. Formal studies of toxicity and biocompatibility should also be conducted in tandem to inform efforts to refine purification processes. While the doses we used did not cause adverse health effects in mice, residual bacterial proteins and antibody development could negatively impact long-term performance.

In conclusion, bicones could allow for techniques previously exclusive to nuclear and magnetic resonance imaging to be translated into the cost-effective and accessible realm of ultrasonography, highlighting the immense potential of these truly tiny particles.

4.5 Methods

Chemicals

All chemicals were purchased from Sigma Aldrich and used without further purification unless otherwise noted.

Bicone preparation

Plasmid construction: The original bicone construct (A2C-ΔN) was prepared by deleting gvpN from the full GV gene cluster (available on Addgene as plasmid #106473) via KLD mutagenesis using enzymes from New England Biolabs and primers from IDT. Briefly, this plasmid contained gvpAAC from *Anabaena flos-aquae* and gvpRFSKJTU from *Bacillus megaterium* downstream of a T7 promoter on a pET28a backbone. Variants were similarly

created. FLAG and SpyTag variants included a short linker (GGSG) before the peptide tag. Primer sequences are included in **Table 4-S2**.

Expression and purification: Plasmids were transformed into *E. coli* strain BL21(DE3) (New England Biolabs) and grown on plates overnight at 37°C (LB agar, 2% glucose, 2x kanamycin). Starter cultures were prepared by inoculating a large number of colonies into 4 mL Miller's LB supplemented with 50 μg/mL kanamycin and 2%w/v glucose and grown at 37°C for 3 h. Large-scale cultures were then prepared by 1:100 dilution of the starter culture in 50 mL LB containing kanamycin and 0.2%w/v glucose. Expression was induced after 2.5 h (OD ~0.6) by addition of 10 μM isopropyl-β-D -1-thiogalactopyranoside (IPTG, Teknova), grown overnight at 37°C, and harvested by centrifugation in 50-mL conical tubes at 450xg (12 h, 4°C). Excess LB was removed by vacuum filtration through binder-free glass microfiber filters (Whatman GF/F grade, Cytiva). Cells were lysed by incubation in 4 mL SoluLyse (Genlantis) supplemented with 100 μg DNaseI (Roche) for 5 h at room temperature. Lysates were then combined and clarified by centrifugation at 600xg for 2 h at 4°C. Bicones were enriched from the supernatant and exchanged into PBS by 5 rounds of overnight centrifugation at 800xg, 4°C followed by replacement of the subnatant with fresh PBS. Concentrations were measured with a Bio-Rad Quick Start Bradford protein assay based on bovine serum albumin standards.

Particle characterization

Dynamic light scattering: A disposable semi-micro polystyrene cuvette (VWR) containing 300 μL of a 2 μg/mL bicone suspension was placed in a Brookhaven Instruments ZetaPALS particle analyzer, and particle size was determined with the ZetaPALS Particle Sizing software using an angle of 90°, thin shell setting, run length of 15 s, and 6 runs per sample. Measurements were recorded as mean intensity-weighted diameter.

Zeta potential: An electrode (SZP, Brookhaven Instruments) was inserted into a mixture of 50 μL of 200 μg/mL bicones in PBS and 1.5 mL Milli-Q water in a disposable plastic cuvette

(SCP, Brookhaven Instruments). Measurements were performed with the ZetaPALS Zeta Potential software using the Smoluchowski model, based on 5 runs of 15 cycles.

Pressurized absorbance spectroscopy: Hydrostatic collapse pressure measurements were performed as previously described[32]. Briefly, 350 µL of a 200 µg/mL bicone suspension in PBS was loaded into a flow-through quartz cuvette (Hellma Analytics). Hydrostatic pressure was applied from a nitrogen gas source through a single valve pressure controller (Alicat Scientific). Pressure was ramped from 700 kPa to 1400 kPa in 25 kPa increments with a 7 s equilibration period prior to measurement of absorbance at 600 nm with a spectrophotometer (OceanOptics STS-VIS). Bicones collapsed at 1.5 Mpa were used as a blank.

TEM: Samples in PBS were diluted 1:10 in water and spotted onto Formvar/carbon 200 mesh copper grids (Ted Pella) that were glow discharge treated (Emitek K100X). The grids were negatively stained with 1% uranyl acetate. Images were acquired with a Thermo Fisher FEI Tecnai 120 keV T12 LaB6 electron microscope equipped with a Gatan Ultrascan 2k x 2k CCD camera and Gatan Digital Micrograph data collection software. Images were processed with Fiji[58].

CryoEM: Images were acquired as previously described[59]. Gold grids (C-Flat 2/2 – 2Au) were glow discharge treated (Pelco EasiGlow). Freshly purified bicone samples (0.5 mg/mL) were spotted onto the grids and flash-frozen using a Mark IV Vitrobot (Thermo Fisher) (4°C, 100% humidity, blot force 3, blot time 6 s). Images were acquired on a 300 kV Titan Krios microscope (Thermo Fisher) equipped with an energy filter (Gatan) and a K3 6k x 3k direct

electron detector (Gatan) using SerialEM software[60]. Images were loaded into Fiji for manual measurement of particle dimensions.

Bicone functionalization

Stoichiometries were calculated assuming 800 gvpA per particle and 1.65e11 particles per μg protein.

PEGylation: Bicones were coated as previously described. Briefly, alkyne-bicones were prepared by mixing purified bicones with propargyl-N-hydroxysuccinimide ester (prepared as a 250 mM stock solution in DMSO) at a 120:1 molar ratio of ester to gvpA and gently rotated at room temperature for 4 h. The particles were then purified by 4 rounds of overnight centrifugation at 800xg/4°C. The CuAAC reaction was prepared by combining 22 mg m-PEG-azide (10 kDa, BroadPharm), 44 μL DMSO, 4.8 μL PBS, 21.5 μL aminoguanidine hydrochloride (prepared as 11.11 mg/mL PBS), and 44 μL of a 1:1 mixture of BTTAA (Click Chemistry Tools, 77.4 mg/mL PBS) and copper sulfate pentahydrate (7.4 mg/mL water). Once the mPEG was fully dissolved, 1.5 mL of a 400 μg/mL alkyne-bicone suspension and 25 μL sodium ascorbate (59.4 mg/mL in PBS, freshly made within 1 h of reaction) were added, and the mixture was rotated slowly overnight at room temperature. PEG-bicones were purified by 4 rounds of centrifugation.

iRGD conjugation: Azide-iRGD peptide was custom synthesized by Thermo Fisher (sequence: azide-PEG4-GGSGGS[C]RGDKGPD[C]). DBCO-bicones were prepared by reacting purified bicones with Alexa Fluor 647-succinimidyl ester (Invitrogen, prepared as 10 mM stock in DMSO) and dibenzocyclooctyne-sulfo-N-hydroxysuccinimide ester (DBCO-Sulfo-NHS ester, Click Chemistry Tools, prepared as 10 mM stock in DMSO) at a 2500:1:10-1000 molar ratio of dye:particle:DBCO. The reaction was allowed to proceed for 4 h at room temperature before purification by 2 rounds of centrifugation. Azide-iRGD peptide (prepared as 1 mg/mL stock in PBS) was added at a 2:1 molar ratio of peptide to

particle, incubated overnight at 4°C with gentle rocking, then purified by 3 rounds of centrifugation.

In vitro ultrasound imaging

Images were acquired using a 128-element linear array probe (L22-14vX, Verasonics) with a center frequency of 18 MHz and elevation focus of 8 mm. The transducer was connected to a programmable ultrasound scanner (Verasonics Vantage 128) operating on Vantage 4.4.0 software.

Phantoms were cast from 1% agarose in PBS using custom printed molds containing pairs of 2-mm diameter cylindrical wells. Samples were gently mixed 1:1 with 2% low-melt agarose in PBS and quickly loaded into the wells. Phantoms were placed on acoustic absorber material and immersed in PBS to couple the sample with the imaging transducer.

Acoustic collapse measurement: Images were acquired using a conventional B-mode sequence operating at 15.625 MHz using a 40-element aperture. The transducer was positioned such that the wells were at a depth of 8 mm, and an automated voltage ramp script was programmed to insonate samples for 10 s at a specified transmit voltage before recording a single frame at 1.6 V. Transmit voltage was ramped from 2 V to 20 V in 0.5 V increments. The fraction of intact GVs at each pressure step was calculated based on mean B-mode intensity within each well, with samples collapsed at 25 V as a blank.

BURST imaging: BURST images were acquired using a previously described imaging sequence[21]. Briefly, a conventional B-mode sequence optimized for frame rate was used to acquire 10 baseline frames at a voltage of 1.6 V and 20 collapse frames at 20 V. BURST signal in each well was calculated by integrating mean signal intensity across all collapse frames using the final frame as a blank. For display, the first two collapse frames were processed with a 1-pixel radius median filter. The second frame was then subtracted from

the first, and voxels with intensities above a threshold were overlaid on a conventional B-mode image.

Focused ultrasound-induced cavitation

Passive cavitation detection: Measurements were performed as previously described[26]. Under B-mode guidance, an L22-14vX imaging transducer was positioned 10 mm from the center of a 3D-printed holder inside of a water tank. A focused ultrasound transducer (Sonic Concepts HT-115) mounted on a computer-controlled 3D-translatable stage (Velmex) was positioned orthogonal to the imaging probe and aligned to the center of the holder based on feedback from a needle hydrophone (HNR-1000, ONDA Corporation). To enable passive cavitation detection, the Verasonics system was programmed with a zero-amplitude transmit and synchronized with the FUS pulse.

Bicone suspensions were dispensed into 1.5 mL polymethylpentene (TPX) tubes (Diagenode) and allowed to equilibrate for several days at ambient conditions. In some cases, dissolved gas was removed by storing overnight in a vacuum chamber held a gauge pressure of -0.8 bar. For PCD measurements, samples were insonated with a 30-cycle burst of 330 kHz sine waves, and emissions were sampled at 62.5 MHz. Frequency spectra were calculated by averaging spectral density across all 128 transducer elements, as computed by Welch's overlapped segment estimation method. PCD signal was calculated by integrating each spectrum from 8 MHz to 27 MHz using trapezoidal sums.

Fluorescence detection of collapse: Suspensions comprising 25 μg/mL bicones and 100 μM ANS were prepared in TPX tubes. Samples were insonated for the specified amount of time with 30-cycle 330 kHz sine wave bursts repeating at 0.5 kHz (2 ms pulse length, ~5% duty cycle). Samples were then distributed into 96-well microplates and analyzed with a Tecan Spark microplate reader using an excitation wavelength of 380 nm and scanning the emission spectrum from 420 nm to 600 nm in increments of 10 nm. Fraction of intact bicones was

calculated based on fluorescence at 480 nm and normalized relative to samples collapsed in an ultrasonic bath (Branson).

Genetic functionalization

Dot blot of shell proteins: FLAG tags[51] (DYKDDDDK) were individually appended to each member of the A2C-ΔN gene cluster and purified as described above. PVDF membranes (Bio-Rad) were wetted in methanol, rinsed in 1x TBS-T (137 mM sodium chloride, 20 mM Tris, 0.1% Tween-20) (diluted from 10x solution from Cell Signaling Technology), and placed on top of a stack of 2 sheets of 3MM Chr chromatography paper (Whatman) soaked in TBS-T and 2 sheets of dry 3MM Chr paper. 5 µg of each bicone sample was quickly spotted onto the membrane and allowed to dry completely. The blot was blocked with 5% blotting-grade blocker (Bio-Rad) in TBS-T for 1 h at room temperature and stained overnight at 4°C with a rabbit anti-FLAG antibody (1:1000 dilution, Millipore F7425). After removing unbound antibodies by three separate 5-minute washes with TBS-T, the blot was stained with Goat anti-Rabbit IgG (H+L) Secondary Antibody, DyLight 650 (Invitrogen, diluted 1:2000 in 5% blocker) for 2 h at room temperature. Blots were washed 4 times with TBS-T and visualized with a Bio-Rad ChemiDoc MP system using automated exposure settings.

SpyCatcher conjugation: Bicones containing SpyTag peptides[52] fused to gvpC, gvpJ, or gvpS were prepared as described above. SpyCatcher-mNeonGreen (SC-mNG) was prepared as previously described[25]. Briefly, SC-mNG was expressed in BL21(DE3), purified by non-denaturing Ni-NTA affinity chromatography (Qiagen), and buffer exchanged into PBS by overnight dialysis through regenerated cellulose tubing (6-8 kDa MWCO, Repligen). To test conjugation, 4 µg of SC-mNG and 40 µg bicones were mixed in a total volume of 150 µL PBS and incubated in the dark for 2 h at room temperature. Samples were purified by 2

rounds of centrifugation prior to measuring fluorescence intensity with a Tecan Spark microplate reader (ex. 485 nm, em. 525 nm).

Cell culture

U-87 MG (HTB-14) and HT-1080 (CCL-121) cells were ordered from the American Type Culture Collection (ATCC) and cultured on tissue culture-treated flasks in Dulbecco's Modified Eagle's Medium (Corning) supplemented with 10% fetal bovine serum (Gibco) and 1% penicillin/streptomycin (Gibco) in a humidified incubator at 37°C and 5% CO_2.

Cell-specific targeting with iRGD

Confocal microscopy: Tissue culture-treated 24-well plates fitted with #1.5H coverslips (ibidi) were seeded with 50,000 U87 or HT1080 cells per well. After 24 h, the media was exchanged with 500 µL Fluorobrite DMEM (Gibco) supplemented with 10 mM HEPES and 10 µg iRGD-bicones. Following a 2 h incubation, the cells were gently washed twice with 500 µL Fluorobrite DMEM, then fixed by sequential incubation in 2% formalin (10% neutral buffered formalin diluted 1:5 in Fluorobrite) for 2 min and undiluted formalin for 20 min. Samples were stained with 300 nM DAPI (Thermo Fisher) for 5 min and stored in Fluorobrite. Imaging was performed with a Zeiss LSM800 confocal laser scanning microscope through the 20x objective using parameters that prioritized signal specificity over speed. Data were loaded into FIJI and summed over each z-stack. Binding was calculated by dividing the total fluorescence in the bicone (Alexa Fluor 647) channel by the number of 'cell' pixels, defined by thresholding autofluorescence in the DAPI channel using Otsu's method.

Flow cytometry: Tissue culture-treated 6-well plates were seeded with 300,000 U87 or HT1080 cells per well. Once the cells reached ~80% confluency, culture media was removed, and the wells were gently washed with 1.5 mL PBS. The cells were then incubated with 25 µg iRGD-bicones in 1 mL Fluorobrite DMEM (Gibco) for 2 h at 37°C. Afterwards, the cells were gently washed twice with 1 mL room temperature PBS, detached with 500 µL 0.25%

trypsin-EDTA (Gibco), and diluted with 500 µL PBS prior to analysis with a Miltenyi MACSQuant Analyzer 10 flow cytometer. Bicone binding was quantified using the R1 channel. Data processing was performed in FlowJo. Gating strategy is shown in **Fig. 4-S12**.

In vivo ultrasound imaging

All in vivo experiments were performed under protocols approved by the Institutional Animal Care and Use Committee at the California Institute of Technology.

Doppler imaging: Female BALB/cJ mice (8-12 wk, Jackson Laboratory) were mounted on a temperature-controlled platform (Stoelting Co., held at 38.5°C) in a stereotaxic instrument (Kopf Instruments) under isoflurane anesthesia (1.5%, 1L/min), depilated over the skull using Nair, and coupled to an L22-14vX transducer with a column of ultrasound gel (Aquasonic). The transducer was positioned to capture an entire coronal section at an arbitrary plane, and a short catheter (30G needle connected to PE10 tubing) was inserted into the lateral tail vein. Ultrafast power Doppler images were acquired at 0.25 Hz for 1 h using a previously described pulse sequence[18]. Five minutes after the start of acquisition, 200 µL bicones (400 µg/mL) were manually injected.

Data were loaded into MATLAB and hemodynamic signal was isolated by singular value decomposition (cutoff of 20). Pixel-wise signal enhancement was calculated as the ratio of intensity at each time point relative to mean intensity over the first 75 frames. Time courses were then extracted by averaging signal enhancement within a manually drawn region of interest encompassing the cortex and smoothed with a 10-unit median filter. To calculate half-life, an exponential decay function was fitted to each time course from its maximum to the end of acquisition.

Tumor accumulation: Subcutaneous flank tumors were implanted in 3-5 week old male Nu/J mice (The Jackson Laboratory) using 3e6 U-87 MG cells suspended in 25% Matrigel matrix

(Corning) diluted with DMEM. Once the tumors were at least 5 mm in diameter, 200 μL of a 0.5 mg/mL bicone suspension was injected through the lateral tail vein. After 1 h, the mice were anesthetized under isoflurane and placed on a temperature-controlled platform. An L22-14vX transducer was coupled to the tumor with a column of ultrasound gel and adjusted such that the center of the tumor was at a depth of 8 mm. BURST images were then acquired as described above.

Biodistribution

Bicones were fluorescently labeled by incubation with 2500x molar equivalents of Alexa Fluor 647 NHS ester (Invitrogen) at room temperature for 4 h and purified by three rounds of centrifugation. Nude mice bearing subcutaneous U-87 MG tumors were IV injected with 200 μL of labeled bicones and transcardially perfused with 50 mL PBS after a predetermined interval. The heart, lungs, kidneys, liver, spleen, and tumor were extracted and imaged with a Bio-Rad ChemiDoc MP using red epi-illumination and a 695/55 nm filter with an exposure time of 0.2 s. Integrated densities were calculated using the built-in "Analyze Particles" function in FIJI. Tumor accumulation was similarly analyzed using the near-infrared dye indocyanine green NHS ester (AdipoGen). Here, only the tumors were resected, and images

were acquired with an IVIS Lumina In Vivo imaging system (PerkinElmer) and analyzed using Living Image software (PerkinElmer).

Statistical analysis

Sample sizes were chosen based on preliminary experiments to yield sufficient power for the proposed comparisons. Statistical methods are described in applicable figure captions.

4.6 Supplementary Information

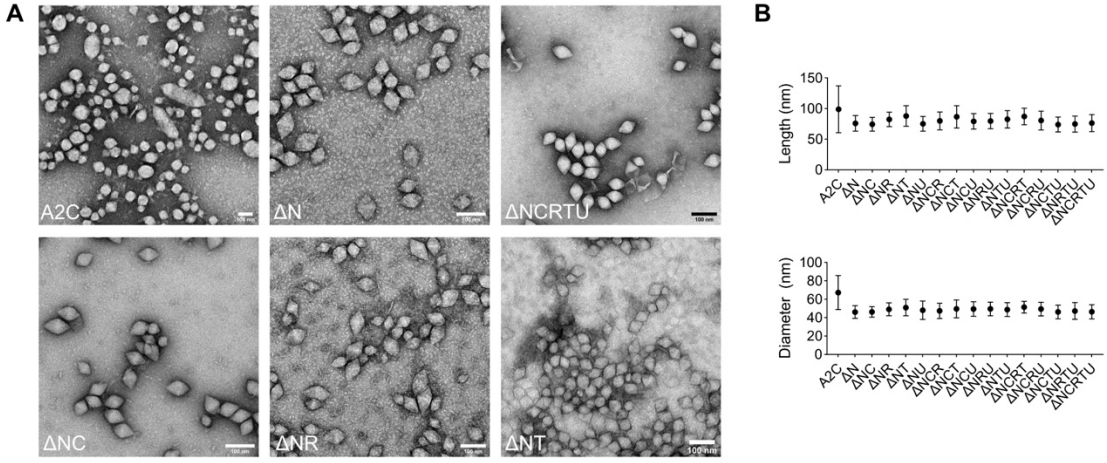

Figure 4-S1. Impact of gene deletions on GV morphology. **A)** Representative TEM images of GVs expressed using the indicated gene cluster. A2C represents the full GV cluster[22]. Deletions are indicated by Δ. Scale bars, 100 nm. **B)** Mean length and diameter of individual particles measured in images from panel A. N = 50-100 particles. Error bars, ±SD.

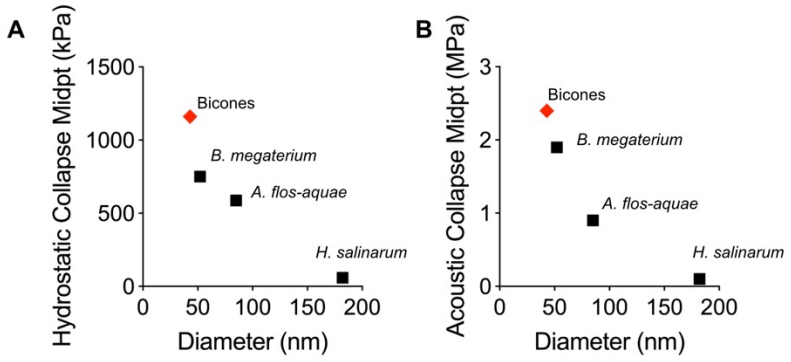

Figure 4-S2. Comparison of hydrostatic (**A**) and acoustic (**B**) collapse midpoints for bicones relative to GVs isolated from *H. salinarum* and *A. flos-aquae*[33], or recombinantly expressed in *E. coli* using a cluster native to *B. megaterium*[20].

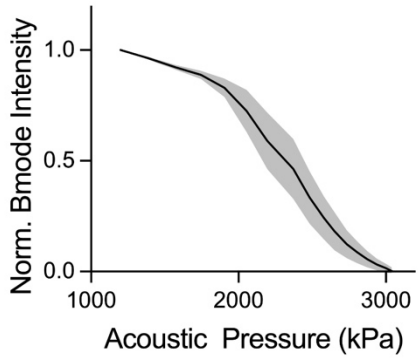

Figure 4-S3. B-mode intensity of bicones embedded in an agarose phantom following exposure to pulses at the indicated acoustic pressure, normalized to the starting value. N = 3. Shaded area, ±SEM.

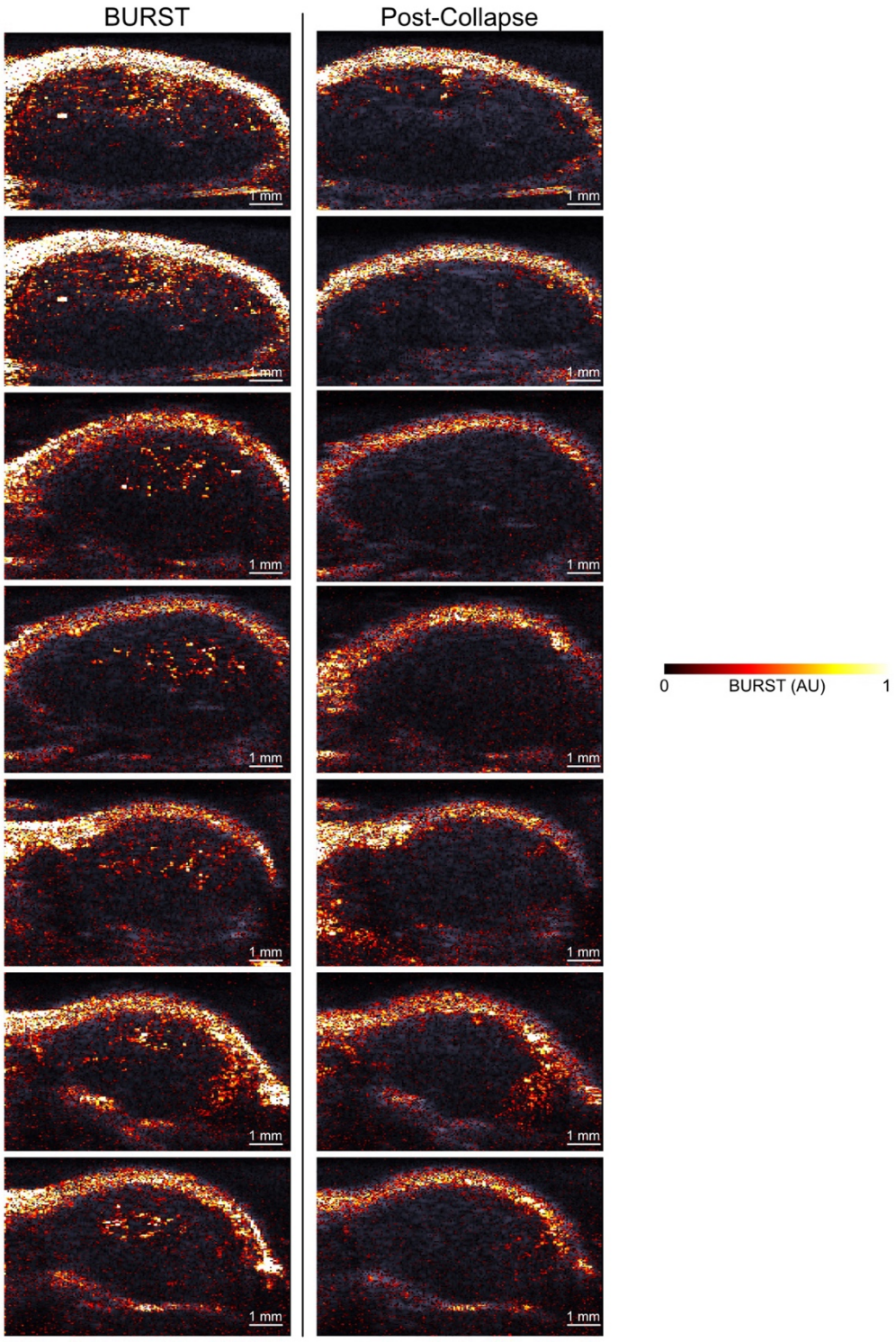
BURST
Post-Collapse
1 mm
0
BURST (AU)
1

Figure 4-S4. BURST images of U-87 MG tumors acquired 1 h after IV injection of bicones, overlaid on a conventional B-mode image. A second acquisition (Post-Collapse) at the same location was used to verify that signal was specific to intact bicones. N = 3. Scale bars, 1 mm.

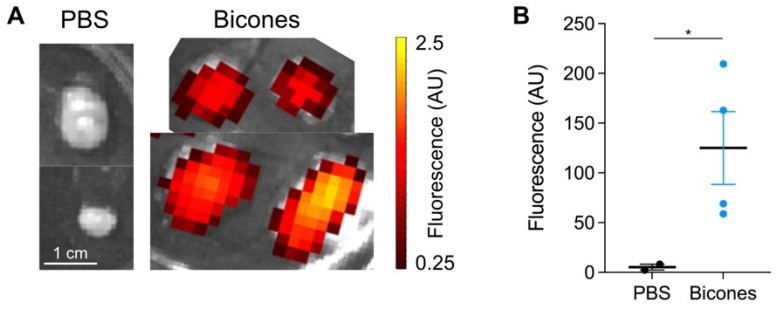

Figure 4-S5. Validation of tumor accumulation. **A)** Fluorescence images of U-87 MG tumors resected 2 h after injection of PBS (N = 2) or bicones labeled with a near-infrared dye (N = 4). A single image was cropped to group replicates together. Scale bar, 1 cm. **B)** Fluorescence intensity of tumors in panel A. Error bars, ±SEM. Welch's t-test, (*, $p<0.05$).

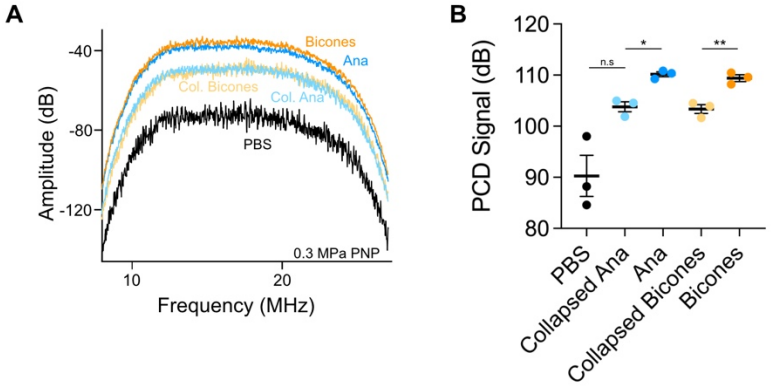

Figure 4-S6. Bicones produce comparable PCD signal to *Anabaena* GVs at the same gas volume. **A)** Representative frequency spectra of acoustic emissions following insonation of bicones (4.2 nM) and *Anabaena* GVs (OD 0.25) with a single pulse at 0.3 Mpa PNP. **B)** Mean PCD signal from spectra in panel A. N = 3. Error bars, ±SEM. Welch's t-test, (*, $p<0.05$; **, $p<0.01$; n.s, $p \geq 0.05$).

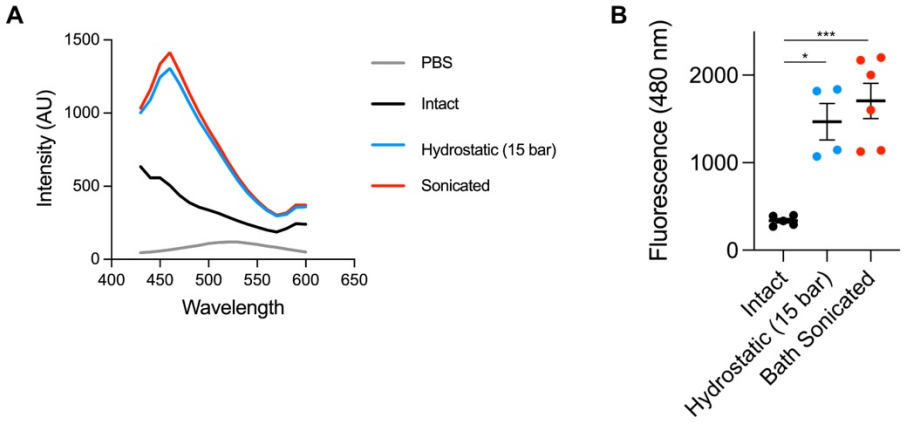

Figure 4-S7. ANS fluoresces in the presence of collapsed bicones. **A)** Representative fluorescence emission spectra (ex. 380 nm) of bicone samples with 100 µM ANS following collapse by bath sonication or hydrostatic pressure. **B)** Fluorescence intensity at 480 nm in spectra from panel A. N = 4–6. Error bars, ±SEM. Welch's t-test (*, $p<0.05$; ***, $p<0.001$).

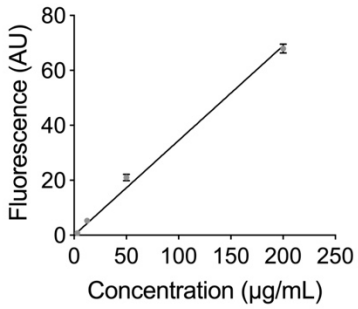

Figure 4-S8. Fluorescence of suspensions containing 100 µM ANS mixed with the indicated concentration of collapsed bicones. Data were fit by linear regression, slope = 0.3447. N = 4. Error bars, ±SEM.

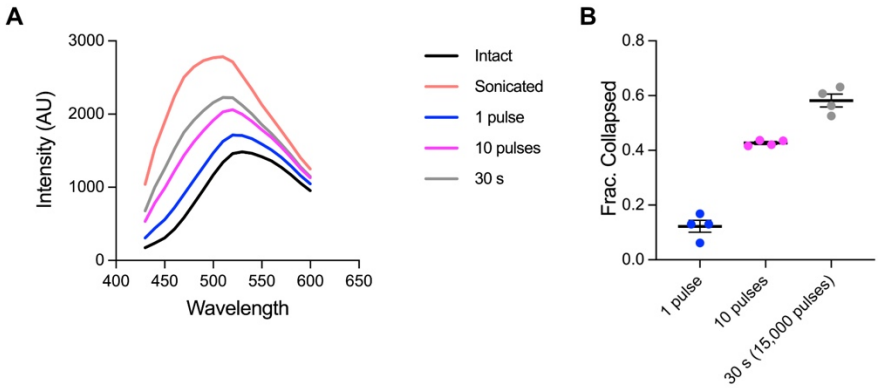

Figure 4-S9. *Anabaena* GVs collapse under FUS insonation. **A)** Representative emission spectra of OD 0.25 *Anabaena* GVs with 100 µM ANS following insonation at 0.65 Mpa PNP, 500 Hz pulse repetition frequency. **B)** Fraction of GVs collapsed, calculated based on ANS fluorescence at 480 nm relative to intact and bath sonicated samples. N = 4. Error bars, ±SEM.

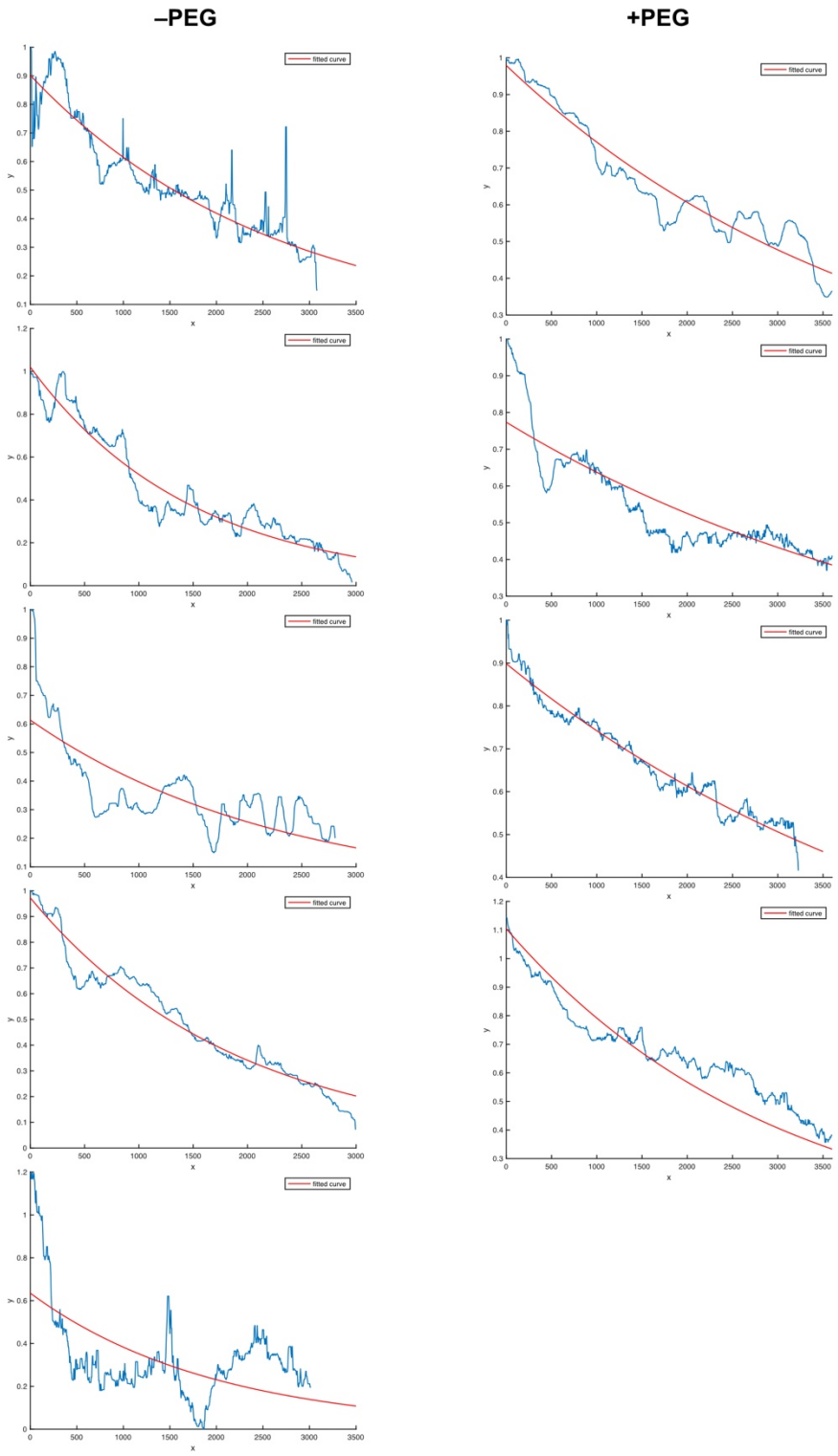
–PEG
+PEG
fitted curve
x
y

Figure 4-S10. Time courses from Fig. 4-3e fitted to an exponential decay function.

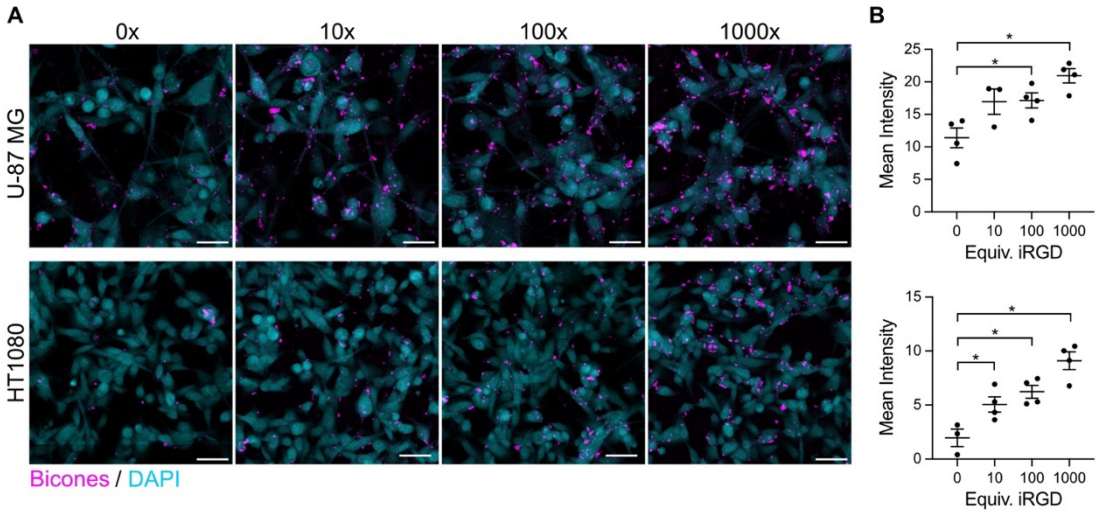

Figure 4-S11. Targeting improves with iRGD loading. **A)** Representative confocal microscopy images of cells after incubation with bicones carrying the indicated number of iRGD peptides. Scale bars, 50 μm. **B)** Mean fluorescence intensity in the bicone channel of cell regions in images from panel A. U-87 MG (top) and HT-1080 (bottom) cells were defined by thresholding on autofluorescence in the DAPI channel. N = 4. Error bars, ±SEM. Welch's t-test, (*, $p < 0.05$).

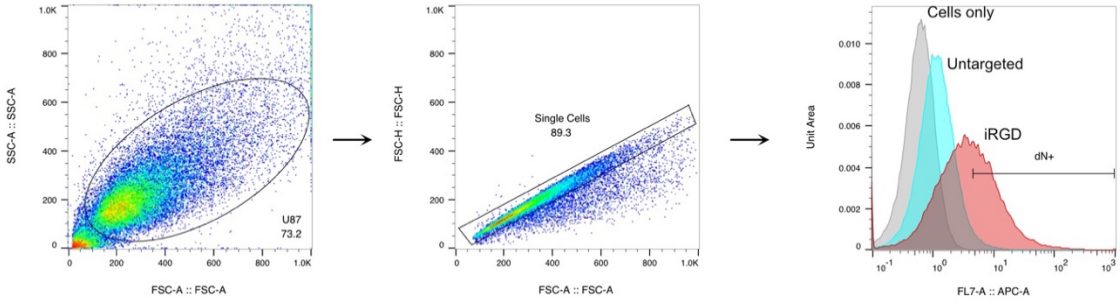

Figure 4-S12. Flow cytometry gating strategy for iRGD targeting experiments. Debris was excluded based on SSC-A vs FSC-A. Single cells were selected from FSC-H vs FSC-A. Bicone positive cells were defined relative to a cell-only control sample.

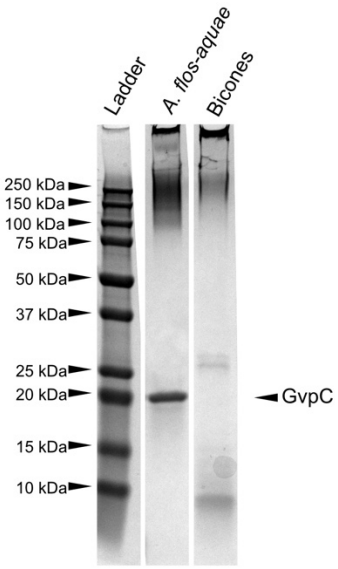

Figure 4-S13. SDS-PAGE of bicones (200 µg/mL) and *Anabaena* GVs (OD 10). GvpC (indicated with an arrow) is not found on bicones.

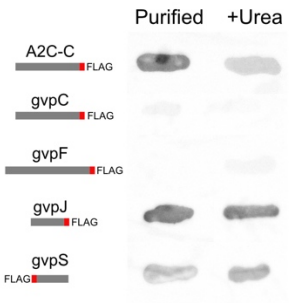

Figure 4-S14. Anti-FLAG dot blot of purified bicones containing the indicated FLAG-fusion protein before and after treatment with 6 M urea to remove surface-bound proteins.

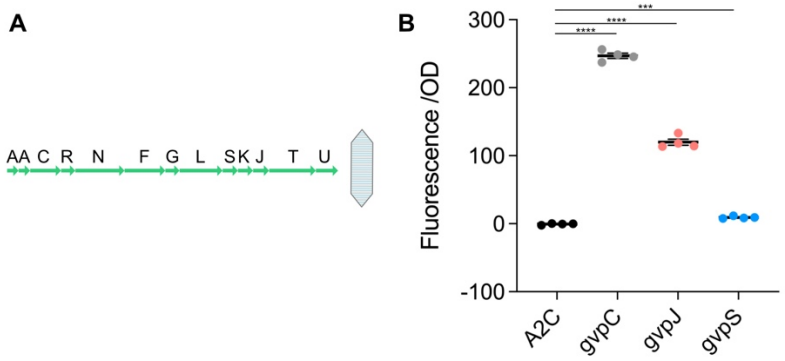

Figure 4-S15. GvpJ and GvpS can also be used to genetically functionalize larger GVs. **A)** A2C gene cluster. The SpyTag peptide was appended to the end of gvpC, gvpJ, or gvpS. Purified particles were then reacted with SC-mNG. **B)** Fluorescence of purified samples after conjugation. N = 4. Error bars, ±SEM. Welch's t-test (***, $p<0.001$; ****, $p<0.0001$).

	Bicones	**Anabaena**
Length (nm)	72	519
Diameter (nm)	40	85
Total volume (aL)	0.03	2.784
Gas vol/total vol	0.764	0.903
Particles/mg protein	1.01e14	2.65e12 (~OD27)
Acoustic Collapse Midpt (MPa)	~2.4	~0.9
Hydrostatic Collapse Midpt (MPa)	~1.2	~0.6

Table 4-S1. Physical properties of bicones compared to *Anabaena* GVs.

		Forward	Reverse
gvpC	SpyTag	TAAGCCGACGAAGGGAGGATCTGGGATTTCTTTAATGGCAAAAATCC	tatgcgtctaccattacaatatgtgcCATGAAGTTCTCCAAAAAATAG
	FLAG	gataaaggggctctgggATTTCTTTAATGGCAAAAATCC	gtcatcatctttataatcCATGAAGTTCTCCAAAAAATAG
	deletion	GAGAACTTCTAAAGATCTAACTATTGGAGGCTACTAAAAATG	CAAAAAATAGTAAATTAGCGCTAGCAAG
gvpR	SpyTag		
	FLAG	gataaaggggctctgggGAAATTAAAAAAATTATGCAAGC	gtcatcatctttataatcCATTTTTAGTAGCCTCCAATAG
	deletion	GCGATAAGATGGCAGGAGCTTG	CTTTAGTAGCCTCCAATAGTTAGATCTTTATTAACC
gvpF	FLAG	gatgatgacaaaTAACGTGCTTCACAAATTAG	gtctttataatccccagagcccccTTTCTCTTCTACTTTTAGGC
	deletion	cgtgcttcacaaattagtaaccgc	GTTTTCAAGCTCCTGCCATCTTATC
gvpG	FLAG	aaagacgatgatgacaaaTAGATGGGAGAATTACTG	ataatccccagagcccccGGATTCCTCATTTCTTTTTTG
	deletion	GAGAAATAAATGGGAGAATTACTGTATTTATACGG	CTCTACTTTTAGGCGAATGTTCAC
gvpL	FLAG	gataaaggggctctgggGGAGAATTACTGTATTTATACG	gtcatcatctttataatcCATCTAGGATTCCTCATTTC
	deletion	CGTGAGGAATTAACATTATGTCTCTTAAAC	CTAGGATTCCTCATTTCTTTTTTGTGTTAGCTCTTC
gvpS	SpyTag	TAAGCCGACGAAGGGAGGATCTGGGTCTCTTAAACAATCCATGG	tatgcgtctaccattacaatatgtgcCATAATGTTAATTCCTCACTTTAC
	FLAG	gataaaggggctctgggTCTCTTAAACAATCCATGG	gtcatcatctttataatcCATAATGTTAATTCCTCACTTTAC
	deletion	gatgcaaccggtcagc	gtgttaattcctcactttacgc
gvpK	FLAG	GATGATGACGATAAATAAGCGGTCAGTAGGAGGAAC	CTTGTAATCCCCAGAGCCCCCAAGCAGGCTGCCTAGCGG
	deletion	cggtcagtaggaggaacag	gtcaggatccaagtggattcg
gvpJ	SpyTag	GTAGACGCATATAAGCCGACGAAGTAAAAACTGTACGCTACTTAAAAAA	CATTACAATATGTGCCCCAGATCCTCCACGTTTCGTTTCTATTTTT
	FLAG	aaagacgatgatgacaaaTAAAAACTGTACGCTACTTAAAAAATG	ataatccccagagcccccACGTTTCGTTTCTATTTTTTC
	deletion	gaactgtacgctacttaaaaaatg	cctgttcctcctactgac
gvpT	FLAG	gataaaggggctctgggGCAACTGAAACAAAATTAGATAAC	gtcatcatctttataatcCATTGTAAATCCCTCCATTTTTTAAG
	deletion	gacgtaaaggaggaaagaaag	ggtaaatccctccatttttttaagtag
gvpU	FLAG	gataaaggggctctgggAGTACAGGCCCTTCTTTTTC	gtcatcatctttataatcCATGTCTTTCTTTCCTCCTTTAC
	deletion	GTCTTTCTTTCCTCCTTTACGTC	CAAACGGCGGGGTGATTGC

Table 4-S2. Primers used for appending SpyTag and FLAG tags, or for gene deletion.

References

1. Ferrara, K., Pollard, R. & Borden, M. Ultrasound microbubble contrast agents: Fundamentals and application to gene and drug delivery. *Annu. Rev. Biomed. Eng.* **9**, 415–447 (2007).
2. Chen, G., Roy, I., Yang, C. & Prasad, P. N. Nanochemistry and nanomedicine for nanoparticle-based diagnostics and therapy. *Chem. Rev.* **116**, 2826–2885 (2016).
3. Pelaz, B. *et al.* Diverse applications of nanomedicine. *ACS Nano* **11**, 2313–2381 (2017).
4. Thakor, A. S. *et al.* Clinically approved nanoparticle imaging agents. *J. Nucl. Med.* **57**, 1833–1837 (2016).
5. Frinking, P., Segers, T., Luan, Y. & Tranquart, F. Three decades of ultrasound contrast agents: A review of the past, present and future improvements. *Ultrasound Med. Biol.* **46**, 892–908 (2020).
6. Leon, A. de *et al.* Contrast enhanced ultrasound imaging by nature-inspired ultrastable echogenic nanobubbles. *Nanoscale* **11**, 15647–15658 (2019).
7. Paproski, R. J. *et al.* Porphyrin nanodroplets: Sub-micrometer ultrasound and photoacoustic contrast imaging agents. *Small* **12**, 371–380 (2016).
8. Sheeran, P. S., Luois, S., Dayton, P. A. & Matsunaga, T. O. Formulation and acoustic studies of a new phase-shift agent for diagnostic and therapeutic ultrasound. *Langmuir* **27**, 10412–10420 (2011).
9. Sheeran, P. S. & Dayton, P. A. Phase-change contrast agents for imaging and therapy. *Curr. Pharm. Des.* **18**, 2152–2165 (2012).
10. Yildirim, A., Chattaraj, R., Blum, N. T., Goldscheitter, G. M. & Goodwin, A. P. Stable encapsulation of air in mesoporous silica nanoparticles: Fluorocarbon-free nanoscale ultrasound contrast agents. *Adv. Healthc. Mater.* **5**, 1290–1298 (2016).
11. Kwan, J. J. *et al.* Ultrasound-propelled nanocups for drug delivery. *Small* **11**, 5305–5314 (2015).
12. Montoya Mira, J. *et al.* Gas-stabilizing sub-100 nm mesoporous silica nanoparticles for ultrasound theranostics. *ACS Omega* **5**, 24762–24772 (2020).
13. Walsby, A. E. Gas vesicles. *Microbiol. Rev.* **58**, 94–144 (1994).
14. Shapiro, M. G. *et al.* Biogenic gas nanostructures as ultrasonic molecular reporters. *Nat. Nanotechnol.* **9**, 311–316 (2014).
15. Huber, S. T., Terwiel, D., Evers, W. H., Maresca, D. & Jakobi, A. J. Cryo-EM structure of gas vesicles for buoyancy-controlled motility. *Cell* **186**, 975-986.e13 (2023).
16. Dutka, P. *et al.* Structure of Anabaena flos-aquae gas vesicles revealed by cryo-ET. *Structure* **31**, 518 (2023).
17. Lakshmanan, A. *et al.* Acoustic biosensors for ultrasound imaging of enzyme activity. *Nat. Chem. Biol.* **16**, 988–996 (2020).
18. Ling, B. *et al.* Biomolecular ultrasound imaging of phagolysosomal function. *ACS Nano* **14**, 12210–12221 (2020).
19. Maresca, D. *et al.* Acoustic biomolecules enhance hemodynamic functional ultrasound imaging of neural activity. *NeuroImage* **209**, 116467 (2020).

20. Farhadi, A. *et al.* Recombinantly expressed gas vesicles as nanoscale contrast agents for ultrasound and hyperpolarized MRI. *AIChE J.* **64**, 2927–2933 (2018).
21. Sawyer, D. P. *et al.* Ultrasensitive ultrasound imaging of gene expression with signal unmixing. *Nat. Methods* **18**, 945–952 (2021).
22. Bourdeau, R. W. *et al.* Acoustic reporter genes for noninvasive imaging of microorganisms in mammalian hosts. *Nature* **553**, 86–90 (2018).
23. Hurt, R. C. *et al.* Genomically mined acoustic reporter genes for real-time in vivo monitoring of tumors and tumor-homing bacteria. *Nat. Biotechnol.* 1–13 (2023).
24. Farhadi, A., Ho, G. H., Sawyer, D. P., Bourdeau, R. W. & Shapiro, M. G. Ultrasound imaging of gene expression in mammalian cells. *Science* **365**, 1469–1475 (2019).
25. Lakshmanan, A. *et al.* Molecular engineering of acoustic protein nanostructures. *ACS Nano* **10**, 7314–7322 (2016).
26. Bar-Zion, A. *et al.* Acoustically triggered mechanotherapy using genetically encoded gas vesicles. *Nat. Nanotechnol.* **16**, 1403–1412 (2021).
27. Song, L. *et al.* Biogenic nanobubbles for effective oxygen delivery and enhanced photodynamic therapy of cancer. *Acta Biomater.* **108**, 313–325 (2020).
28. Tashiro, Y., Monson, R. E., Ramsay, J. P. & Salmond, G. P. C. Molecular genetic and physical analysis of gas vesicles in buoyant enterobacteria. *Environ. Microbiol.* **18**, 1264–1276 (2016).
29. Jost, A. & Pfeifer, F. Interaction of the gas vesicle proteins GvpA, GvpC, GvpN, and GvpO of Halobacterium salinarum. *Front. Microbiol.* **13**, (2022).
30. Pfeifer, F. Recent advances in the study of gas vesicle proteins and application of gas vesicles in biomedical research. *Life* **12**, 1455 (2022).
31. Salahshoor, H. *et al.* Geometric effects in gas vesicle buckling under ultrasound. *Biophys. J.* **121**, 4221 (2022).
32. Lakshmanan, A. *et al.* Preparation of biogenic gas vesicle nanostructures for use as contrast agents for ultrasound and MRI. *Nat. Protoc.* **12**, 2050–2080 (2017).
33. Perry, J. L. *et al.* Mediating passive tumor accumulation through particle size, tumor type, and location. *Nano Lett.* **17**, 2879–2886 (2017).
34. Sykes, E. A., Chen, J., Zheng, G. & Chan, W. C. W. Investigating the impact of nanoparticle size on active and passive tumor targeting efficiency. *ACS Nano* **8**, 5696–5706 (2014).
35. Tang, L. *et al.* Investigating the optimal size of anticancer nanomedicine. *Proc. Natl. Acad. Sci. U. S. A.* **111**, 15344–15349 (2014).
36. Ouyang, B. *et al.* The dose threshold for nanoparticle tumour delivery. *Nat. Mater.* **19**, 1362–1371 (2020).
37. Poon, W. *et al.* Elimination pathways of nanoparticles. *ACS Nano* **13**, 5785–5798 (2019).
38. Kooiman, K. *et al.* Ultrasound-responsive cavitation nuclei for therapy and drug delivery. *Ultrasound Med. Biol.* **46**, 1296–1325 (2020).
39. Cardamone, M. & Puri, N. K. Spectrofluorimetric assessment of the surface hydrophobicity of proteins. *Biochem. J.* **282**, 589–593 (1992).
40. Hawe, A., Sutter, M. & Jiskoot, W. Extrinsic fluorescent dyes as tools for protein characterization. *Pharm. Res.* **25**, 1487–1499 (2008).

41. Jokerst, J. V., Lobovkina, T., Zare, R. N. & Gambhir, S. S. Nanoparticle PEGylation for imaging and therapy. *Nanomed.* **6**, 715–728 (2011).
42. Yan, J., Yin, M., Foster, F. S. & Démoré, C. E. M. Tumor contrast imaging with gas vesicles by circumventing the reticuloendothelial system. *Ultrasound Med. Biol.* **46**, 359–368 (2020).
43. Taiariol, L., Chaix, C., Farre, C. & Moreau, E. Click and bioorthogonal chemistry: The future of active targeting of nanoparticles for nanomedicines? *Chem. Rev.* **122**, 340–384 (2022).
44. Agard, N. J., Prescher, J. A. & Bertozzi, C. R. A strain-promoted [3 + 2] azide−alkyne cycloaddition for covalent modification of biomolecules in living systems. *J. Am. Chem. Soc.* **126**, 15046–15047 (2004).
45. Meldal, M. & Tornøe, C. W. Cu-catalyzed azide−alkyne cycloaddition. *Chem. Rev.* **108**, 2952–3015 (2008).
46. Kim, W.-S. *et al.* Magneto-acoustic protein nanostructures for non-invasive imaging of tissue mechanics in vivo. *bioRxiv* doi: 10.1101/2022.05.26.493158 (2022).
47. Besanceney-Webler, C. *et al.* Increasing the efficacy of bioorthogonal click reactions for bioconjugation: A comparative study. *Angew. Chem. Int. Ed.* **50**, 8051–8056 (2011).
48. Sugahara, K. N. *et al.* Tissue-penetrating delivery of compounds and nanoparticles into tumors. *Cancer Cell* **16**, 510–520 (2009).
49. Lo, J. H. *et al.* iRGD-guided tumor-penetrating nanocomplexes for therapeutic siRNA delivery to pancreatic cancer. *Mol. Cancer Ther.* **17**, 2377–2388 (2018).
50. Kim, J.-M. *et al.* Bioengineering of Halobacterium sp. NRC-1 gas vesicle nanoparticles with GvpC fusion protein produced in E. coli. *Appl. Microbiol. Biotechnol.* **106**, 2043–2052 (2022).
51. Hopp, T. P. *et al.* A short polypeptide marker sequence useful for recombinant protein identification and purification. *Bio/Technology* **6**, 1204–1210 (1988).
52. Zakeri, B. *et al.* Peptide tag forming a rapid covalent bond to a protein, through engineering a bacterial adhesin. *Proc. Natl. Acad. Sci. U. S. A.* **109**, E690–E697 (2012).
53. Xu, Q. *et al.* Impact of surface polyethylene glycol (PEG) density on biodegradable nanoparticle transport in mucus ex divo and distribution in vivo. *ACS Nano* **9**, 9217–9227 (2015).
54. Yang, L. *et al.* Multimodal precision imaging of pulmonary nanoparticle delivery in mice: Dynamics of application, spatial distribution, and dosimetry. *Small* **15**, 1904112 (2019).
55. Cai, S., Yang, Q., Bagby, T. R. & Forrest, M. L. Lymphatic drug delivery using engineered liposomes and solid lipid nanoparticles. *Adv. Drug Deliv. Rev.* **63**, 901–908 (2011).
56. Maresca, D. *et al.* Nonlinear ultrasound imaging of nanoscale acoustic biomolecules. *Appl. Phys. Lett.* **110**, 073704 (2017).
57. Paris, J. L., Cabañas, M. V., Manzano, M. & Vallet-Regí, M. Polymer-grafted mesoporous silica nanoparticles as ultrasound-responsive drug carriers. *ACS Nano* **9**, 11023–11033 (2015).

58. Schindelin, J. *et al.* Fiji: an open-source platform for biological-image analysis. *Nat. Methods* **9**, 676–682 (2012).
59. Dutka, P. *et al.* Measuring gas vesicle dimensions by electron microscopy. *Protein Sci.* **30**, 1081–1086 (2021).
60. Mastronarde, D. N. Automated electron microscope tomography using robust prediction of specimen movements. *J. Struct. Biol.* **152**, 36–51 (2005).

Chapter 5

CONCLUSIONS AND FUTURE DIRECTIONS

This thesis describes early efforts to adapt GVs for nanodiagnostic applications, serving as a foundation for future studies to further refine the design and application of these agents. Chapter 2 detailed the blood interactions of GVs, examining how adsorption onto RBCs and the formation of a protein corona influenced acoustic response, circulation time, and immunogenicity. In Chapter 3, the focus shifted to the liver's role in processing GVs, showing their phagocytosis and lysosomal degradation within macrophages, and demonstrating how these processes could be measured to monitor liver disease. Chapter 4 introduced bicones, currently the smallest known ultrasound contrast agent, and explored their use in various applications including tumor targeting, ultrasound mechanotherapy, and blood flow imaging. This work underscores the tremendous potential of GVs as injectable nanomaterials and the considerations that must be factored into their design.

Nevertheless, the successful integration of GVs into clinical practice requires overcoming numerous challenges, encompassing both general concerns related to GV

production and application-specific obstacles, such as optimizing delivery efficiency. Below, we discuss some of these challenges, as well as unique opportunities for GVs.

5.1 Considerations for GV production

Efficient and scalable production of GVs is required for their transition from the laboratory to the clinic. Each stage of the production process, from microbial growth to purification, has unique opportunities for improvement.

Currently, our laboratory cultivates *A. flos aquae* in individual flasks, allowing for the harvesting and processing of several liters of culture each week[1]. While this approach is adequate for small-scale use, it will require significant scaling up to produce the quantities needed for clinical use. One potential solution involves the use of bioreactors to enhance culture volumes. These systems also offer the advantage of precise control over growth conditions, allowing for careful optimization of GV yield. Additionally, they could enable continuous efflux, maintaining the cells in exponential growth and bypassing the slow lag phase typically experienced when initiating cultures.

Following cell harvesting, the GVs are released via hypertonic lysis and purified through a series of centrifugation steps. A more streamlined approach could be the use of diafiltration, which could combine the steps of cell concentration, hypertonic lysis, GV washing, and buffer exchange into a single, automatable process. Furthermore, diafiltration could facilitate the removal of residual proteins on the GV surface, which as discussed in Chapter 2, may contribute to unwanted immune reactions. However, this process must be

carefully managed to avoid high pressures that could lead to GV collapse. An alternative strategy could involve the incorporation of a chromatography step for greater selectivity.

In addition to production considerations, regulatory requirements cannot be overlooked. The approval process for new diagnostic or therapeutic agents demands rigorous demonstrations of safety, efficacy, and consistency. Given that GVs are produced in microbes, strategies must be developed to ensure consistency in morphology, purity, and other properties. Furthermore, while our data suggest that GVs are degraded and renally excreted, this must be thoroughly confirmed.

5.2 GV surface engineering

The promise of GVs as nanodiagnostic agents is directly linked to their ability to target specific tissues effectively. This ability is contingent upon the successful optimization of affinity ligands tailored to each application. Our results demonstrate that GVs are compatible with various bioconjugation methods, such as EDC/NHS and alkyne-azide click chemistry, providing a flexible platform for the attachment of a range of molecules, including polymers, peptides, antibodies, lipids, aptamers, and even other particles for multimodal imaging applications.

However, the presence of a protein corona and adsorption of GVs onto RBCs can significantly influence targeting capabilities. Our initial attempts to reduce these interactions with PEG led to an unintended consequence—the production of anti-PEG antibodies, provoking anaphylactic reactions upon repeated administration within a specific timeframe.

Given these results, a key area for future research is to survey alternative coatings. Potential candidates, such as RBC membrane cloaking[2], lipid coating, and pre-formed protein coronas[3,4] have demonstrated efficacy in other contexts and warrant further investigation with GVs.

The introduction of foreign agents into the body invariably results in the production of antibodies. A potentially transformative, yet ambitious, strategy to mitigate this response involves the genetic modification of antigenic epitopes on GVs. This could be achieved by analyzing the peptides displayed on antigen-presenting cells following lysosomal degradation of GVs to identify problematic sequences. These epitopes can then be eliminated by application of CRISPR and other genome engineering technologies[5], delivered to *Anabaena* cells using vehicles capable of penetrating cell walls, such as carbon nanotubes[6]. This approach has the additional benefit of retaining the original organismal chassis, thereby maintaining high GV yields. However, this strategy may not be universally applicable due to the extensive variability in binding capacities of different alleles in the human leukocyte antigen complex.

The interaction of GVs with RBCs presents intriguing possibilities. Beyond the benefits outlined in Chapter 2, such as immune tolerance and enhanced circulation half-life, this interaction could enable innovative drug delivery methods. For example, molecules loaded into RBCs via hypotonic swelling[7] could be released via GV-induced inertial cavitation. This mechanism may prove to be more effective than previous attempts using temperature-sensitive liposomes, as cavitation provides an immediate, convective release

mechanism. This approach could potentially be better executed with bicones, given their ability to cavitate repeatedly.

5.3 Emerging sensing methods

Chapter 3 highlighted the unique capacity of GVs to probe cellular degradation processes. Many existing nanoparticles degrade over timescales that are too long for practical monitoring, while existing optical sensors are difficult to use with larger organisms due to limited light penetration in tissue. However, GVs overcome these limitations, providing insight into intracellular processes deep within live tissue.

Inflammation has been implicated in the progression of many diseases and is intrinsically linked to lysosomal function[8]. For example, inflammatory signaling prompts the accumulation of immune cells and lipids on arterial walls in atherosclerosis and is thought to contribute to the progression of neurodegenerative diseases such as Alzheimer's and Parkinson's. Targeted delivery of GVs to these tissues could offer a means to monitor disease progression and assess treatment efficacy.

The reporter gene functionality of GVs could also be leveraged to monitor autophagy, a fundamental cellular process responsible for degrading and recycling internal components. Dysregulation of this process has been linked with a variety of conditions, including aging, neurodegeneration, and cancer[9,10]. Furthermore, we could potentially track sub-cellular processes such as mitophagy by appending an organelle affinity ligand to the GVs.

Noninvasive visualization of autophagy would enhance our understanding of its role in disease and how it is affected by organismal health.

5.4 Future directions for bicones

Our results have highlighted the potential of bicones as a platform for ultrasound diagnostics and therapy. However, to fully utilize these acoustic nanomaterials, several areas require further optimization and exploration.

One such area is the production protocol of bicones. Currently, yields from *E. coli* tend to be modest, and the purification process involves many time-consuming centrifugation steps. A potential solution is to produce bicones in *Anabaena*. As the native hosts of GVs, these organisms likely possess sophisticated control over the stoichiometry and other factors involved in GV assembly, which could improve bicone yield. Additionally, substituting centrifugation with tangential flow filtration could significantly expedite the purification process.

Enhancing the ultrasound contrast generated by bicones is another area for improvement. Although their small dimensions inherently limit scattering, increasing contrast could substantially broaden their diagnostic utility. This could potentially be achieved by mutagenesis of shell proteins to enable buckling and generation of nonlinear contrast, though it is important to note that gvpA has limited tolerance for mutations. Alternatively, bicones could be used in conjunction with techniques such as cryoEM, cell-free translation, and mass spectrometry to inform our understanding of GV assembly, the

mechanisms underlying nucleation and elongation, and factors that regulate GV size. This knowledge could then be implemented to precisely control GV morphology.

As one of the few truly nanoscale, sub-100 nm agents for ultrasound, bicones present a unique opportunity to translate a range of existing nanomedicine applications to ultrasonography. These include traversal of mucosa, navigation through lymph networks, and targeting to the brain. For example, the dissemination of many cancer cells occurs via the lymphatic system[11]. Bicones could potentially be used to identify and detect particular molecules within lymph nodes, assisting with cancer staging and guiding surgical intervention. However, as with any nanomaterial, a comprehensive understanding of potential immune responses and biocompatibility is required.

The transformative potential of GVs arises from the convergence of their unique material properties and ultrasound's wide accessibility. The work presented here is just the beginning of an exciting journey towards implementing these agents into routine clinical practice. Persistently challenging the limits of possibility, GVs will undoubtedly buoy ultrasound technology to new heights.

References

1. Lakshmanan, A. *et al.* Preparation of biogenic gas vesicle nanostructures for use as contrast agents for ultrasound and MRI. *Nat. Protoc.* **12**, 2050–2080 (2017).
2. Hu, C.-M. J. *et al.* Erythrocyte membrane-camouflaged polymeric nanoparticles as a biomimetic delivery platform. *Proc. Natl. Acad. Sci.* **108**, 10980–10985 (2011).
3. Rampado, R., Crotti, S., Caliceti, P., Pucciarelli, S. & Agostini, M. Recent advances in understanding the protein corona of nanoparticles and in the formulation of "stealthy" nanomaterials. *Front. Bioeng. Biotechnol.* **8**, (2020).
4. Oh, J. Y. *et al.* Cloaking nanoparticles with protein corona shield for targeted drug delivery. *Nat. Commun.* **9**, 4548 (2018).
5. Barrangou, R. & Doudna, J. A. Applications of CRISPR technologies in research and beyond. *Nat. Biotechnol.* **34**, 933–941 (2016).
6. Demirer, G. S., Zhang, H., Goh, N. S., González-Grandío, E. & Landry, M. P. Carbon nanotube–mediated DNA delivery without transgene integration in intact plants. *Nat. Protoc.* **14**, 2954–2971 (2019).
7. Muzykantov, V. R. Drug delivery by red blood cells: Vascular carriers designed by mother nature. *Expert Opin. Drug Deliv.* **7**, 403–427 (2010).
8. Aderem, A. Phagocytosis and the inflammatory response. *J. Infect. Dis.* **187**, S340-5 (2003).
9. Aman, Y. *et al.* Autophagy in healthy aging and disease. *Nat. Aging* **1**, 634–650 (2021).
10. Levine, B., Mizushima, N. & Virgin, H. W. Autophagy in immunity and inflammation. *Nature* **469**, 323–335 (2011).
11. Jain, R., Dandekar, P. & Patravale, V. Diagnostic nanocarriers for sentinel lymph node imaging. *J. Controlled Release* **138**, 90–102 (2009).